MULTI-FRAGMENTATION AND DISAPPEARANCE OF FLOW IN INTERMEDIATE ENERGY HEAVY-ION COLLISIONS

By

TONG QING LI

A DISSERTATION

Submitted to
Michigan State University
in partial fulfillment of the requirements
for the Degree of

DOCTOR OF PHILOSOPHY

Department of Physics and Astronomy

1993

ABSTRACT

MULTI-FRAGMENTATION AND DISAPPEARANCE OF FLOW IN INTERMEDIATE ENERGY HEAVY-ION

By

Tong Qing Li

The equation of state (EOS) of nuclear matter can be probed through heavy ion reactions if finite size effects are taken into account. A first-order liquid-gas phase transition and the critical point, if measured, can provide a calibration point for EOS.

The critical behavior of nuclear fragmentation is characterized by a power law cluster mass distribution. The measured Z-distributions of fragments emitted from central collisions of ^{40}Ar + ^{45}Sc at beam energies from 15 to 115 MeV/nucleon have been fitted to power laws $\sigma(Z) \propto Z^{-\lambda}$. The apparent exponent, λ, reaches a minimum at a beam energy of 23.9 ± 0.7 MeV/nucleon. A percolation model calculation reproduces the observed Z-distributions for all beam energies, using the mean excitation energy as extracted from proton kinetic energy spectra. We extract the critical value of the deposited excitation energy for our system and make predictions for the dependence of this quantity on the size of the fragmenting system. The asymptotic limit of the critical temperature for a binding energy of 8 MeV/nucleon is found to be 13.1 ± 0.6 MeV using percolation calculations. The asymptotic critical point can be used as a constraint for the EOS of nuclear matter.

Dynamically the EOS can be probed by collective motion. At low beam energies ($\sim$ 10MeV/nucleon), the dominant interaction in the reaction zone is the attractive

MULTI-FRAGMENTATION AND DISAPPEARANCE OF FLOW IN INTERMEDIATE ENERGY HEAVY-ION COLLISIONS

By

TONG QING LI

A DISSERTATION

Submitted to
Michigan State University
in partial fulfillment of the requirements
for the Degree of

DOCTOR OF PHILOSOPHY

Department of Physics and Astronomy

1993

ABSTRACT

MULTI-FRAGMENTATION AND DISAPPEARANCE OF FLOW IN INTERMEDIATE ENERGY HEAVY-ION

By

Tong Qing Li

The equation of state (EOS) of nuclear matter can be probed through heavy ion reactions if finite size effects are taken into account. A first-order liquid-gas phase transition and the critical point, if measured, can provide a calibration point for EOS.

The critical behavior of nuclear fragmentation is characterized by a power law cluster mass distribution. The measured Z-distributions of fragments emitted from central collisions of $^{40}Ar + ^{45}Sc$ at beam energies from 15 to 115 MeV/nucleon have been fitted to power laws $\sigma(Z) \propto Z^{-\lambda}$. The apparent exponent, λ, reaches a minimum at a beam energy of 23.9 ± 0.7 MeV/nucleon. A percolation model calculation reproduces the observed Z-distributions for all beam energies, using the mean excitation energy as extracted from proton kinetic energy spectra. We extract the critical value of the deposited excitation energy for our system and make predictions for the dependence of this quantity on the size of the fragmenting system. The asymptotic limit of the critical temperature for a binding energy of 8 MeV/nucleon is found to be 13.1 ± 0.6 MeV using percolation calculations. The asymptotic critical point can be used as a constraint for the EOS of nuclear matter.

Dynamically the EOS can be probed by collective motion. At low beam energies ($\sim$ 10MeV/nucleon), the dominant interaction in the reaction zone is the attractive

mean field, which leads to a negative dynamical deflection (flow) of the final particles. At high beam energies ($\sim$ 400MeV/nucleon), the dominant interaction is the nucleon-nucleon (n-n) repulsive interaction, which leads to a positive deflection (flow) of the final products. The balance energy is the beam energy at which the mean field attraction is balanced by the n-n repulsion. This balance energy compared with dynamical calculation such as the Boltzmann-Uehling-Uhlenbeck (BUU) model can provide constraints on the EOS.

We observed the balance energy of Ar + Sc to be 87 ± 12 MeV/nucleon. A single observation of central collisions of one system apparently cannot give strong constraints on EOS.

Dedicated with love to Michelle and Dillon.

ACKNOWLEDGEMENTS

I wish to thank my thesis advisor, Gary Westfall, for his encouragement and patience during all the ups and downs over the years. It is his advise, guidance and teaching that made the four years of research challenging and full of fun; and it is his sense of humor that made the work fabulously enjoyable (not all the time of course) and rewarding.

A special thanks to Wolfgang Bauer for his support of my change from doing theory to doing experiments and for his constant support and advice in the theoretical aspects of the research.

I also owe a deep debt to all of my 4π colleagues: Roy Lacey's "plans" and discussions, our hot debate and our downstairs rush for scheduled runs, leaves an unerasable memory; Skip Vander Molen, his "call me now" spirit on running experiment; Ken Wilson's enthusiastic and patient discussions, his leading role on research made my first year a lot easier and fun; Sherry Yennello, her advise over all aspects of my graduate student "life" (if we have any), from physics to every day problems, are invaluable; Jaeyong Yee, for his silent support and over night hard work; Gene Gualtieri, for his jokes and his patience of listening to all of my problems; Darren Craig, for his working on everything for four dollars an hour spirit and his contribution to all aspects of this thesis work are highly acknowledged;

Special thanks to all the lab directors, Sam Austin, Konrad Gelbke and Walt Benenson, for their financial support on the research, travel to conferences and summer schools, and for their excellent management, which makes the lab a most productive one.

I also wish to express my appreciation to all of my colleagues at the NSCL: John Yurkon and Dennis Swan, on their supervision in making detectors; most of all, their

friendly help made the working downstairs a lot of fun. Len Morris and Steve Bricker, for their support on mechanical work of the detectors and their cooperative spirit; Jim Vincent, our electronic life saver; Cyclotron operating staff for their patience to hear "where is the beam" millions of times; all the secretaries and staff, they make the NSCL an easy, comfortable and fun place to work.

Most of all, I owe great debt to my parents. It is their encouragement, their endless support and their love that made me who I am and made my pursuit in physics possible; to my wife, whose love, patience and understanding made the final finishing of my thesis a lot of easier; and my son, Dillon, whose midnight crying made this thesis a little late but a much more colorful part of my life.

Contents

List of Tables

List of Figures

Chapter 1

Introduction

The first heavy ion accelerator that made heavy ion reaction studies possible at beam energy of 1 GeV per nucleon was the Princeton-Penn Accelerator in 1972 [Gupt93]. When the Bevatron, a weak focusing synchrotron which could produce 6.2 GeV protons, was coupled with the SuperHILAC, a linear accelerator which could accelerate heavy ions to 8 MeV/nucleon, the Bevalac at Berkeley went into operation. Heavy ions could be accelerated at the Bevalac up to 2.1 GeV/nucleon [Gupt93, Gutb89a]. The high energy nucleus bombarding the target nucleus can create high excitation and high pressure. Nuclear matter with densities as high as 2 to 4 times the nuclear saturation density can be studied in a controlled laboratory environment. These studies may provide reliable information towards the bulk properties of nuclear matter at high density as studied by astronomical observations in neutron stars and supernovas. Heavy ion reactions turned the attention of nuclear physicists from the structure of nuclei to the bulk properties of nuclear matter. The first goal is simple and clear – the determination of the equation of state (EOS) of nuclear matter.

The difficulties of measuring the EOS of nuclear matter are due to the fast time scale and small space scale, which make direct time-dependent measurements impossible. Only final products are measured with a given detector acceptance. The microscopic process of heavy ion reactions can not be observed directly. Thus, the

picture of the time evolution of a reaction system largely relies on theories. Heavy ion reactions increase the number of participating particles to the order of 10^2 comparing with proton-proton collision, but the particle number scale is far from the macroscopic situation of 10^{23} particles. The macroscopic observables such as temperature, pressure, entropy, etc. either have large fluctuation in the finite size system or have different physical meanings. The finite size, which cause large fluctuations in all the statistical quantities, makes the study of the EOS difficult.

1.1 Nuclear Matter Compressibility

Due to the high energy and short time scale, it is difficult to measure directly macroscopic quantities such as volume, and pressure. Therefore, it is impossible to directly measure the thermodynamic properties of nuclear matter as we could in the classical case. Astronomical observations indicate that such highly compressed, highly excited systems do exist in supernova and neutron stars.

The properties of the nuclear EOS are discussed in terms of nuclear compressibility, which represents the hardness of nuclear matter against compression. Hence, the nuclear compressibility is measured, or estimated, from secondary observables compared with theoretical models. Putting all possible constraint on the nuclear compressibility is essential to both nuclear physics and astrophysics. The Landau theory of Fermi liquids gives a K from 74 to 371 MeV [Brow85]. The study of giant monopole resonance, which corresponding a compressional mode of the nucleus, showed that $K \sim 210 \pm 30$ MeV [Blai80]. The droplet model of nuclear masses suggests K from 210 to 410 MeV. The dynamic study of Bevalac energy collective flow showed a compressibility of 380 MeV [Krus85] using BUU model which incorperates nucleon-nucleon collisions and a mean field with no momentum dependent

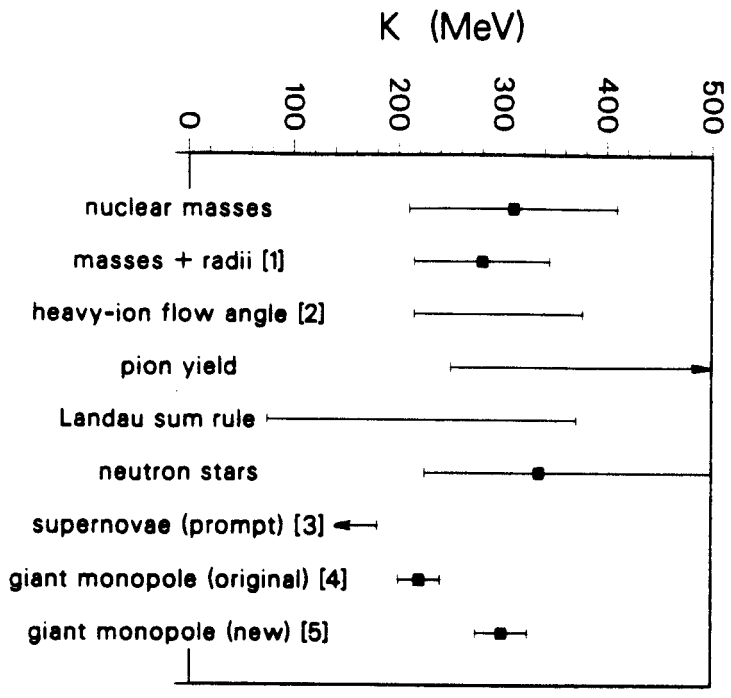

Figure 1.1: Nuclear compressibility obtained from different studies. (from reference [Glen88]). Reference [1] to [5] are listed in [Glen88].

terms. Later study using BUU calculation with momentum dependent mean field indicated a compressibility of 215 MeV [Gale90]. Glendenning summarized all the different studies of the nuclear compressibility and plotted the result shown in Figure 1.1 [Glen86].

Intermediate energy heavy ion physics exhibits many transitional phenomena which may provide more information concerning nuclear compressibility. At this energy, the excitation is high enough to break apart the nucleus but is not high enough to totally disintegrate it into its component nucleons. A transition from sequential decay where the hot nuclear system decays through a binary decay chain to multifragmentation where the system breaks up in a fast time scale may occur. Or a transition from fission-evaporation process, which indicates a liquid-gas coexistence,

to a critical point at which the system evaporates totally with no heavy residue may be possible. A first order liquid-gas phase transition terminates at a critical point.

Different from statistical systems, there is also a strong dynamical process involved in heavy ion reactions. The entrance projectile incedent on the target nucleus with a certain impact parameter and velocity is a unique initial condition which leads the evolution of the reaction system both statistically and dynamically. Some strong collective motion such as transverse flow, azimuthal distributions and rotation have been observed [Gutb89a, Gutb89b, Wils91, Lace93]. The dynamic collective flow changes direction in this energy region, which indicate a competition between nucleon-nucleon repulsive and meanfield attractive interactions. The dynamical observations provide information on the interactions between particles in the reaction zone. Therefore, the search for the EOS of nuclear matter is in two inseparable directions: statistical studies and dynamical studies.

1.2 Statistical Behavior of Heavy Ion Reaction

High energy heavy ion reactions are successfully described by the statistical fireball model which assumes the projectile nucleus interacting with the target creates a fireball and target and projectile spectators. [West76, Goss77, West82, Jaca87] (see Figure 4.5). Due to the high excitation energy, the reaction system can be disintegrated into light particles. At low beam energies (below 8 MeV/nucleon), the reaction process is dominated by fusion-fission and light particle evaporation. It is in the intermediate energy region, the beam energy from 10 to several hundred MeV per nucleon, that there is a transition from binary fission-evaporation and sequential decay processes to multi-fragmentation processes. Multi-fragmentation is defined as the simultaneous emission of heavy particles ($Z \geq 3$). Theoretical studies based on statistical de-

scriptions indicate that in the intermediate energy region the heated and compressed reaction system goes through the mechanical instability region during the expansion where the system disintegrates simultaneously [Good84, Boal86]. On the pressure vs. density plot, during the expansion, the system goes through the liquid-gas co-existence region (see Figure 4.2) since the nuclear equation of state resembles the properties of classical Van der Waals gas. There is a second order phase transition characterized by a critical point. Below the critical point, the liquid-like compound system may evaporate light particles or fission while above the critical point, the system may totally break up into light particles [Good84, Jaqa84, Boal86, Pana84, Kapu84, Bond85].

There are two extreme approaches in statistical theories, the sequential decay approach and the simultaneous breakup approach [Frie89, Lópe89, Cebr90a] in describing the heavy ion reactions. In the sequential statistical theory, one assumes that the compound system de-excites through a sequence of binary breakups. The final fragments are the sum of the chain binary decay. The decay rates are assumed to be given by detailed balance [Frie89]. While simultaneous emission assumes a statistical ensemble (canonical or micro canonical), the fragments are in equilibrium with each other as the system expands. The two approaches are illustrated by Figure 1.2.

It is observed that at low beam energies (below 10 MeV/nucleon), the particle emission is dominated by binary sequential decay, while at high energies, the multifragmentation takes place [Cebr90a, Cebr90b, Biza93] Determination of onset of multifragmentation has been a major research effort in the last five years [Boug88, Yenn90, Bowm91, Blum91, Yenn91, Ogil91, Hube91, Bowm92, Kim92, Sang92, Hage92, Grab92, Ogil93, Peas92]. To discriminate the two different statistical processes, observables which are sensitive to the evolution of the system are necessary. The study of the phase space event shape of the emission particles, parameterized by sphericity and coplanarity [Cebr90a], can distinguish the transition from sequential decay to si-

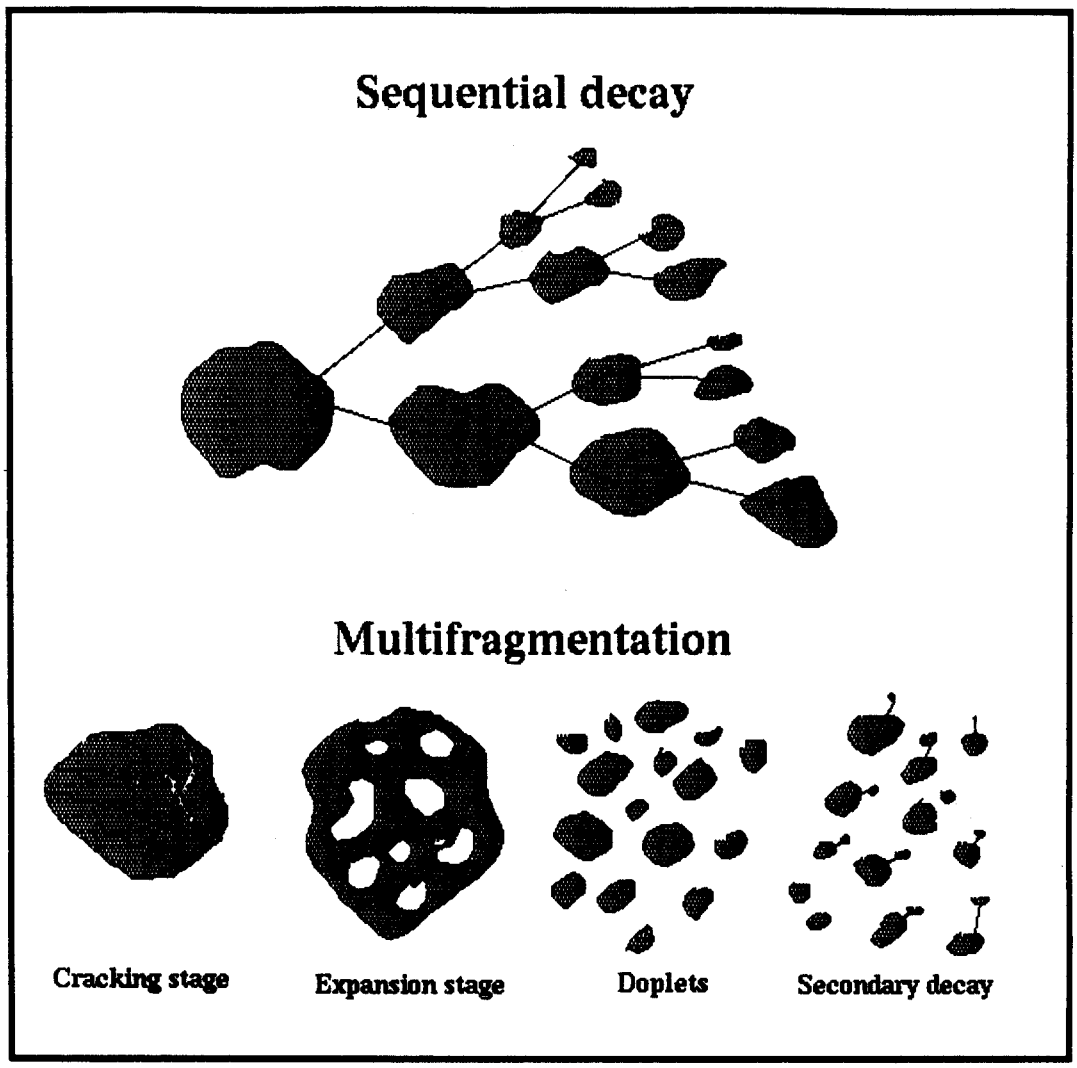

Figure 1.2: Two statistical approaches for nuclear fragmentation

multaneous emission. Because binary sequential decay has an elongated pattern in momentum space, while simultaneous emission is more isotropic [Cebr90a], the onset of multifragmentation can be observed by studying the event shapes for a variety of beam energies [Cebr90a].

Also associated with the statistical properties of heavy ion reaction is the liquid-gas phase transition of nuclear matter, which has been predicted in the intermediate energy region for decades [Küpp74, Saue76, Lamb78, Jaqa84, Good84, Pana84, Kapu84, Bond85, Boal86]. The similarity of nucleon-nucleon interaction with the interaction of Van der Waals gas suggests a critical behavior of bulk nuclear matter may exist [Abra79]. The nuclear EOS derived from two body interactions using a variety of methods all show the first order liquid-gas phase transition terminating at a critical point. Recently, the results of inclusive fragment production of high energy proton induced reactions stimulated wide spread interests [Finn82, Mini82, Hirs84, Hüfn85].

The observable for studying the liquid-gas phase transition is the mass distribution of the final reaction products. Both Fisher's droplet model [Fish67, Pana84, Pori89] and percolation theory [Stau79, Baue85, Baue88] predict that the cluster distribution has a power law form in the vicinity of the critical point. At the critical point, the exponent of the power law goes to a minimum. The measured critical point can be used to constrain the EOS if finite size effects are considered.

From the EOS of nuclear matter, the critical point can be obtained by setting the first and second derivative of pressure to nucleon density equal to zero (see section 4.1.1). Therefore, determination of the critical point using the cluster distributions can provide information about the EOS of nuclear matter. Both inclusive measurements of proton and light ion induced reactions showed the power law behavior and the proton induced reaction showed a minimum of the power law exponent [Pori89, Hirs84, Finn82, Chit83, Yenn90].

However, the inclusive measurements are integrated over impact parameters leading to different types reactions with different excitation energies. To obtain unambiguous evidence of such critical phenomena for a finite system, more exclusive measurements must be done and, most importantly, the finite size effects have to be treated [Jaqa84].

To obtain unambiguous measurements of the statistical properties, especially the transitional properties such as sequential decay to multifragmentation, or the liquid-gas phase transition, better exclusive measurements are necessary. Because the initial conditions such as impact parameter and reaction plane, and excitation energy can be estimated using exclusive measurements, the study of central collisions will provide unambiguous statistical information.

1.3 Dynamical Behavior

Dynamical collective motion has been observed in heavy ion reactions [Gutb89b]. The averaged phase space distributions show some non isotropic properties, such as transverse momentum flow, squeeze out and rotation [Gutb89a, Krof89, Krof91, Wils90, Wils91, Krof92]. Dynamical collective motion may provide information concerning the interactions inside the reaction zone. Dynamical model calculations show the gross features of the collective motion of heavy ion reactions. The most successful dynamical model, the Boltzmann-Uehling-Uhlenbeck (BUU) transport equation calculation [Bert88, Gale90, Pan93], which incorporates the mean field of nuclear matter and nucleon-nucleon collisions, reproducs the observed transverse momentum flow [Ogil90, Gale90, Krof92, Pan93].

At intermediate energies, the nucleon-nucleon hard core repulsion competes with the mean field attraction. At low beam energy, the mean field attraction is stronger

than nucleon-nucleon repulsion and a negative deflection of the final reaction products will occur. At high beam energy, the nucleon-nucleon repulsive collision dominates the reaction, and a positive deflection of the final reaction products will be observed. At a certain beam energy (depending on the mass of the reaction system), if the mean field attraction is balanced by nucleon-nucleon repulsion, the flow will disappear. The energy at which the transverse flow disappears is called the balance energy, which can be used to determine the mean field parameters. In BUU, the EOS is linked with the mean field [Bert88]. Comparing the experimentally measured balance energy with the theoretical calculation, we can gain information about the mean field and therefore the EOS.

The balance energy calculated by BUU is strongly sensitive to the medium nucleon-nucleon cross sections which is a parameter of the nucleon-nucleon collisions of the BUU calculation, but it is weakly sensitive to the nuclear compressibility. The single measurement of balance energy does not provide a complete constraint on the input used by BUU. In order to obtain complete constraint on the input parameters of BUU, we must do measurements of the balance energy for different reaction systems and measurements of the impact parameter dependence of the balance energy [West93, Sull90].

1.4 Organization of the Thesis

The main objective of this thesis is to probe the nuclear EOS by studying the properties of the statistical breakup of the reaction system and dynamical collective motion.

The thesis concentrates on the experiment of ^{40}Ar + ^{45}Sc at 15, 25, 35, 45, 65, 75, 85, 95, 105 and 115 MeV/nucleon. The main goal of the experiment is to study the onset of multifragmentation and the liquid-gas phase transition [West88]. The

MSU 4π Array can exclusively characterize the collisions. Only central collisions are studied in this thesis. In chapter 2, the experimental set-up, particle identification and data reduction are discussed in detail.

Before the statistical and dynamical results can be addressed, the initial condition of the reaction, i.e. impact parameter and reaction plane, must be determined. In chapter 3, the event characterization is discussed. The impact parameter is determined by an analytical formula which links the impact parameter to global observables using the probability density distribution of the global observable. To obtain a common centrality cut for all studies with minimum bias, a combined global observable is proposed. Then the method of reaction plane determination, the azimuthal correlation method, is introduced. A comparison with the previously used transverse momentum method shows that a better measurement of reaction plane is given by the azimuthal correlation method.

Multifragmentation is discussed in chapter 4. Observed Z-distributions are corrected for the detector acceptance. These distributions are related to critical behavior. Then a percolation calculation, linking the bond breaking probability to the proton kinetic energy slope parameter is presented. Comparing with the GSI experiment of Au + C, Al, Cu at 600 MeV per nucleon [Ogil91], the percolation calculation shows the mass dependence of critical behavior. To estimate the finite size effects, we run the percolation calculation increasing the size of the initial system. The asymptotic limit of the critical point that has been obtained for a binding energy of 8 MeV per nucleon is $T_c = 13.1 \pm 0.6$ MeV.

In chapter 5, we discuss the dynamics of the nearly symmetric system in terms of transverse flow and the disappearance of the flow. Comparing with the BUU calculation, the nuclear compressibility be discussed.

Chapter 6 will summarize the results.

Chapter 2

Experiment

2.1 Introduction

The experiment was done at the National Superconducting Cyclotron Laboratory (NSCL) of Michigan State University (MSU) with MSU 4π Array. The newly finished Bragg Curve Counters (BCC) working in ion chamber mode (as ΔE with the fast plastic phoswich working as E) gave a lower energy threshold and good charge resolution for $2 \leq Z \leq 13$. The BCCs combined with the fast/slow phoswichs provided a wide range of Z (charge number from 1 to 13) identification and large dynamic range (3 MeV/nucleon to ~200 MeV/nucleon for Helium) and nearly 4π sr solid angle coverage [West85, Li93]. To study nuclear matter in a highly compressed and excited environment, a nearly symmetric beam and target combination was chosen to eliminate the projectile and target spectator components in head on (central) collisions. A wide range of beam energies (15 to 115 MeV/n) was used to cover the range of temperatures of nuclear matter at which a liquid-gas phase transition predicted by theories may occur.

The following is a summary of the experiment:

Goal: Multi-fragmentation: Liquid-Gas phase transition.

Disappearance of flow: Balance energy.

Experiment No: NSCL EXPT. 88016

Reaction: $^{40}Ar + ^{45}Sc$

Beam: ^{40}Ar of 15, 25, 35, 45, 65, 75, 85, 95, 105, 115 MeV/nucleon
of about $0.1pnA$ produced by NSCL K1200 cyclotron
at charge state from 10^+ to 16^+.
The K1200 cyclotron operation parameters are shown in table 2.1.

Target: Mounted on the rotary target frame
1.6 mg/cm^2 ^{45}Sc self supporting target

Detectors: MSU 4π Array (Phase II):
- 170 Ball Phoswich Telescopes (BALL)
- 45 Forward Array Telescopes (FA)
- 55 Bragg Curve Counters (BCC)

Triggers: S_2 - system 2 trigger: any two ΔE of Ball and FA firing.
S_5 - system 5 trigger: any five ΔE of Ball and FA firing.

Table 2.1 is a summary of the beams produced by K1200 cyclotron. The charge state of Ar ions generated by the electron cyclotron resonance (ECR) source was from 10^+ for 45 MeV/nucleon to 16^+ for 115 MeV/nucleon. The cyclotron was operated at a radio frequency (RF) from 14.2 MHz to 21.5 MHz corresponding to a period of 46.5 ns to 70.4 ns for the beam burst.

2.2 Michigan State University 4π Array

Enclosed in an aluminum 32 face truncated icosahedron (soccer ball geometry with 12 pentagonal faces and 20 hexagonal faces) with a diameter (from hexagon to hexagon outer surface) of 241.3 cm, the detectors are mounted on the 2 cm thick aluminum

Table 2.1: Ar beam produced by K1200 cyclotron.

E_{beam}	charge state	f
(MeV/n)		(MH_z)
115	16^+	21.5
105	16^+	20.8
95	14^+	19.9
85	14^+	19.0
75	18^+	19.0
65	12^+	16.8
45	10^+	14.2
35	18^+	14.2

back plates – 10 pentagons and 20 hexagons, leaving two pentagons as beam entrance and exit. Each of the 30 back plates supports a detector module composed of close packed triangular pyramid shaped fast/slow plastic phoswich detectors (5 detectors for a pentagonal module and 6 for a hexagonal module) [West85, Cebr90a, Wils91]. A BCC is mounted in front of the phoswich detectors of each module. A schematic drawing of a pentagonal module is shown in Figure 2.1. In the forward direction, 45 fast/slow plastic phoswich telescopes were mounted in the exit pentagonal area covering the angular range of 7° to 18° with a solid angle coverage of 51%. This set of detectors is referred to as the forward array (FA).

Table 2.2 shows the main specifications of the three types of detectors. In column 1, the angle range is the polar angle the detector array covers with respect to beam direction. The solid angle coverage means the percentage of the solid angle the detector array covers with respect to full solid angle within the angular range specified. The energy threshold is the lowest kinetic energy the detectors can detect for different particles. We only show proton, helium and carbon as examples. The phoswich telescopes (both BALL and FA) can separate Z=1 isotopes, proton, deuteron and triton. The gain of BALL phoswich detectors was set to accept Z=1 to Z=8 and FA

Table 2.2: MSU 4π Array Detector Parameters.

Specification	Ball Phoswich	FA Phoswich	BCC
Angle Range (degree)	23 to 157	7 to 17	23 to 157
Solid Angle Coverage(%)	83	47	83
Z identification	Z=1 to 8 †	Z=1 to 13 †	Z=2 to 12 ‡
Energy Threshold(MeV/n):			
Proton	11	12	-
Helium	15	12	3
Carbon	27	21	4

† Both BALL and FA phoswich has Z=1 isotope resolution. (p, d, t).

‡ The BCC gain is set to accept $2 \leq Z \leq 12$

phoswich to accept Z=1 to Z=13 and BCC can identify Z=2 to Z=12.

2.3 Bragg Curve Counter

The bragg curve spectrometer was first proposed by Gruhn et al [Gruh82], then studied and improved by others [Schi82, Asse82, Oed83a, Oed83b, Mcdo84, Moro84, Shen85, Kott87, Cebr91]. The BCC has several advantages: It has a low energy threshold; It can be made to subtend large solid angle with good Z resolution and linear energy response. The particles go through an electric field parallel to the path of the particle which is especially suitable for a spherical geometry where particles emitted from the target go through an radial field inside the BCC. To accomplish the goal of maximizing the solid angle coverage and minimizing the low energy cut off, hexagonal or pentagonal pyramid G10 fiberglass casings are mounted directly on the phoswich module to make a close-packed detector array inside the 4π Array. A 2.5 μm thick aluminum coating is evaporated on the entrance surface of the phoswich module which serves as the BCC anode. The anodes on the first ring of five hexagonal modules (the first ring from the beam axis) are further segmented into six segments

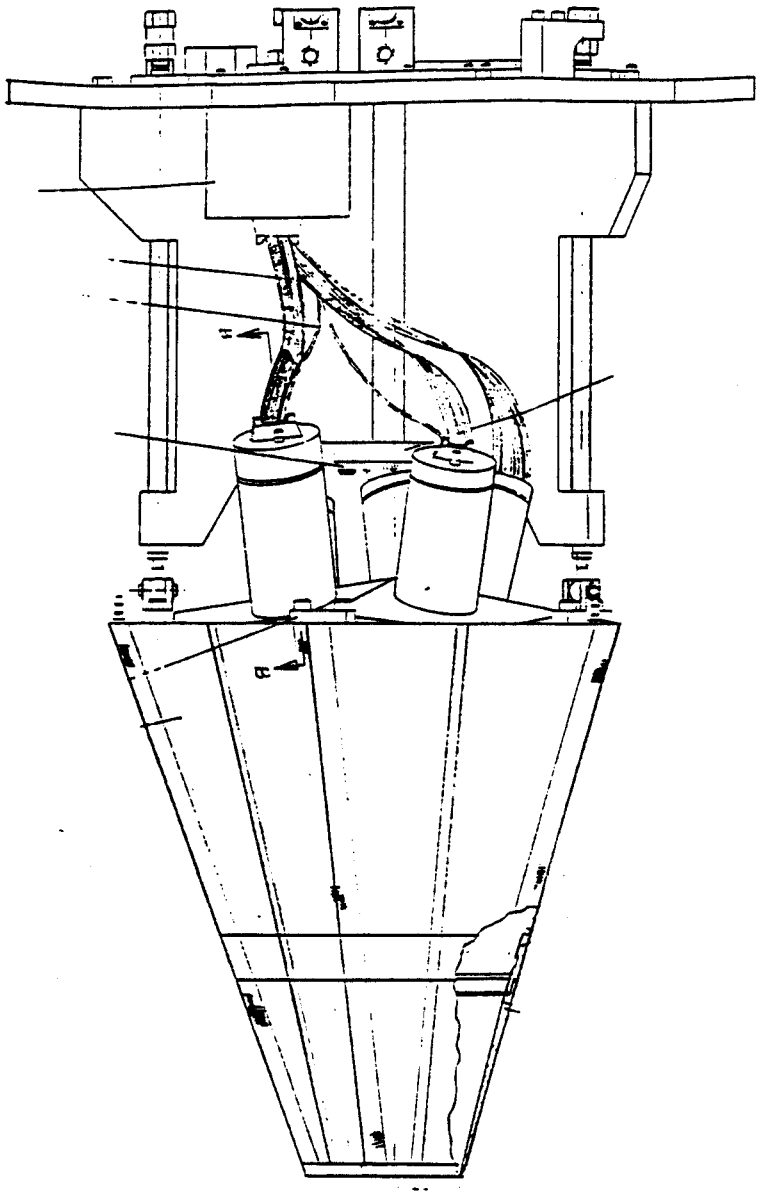

Figure 2.1: A pentagon module of MSU 4π array.

which give six independent outputs corresponding to the six phoswich telescopes. The entrance window is made up of a 900 $\mu g/cm^2$ thick, aluminized kapton which was epoxy-bonded on a stainless steel window frame with 1 cm spacing supporting grid. The distance between the cathode and the anode is 13.36 cm .

A Frisch grid made of 12.5 μm gold plated tungsten wires with a 0.5 mm spacing is epoxy-bonded with silver epoxy on a G10 frame with a conducting copper strip. The Frisch grid to anode distance is 1 cm. The Frisch grid is connected to ground potential to shield the positive ion induced charge. On the inside surface of the G10 BCC cover, 21 field shaping copper strips are installed. The 21 strips are linked by twenty-one 1.55 MΩ resistors from Frisch grid to the cathode to provide a radial electric field. A layer of silver conducting paint covers the BCC and is connected to ground to shield the detector from the electromagnetic interference. The BCCs are filled with P5 gas (95% Ar and 5% CH_4) with a pressure of 500 torr. The anode potential is set at +200 V and cathode at -1200V. The distance from the entrance window of BCC to the target is 17.27 cm. The entering charged particles ionize the gas and produce electron-ion pairs. The electrons and ions drift along the radial field in opposite directions. Taken from anode, the BCC signal feeds into a charge-sensitive pre-amplifier mounted on each module inside the vacuum chamber to reduce the signal to noise ratio. An integrated signal is obtained at the output of the pre-amplifier. The schematic of the preamplifier is shown in figure 2.3. The signal is further amplified by a shaping amplifier. The shaping amplifier gives a differentiated fast signal whose peak is proportional to the charge and an one stage differentiation and two stages of integration of the slow signal whose peak is proportional to the energy deposited by the detected particle. The time constant of the slow signal is $5\mu s$. The slow signals go into peak sensing ADCs (Silena 4418/v). The NSCL data acquisition system is used to read the ADCs.

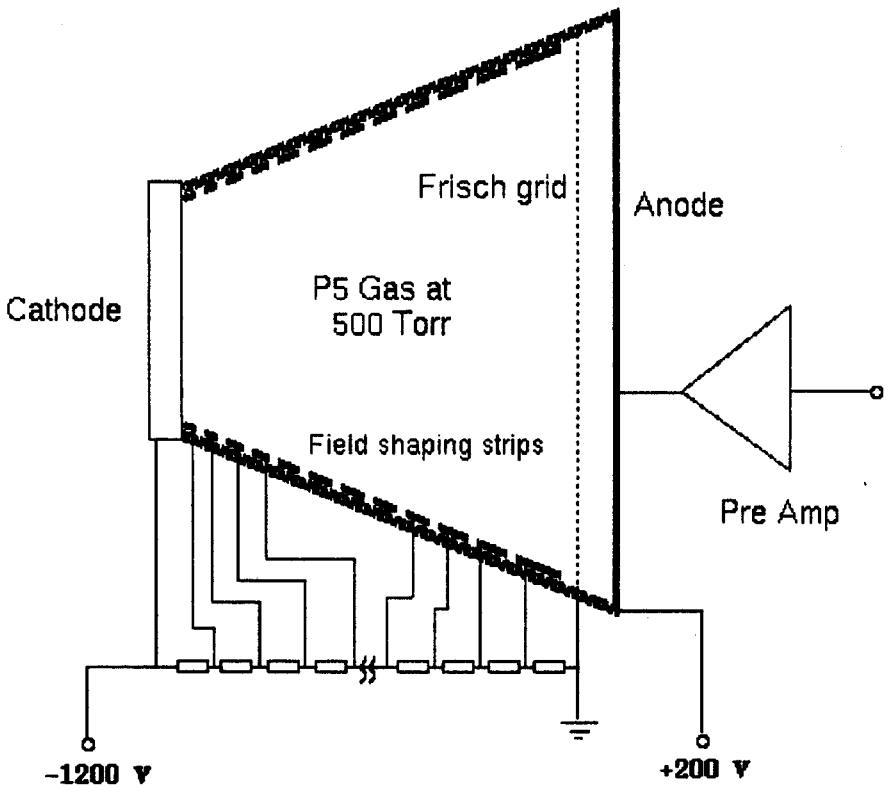

Figure 2.2: Schematic diagram of the MSU 4π Bragg Curve Counter (BCC).

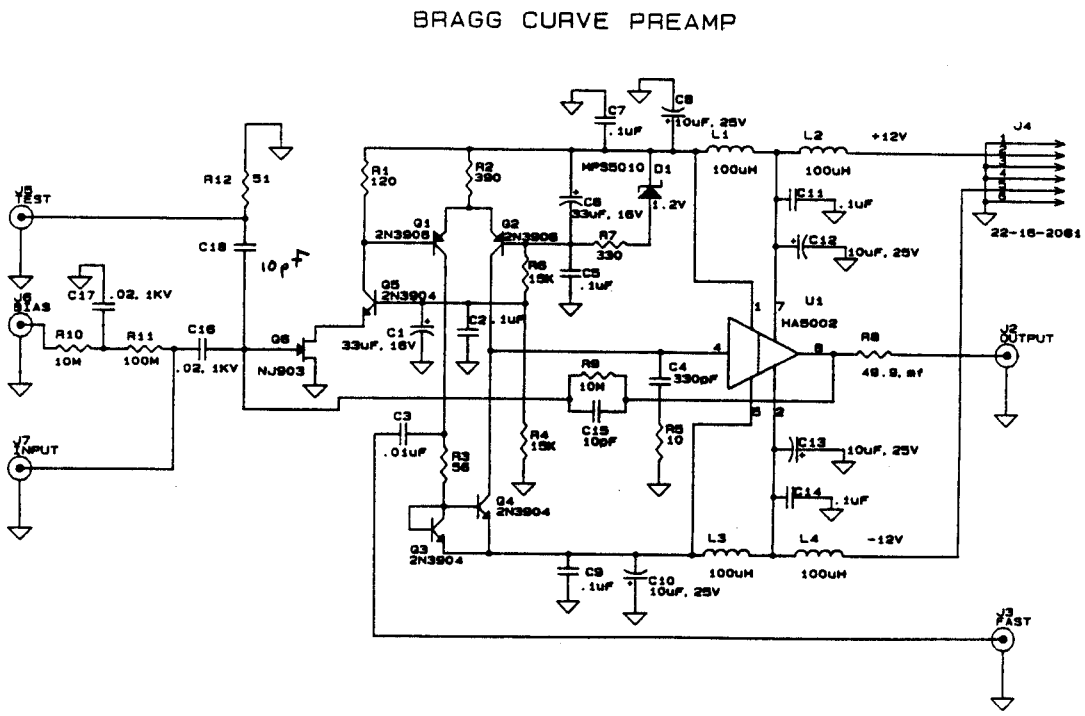

Figure 2.3: Schematic of the preamplifier used for the Bragg Curve Counters.

2.4 Phoswich detectors

The 170 ball fast/slow plastic telescopes are made of 3 mm thick Bicron BC-412 fast plastic scintillator with a rise time of 1.0 ns and a fall time of 3.3 ns optically coupled to a 25 cm thick BC-444 slow plastic scintillator with a rise time of 19.5 ns and a fall time of 179.7 ns. The ball hexagonal modules each cover a solid angle of 6×65.96 msr and the pentagon module covers a solid angle of 5×49.92 msr. The 45 forward array telescopes are made of the same fast/slow plastic as the ball phoswich detectors except that the fast plastic ΔE counters are 1.6 mm thick. There are 30 cylindrically shaped telescopes each covering 3.02 msr solid angle and 15 pyramid shaped telescope each covering 2.75 msr solid angle.

The light signal produced by energetic incident charged particle is transformed to an electronic signal by a 8 stage photo-multiplier tube. The fast/slow phoswich signal is shown schematically in Figure 2.8. The signal is separated into ΔE and E using a fast gate and a slow gate. The fast and slow signal are recorded separately using Lecroy FERA 4301b charge to digital converter. Two dimensional spectrum of ball fast signal (ΔE) vs. slow signal (E) in electronic channels is shown in Figure 2.4 and the forward array two dimensional spectrum is shown in Figure 2.5. The density of the scattering plots is proportional to the logarithm of the counts. The lines visible in the two dimensional spectra show the particle identification. The actual electronic resolution is 2048 by 2048 channels.

2.5 Data Reduction

The experimental data was stored event-by-event on 8mm magnetic tapes in the NSCL event buffer format. Because the MSU 4π Array is a permanent device with large number of detectors, the calibration and data reduction must be as standardized

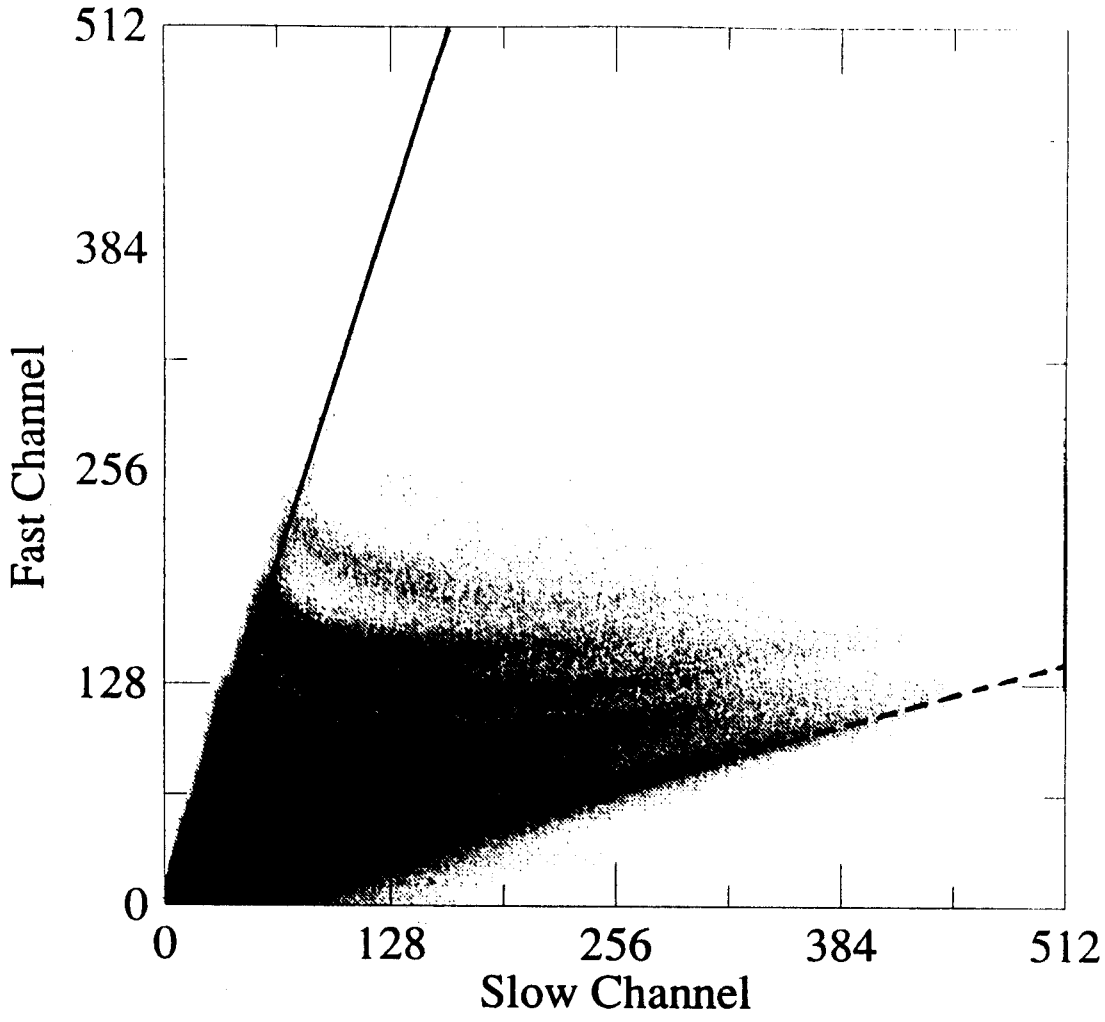

Figure 2.4: Ball phoswich fast electronic channel vs. slow electronic channel from Ar + Sc at 75 MeV/nucleon at 23°. The particles close to the solid line (punch-in line) are the particles stopped in fast plastic and the particles close to the dashed line (neutral line) are neutral particles.

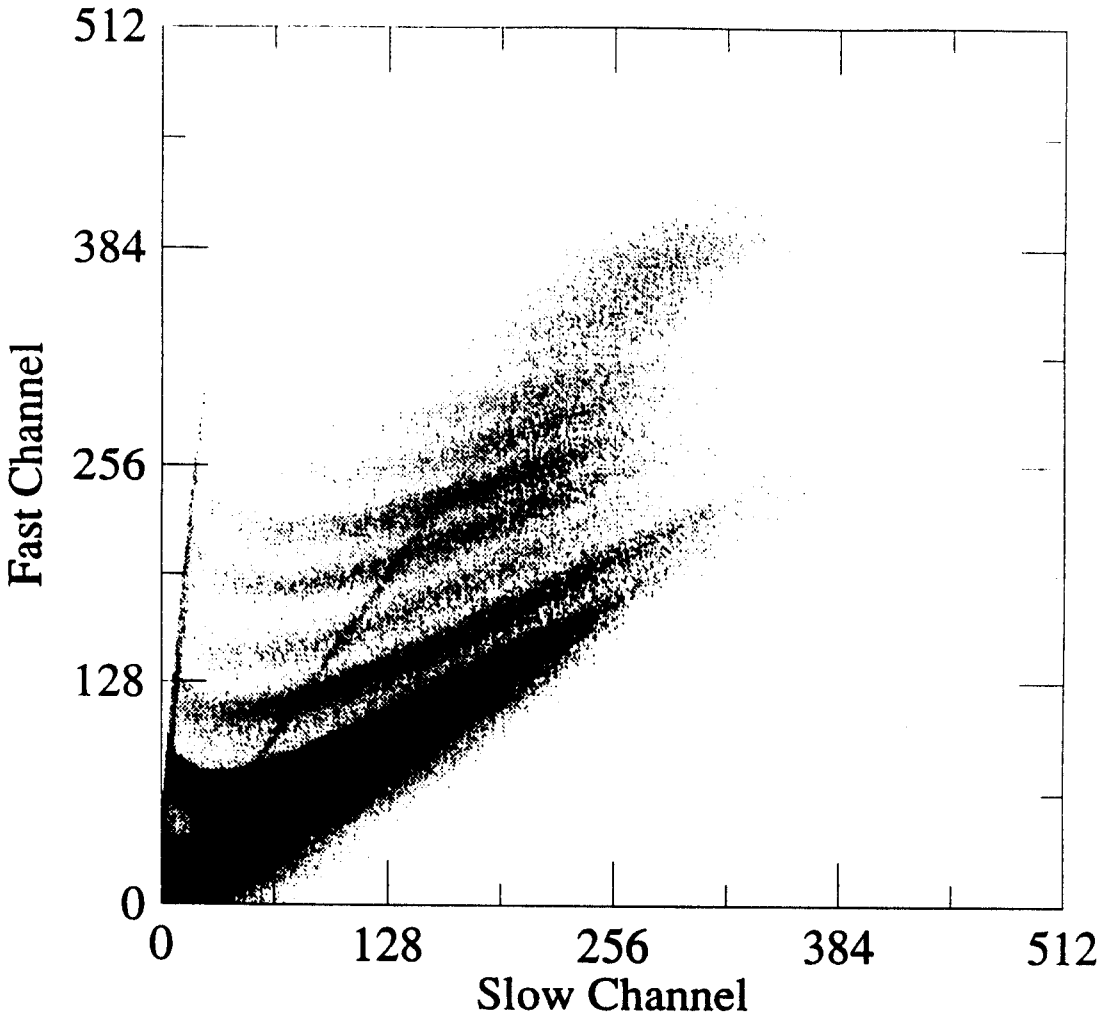

Figure 2.5: Fast electronic channel vs. slow electronic channel for a forward array detector at 7° for Ar + Sc at 75 MeV/nucleon.

as possible. To cope with the large number of detectors and the diverse experimental capabilities of the device, a calibrated template method is used for both the phoswich detectors and BCCs. The data reduction includes 3 steps:

- Using the energy response function obtained in calibration runs and the range-energy program (DONNA [Meye81]), we generate a standard line spectrum called a template (shown as Figure 2.9) and the corresponding look-up tables. For any point in the two dimensional template, the physical quantities such as Z, A, kinetic energy can be found from the tables.

- Matching all the two dimensional spectra of each detector to the template, we obtain a parameter file which contains all the information of the matching transformation from the original spectra to the matched spectra.

- Using the look up tables and the parameter files, we make physics tapes that contain information including multiplicity, particle charge number (Z), particle mass number (A), polar angle (θ), and azimuthal angle (ϕ) of all the events.

After the templates and look up tables are made, the energy calibration and particle identification is reduced to the relatively simple task of matching each detector to the template by varying the gain of the ΔE and E. A graphic matching program was used to use VAX workstation to obtain the gain parameters. The parameters of the matching is stored in a parameter file. The parameter file and look up tables are used to run the physics tape program for making physics tapes.

2.5.1 Phoswich Calibration

For a detector calibration there are two goals, to obtain the particle identification and to calibrate the kinetic energies for the identified particles.

The particle identification is done by using a standard spectrum and transforming the two dimensional spectrum of fast ΔE channel vs. slow E channels into a reduced two dimensional spectrum. A representative two dimensional histogram is shown in Figure 2.4. The particles close to the solid line, the punch-in line, are the particles stopped in the fast plastic. The non zero E channel on the punch-in line is due to the mixing of the fast and the slow light signal shown in Figure 2.8. The particles close to the dashed line are neutral particles. Thus the dashed line is called neutral line. The slope is also due to the mixing of fast and slow signals. The two dimensional histogram is transformed to the reduced channel, CH_f and CH_s using the following equation: [Cebr90a].

$$\begin{aligned} CH_f &= (\Delta E_{channel} - Y_0) - (E_{channel} - X_0)M_n \\ CH_s &= (E_{channel} - X_0) - (\Delta E_{channel} - Y_0)/M_p, \end{aligned} \tag{2.1}$$

where $\Delta E_{channel}$ and $E_{channel}$ are fast and slow electronic channels recorded from the experiment, the CH_f and CH_s are reduced channels which are proportional to the fast and slow light signal [Cebr90a], M_p and M_n are the slope of the punch-in line and the neutral line respectively, X_0 and Y_0 are the crossing point of the neutral line and the punch-in line, which represent the offset of the ADCs. Figure 2.6 shows a reduced two dimensional spectrum of CH_f vs. CH_s for a ball phoswich at angle 23° and Figure 2.7 shows a reduced two dimensional spectrum of forward array.

A set of gate lines are then calculated for the transformed two dimensional histogram to be used as a template for particle identification. The ball phoswich template is shown in Figure 2.9 and the forward array template is show in Figure 2.10. From the calibration runs, we get the following response function: [Cebr90a]

$$\begin{aligned} CH_s &= aE_s^{1.4}/A^{0.4}Z^{0.8} \\ CH_f &= bE_f^{0.5} - c, \end{aligned} \tag{2.2}$$

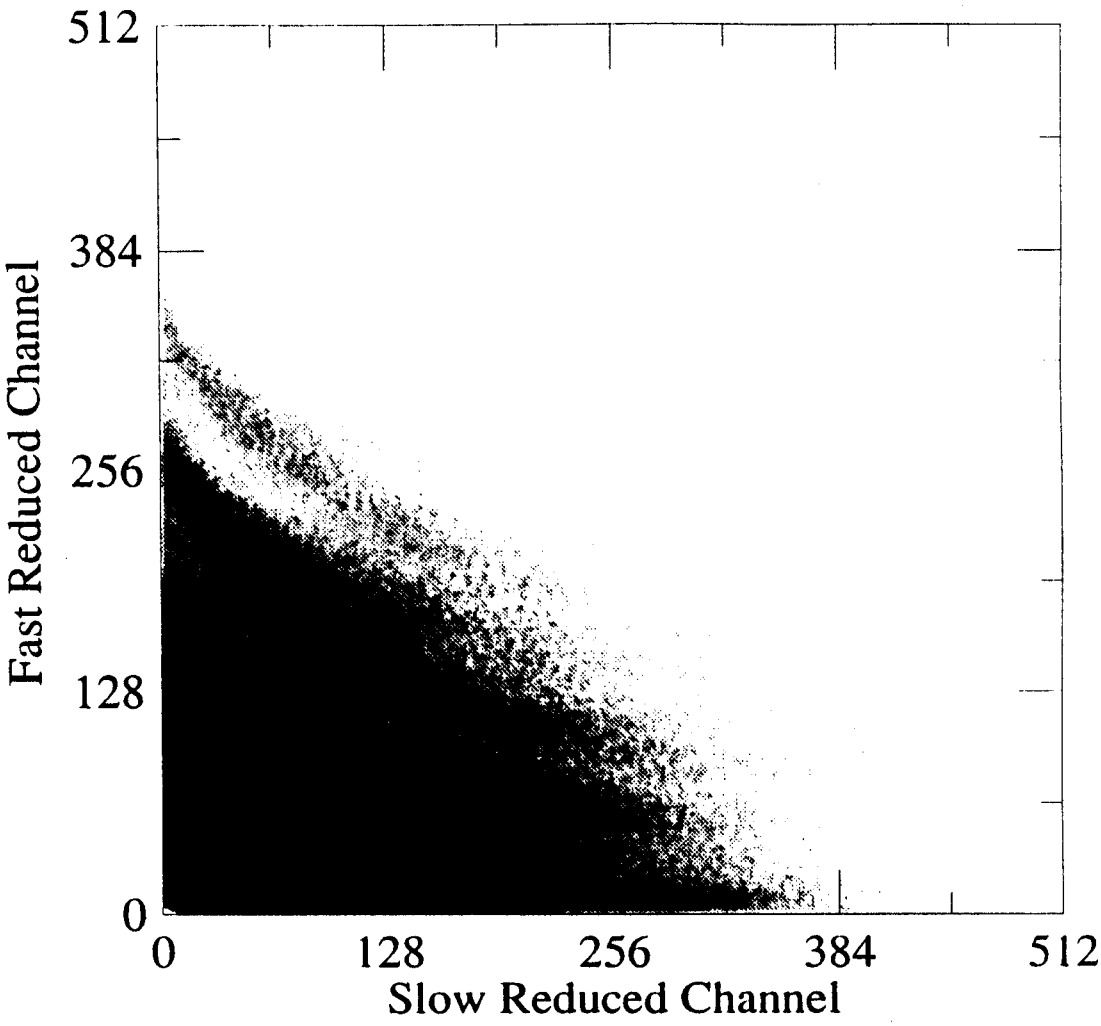

Figure 2.6: Fast reduced channel vs. slow reduced channel for a ball phoswich detector at 23° for Ar + Sc at 75 MeV/nucleon.

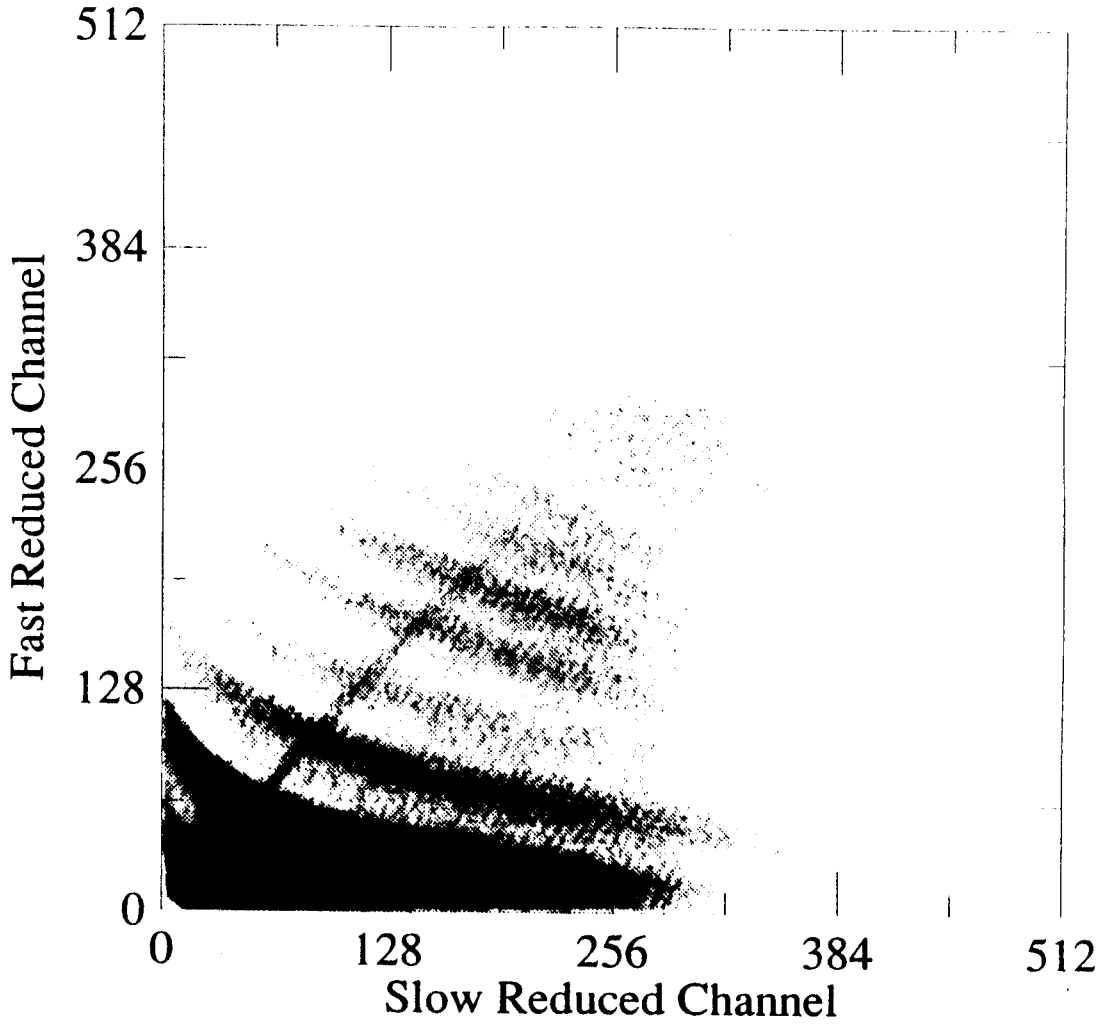

Figure 2.7: Fast reduced channel vs. slow reduced channel for a forward array detector at 7° for Ar + Sc at 75 MeV/nucleon.

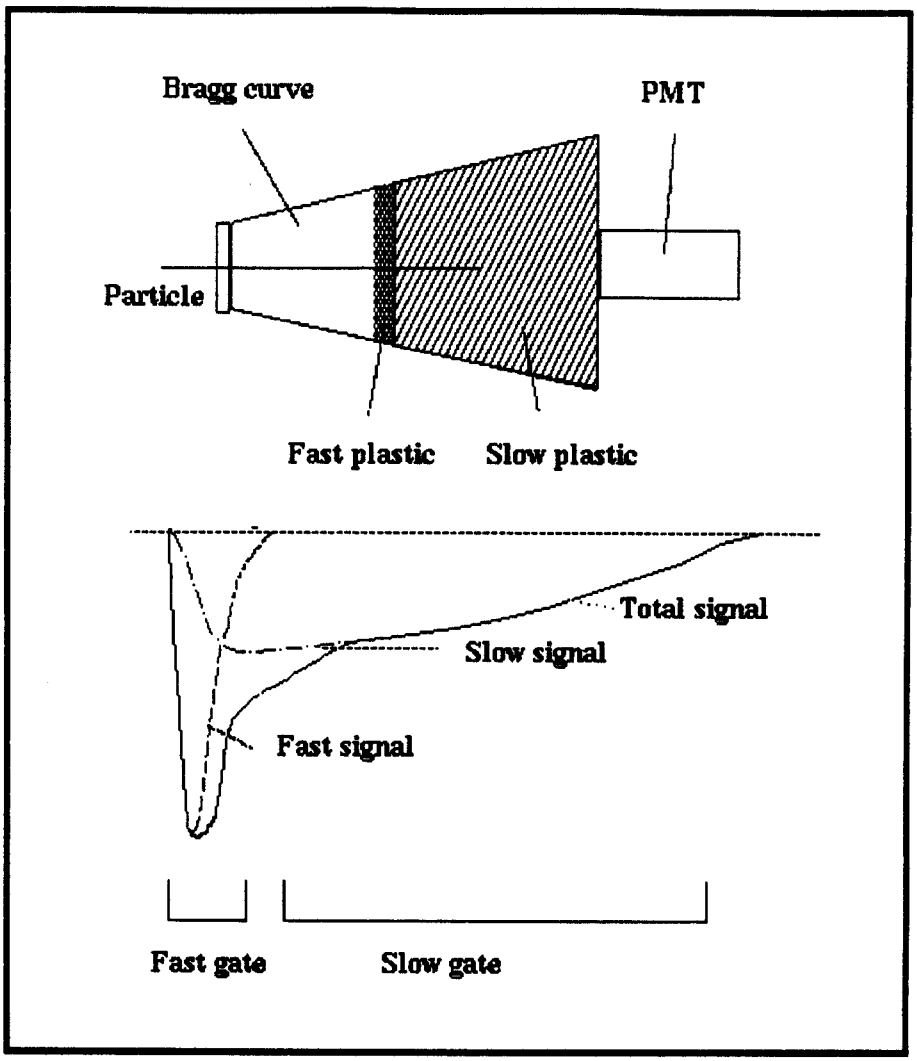

Figure 2.8: The fast/slow plastic telescope, the signals and the gates.

where the CH_s and CH_f are the slow plastic and fast plastic reduced channels, E_s and E_f are the particle energy loss inside the slow and fast plastic, respectively. The quantities a, b and c are the gains and offsets which are determined by fitting the measured spectra to the response function through range-energy calculations. The range-energy program called DONNA [Meye81] was used. For a given particle of Z and A with certain kinetic energy, the E_s and E_f are calculated using DONNA given the density and the thickness of all the material along the particle path. Therefore for a given particle with Z and A one can calculate the relation of CH_s vs. CH_f shown as Figure 2.11. From bottom to top, the curves are for proton, deuteron, triton and Z=2 to Z=8 (with the most probable isotope A). We fit the calculated particle lines of 2.11 on the particle lines of the experimental two dimensional spectrum 2.4, we obtain the constant a, b and c.

From the template gate lines we can identify the Z and A of a particle. To reduce computational time for physics tape program, a look-up table with 512 by 512 resolution was made which gives particle Z (charge number) and A (mass number) according to the slow and fast electronic channels. The most probable isotope mass number for $Z > 1$ was used. Along with the particle identification table, a template is also made in 512 by 512 resolution to be used as a standard spectra for matching the experimental data. The ball template is shown in Figure 2.9 and the forward array template shown in Figure 2.10. The solid lines are the gate lines.

Two sets of tables and templates are made for ball phoswich detectors and forward array phoswich detectors separately. Then the experimental two dimensional spectra of 215 detectors for each beam energy are matched into the template using the matching program. The gain factors and offsets are then written in the parameter files.

Combining the response functions (equation 2.2), using the constants obtained by

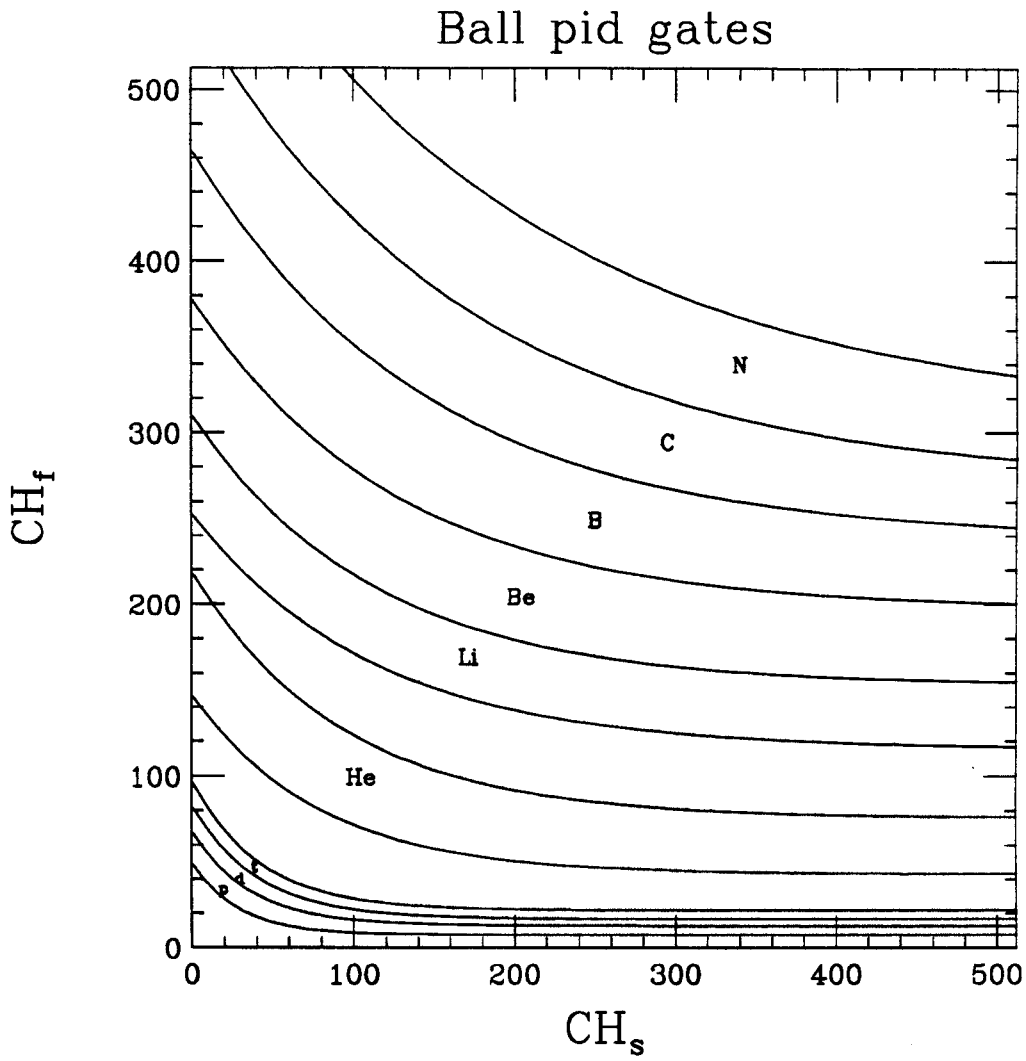

Figure 2.9: The particle gate lines for p,d,t and Z=3 to 4 with the most probable isotopes.

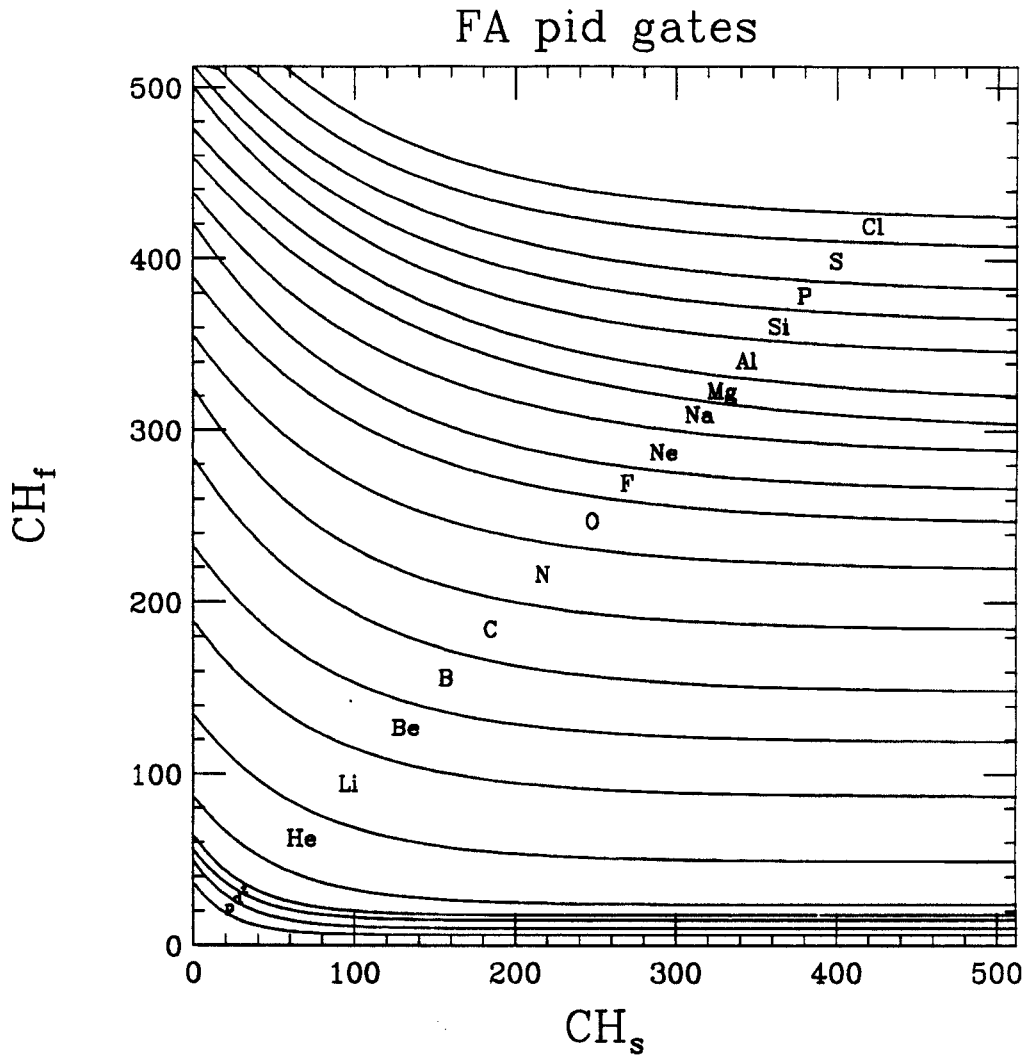

Figure 2.10: The particle gate lines for p,d,t and Z=3 to 4 with the most probable isotopes for forward array detectors.

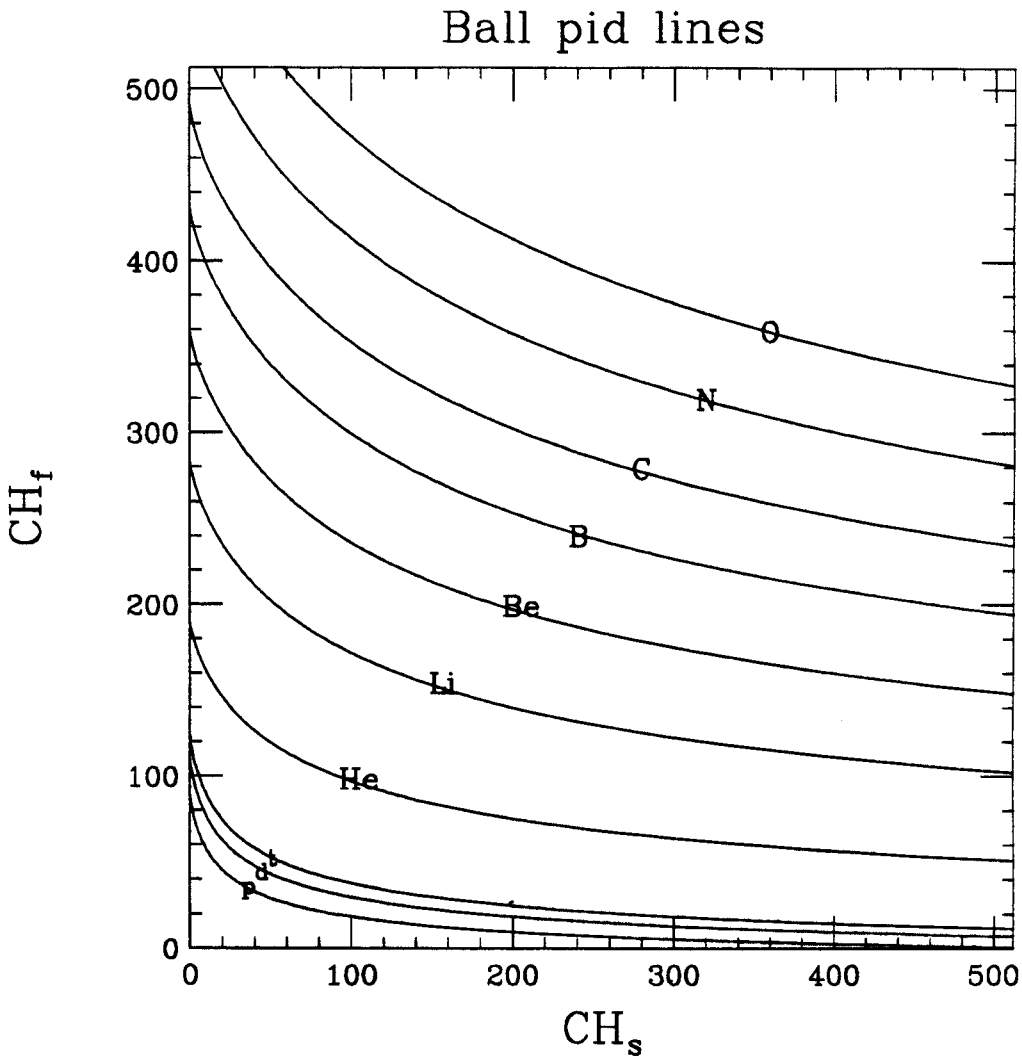

Figure 2.11: The particle lines for p,d,t and Z=3 to 4 with the most probable isotopes calculated from energy loss and response function.

the fitting, and the range-energy program (DONNA), one can determine the incident energy of the particle. Then an energy table was made to convert the channel numbers to incident particle kinetic energy.

2.5.2 Bragg Curve Calibration

Prior to the mass production of all 32 BCCs (30 working modules and two spares), a prototype module was made and a calibration run was performed [Cebr91]. The calibration run was done at NSCL using a beam of ^{40}Ar produced by the K500 cyclotron. The prototype module was placed inside the S320 spectrometer. A 4 MeV/nucleon ^{40}Ar was stopped in the gas counter and an energy resolution of 2% was determined by the ratio of FWHM(full with half maximum) and the beam energy. Then a 35 MeV/n ^{40}Ar beam bombarded an target 15 cm away from the entrance window of the BCC. For the particle stopped inside the gas counter, the charge number can be identified by BCC's E signal vs. Z signal as shown in Figure 2.12. For the particle punching through the gas counter and stopping inside the fast plastic of the phoswich, the charge number (Z) of the particle can be identified by the BCC's E channel vs. ΔE (fast plastic) channel as shown in Figure 2.13. Clear Z lines from proton to Mg can be seen. To study the energy response function, the fragments produced by the reaction of Ar + Au were selected by the spectrometer at different rigidities. The result of the study shows that the energy response of the detector is linear and independent of the charge and mass of the incident particle (Figure 2.14) [Cebr91])

The same method was used to calibrate the two dimensional spectra of BCCs' E signal vs. fast plastic signal channel as for the fast/slow plastic. The response function of a particle stopped in the fast plastic is the same as the response function of a particle stopped in slow plastic and the response function of BCC is linear as

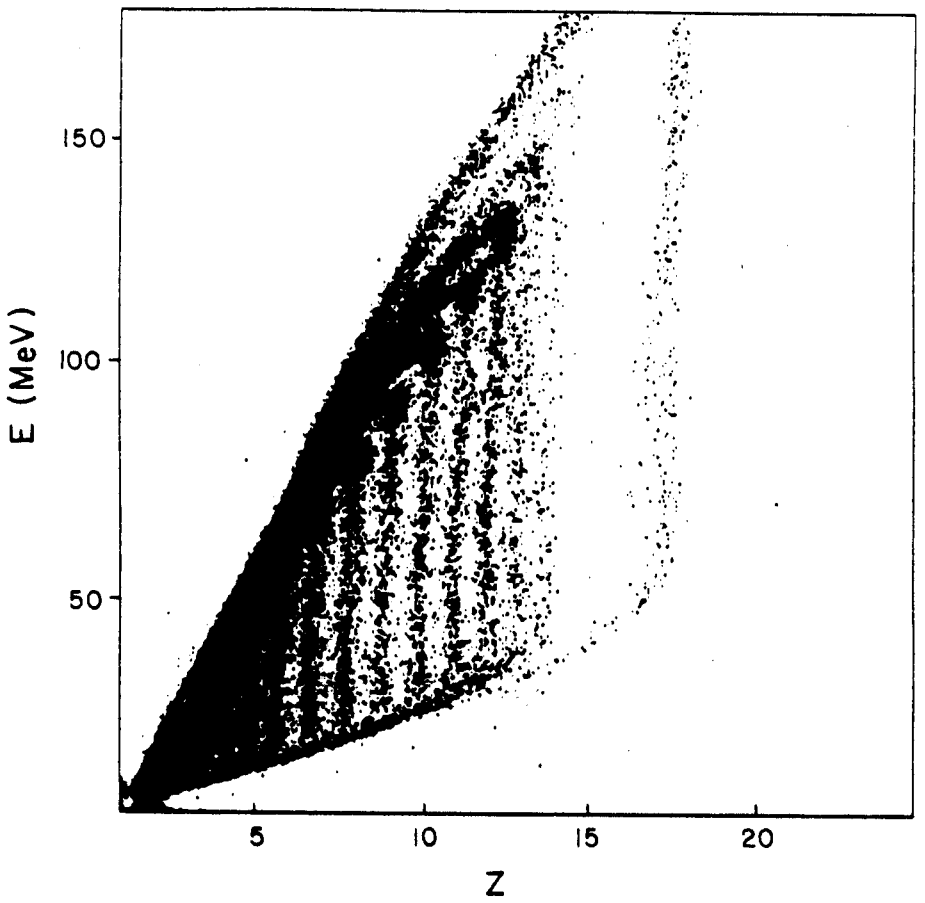

Figure 2.12: BCC E channel vs. BCC Z channel

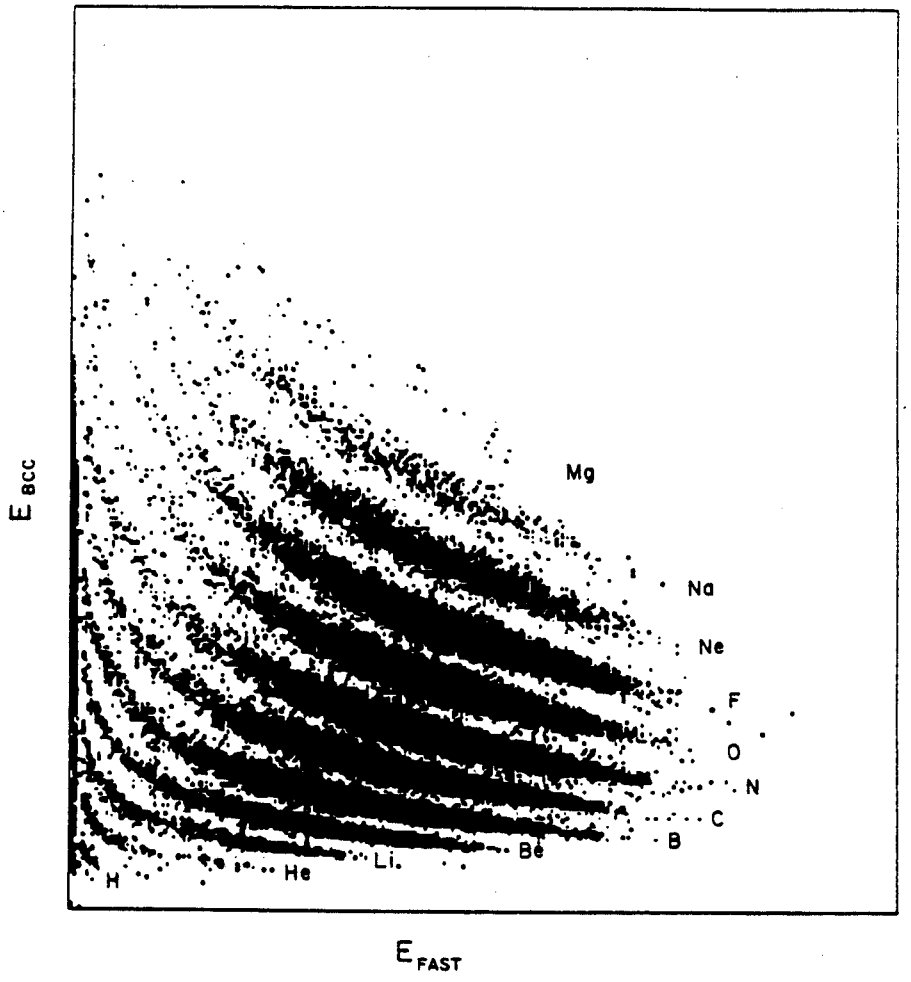

Figure 2.13: BCC E channel vs. ΔE plastic channel

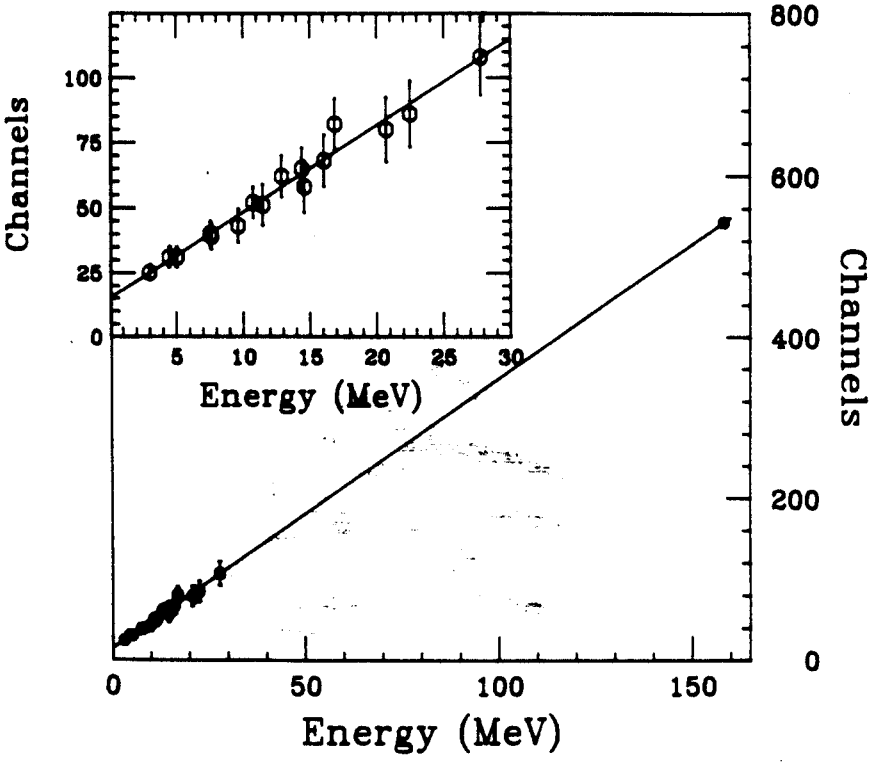

Figure 2.14: Energy response of the BCC

proved by our calibration run. The response function as following:

$$\begin{aligned} CH_f &= \alpha E_f^{1.4}/(A^{0.4}Z^{0.8}) \\ CH_{BCC} &= \beta E_{BCC}, \end{aligned} \tag{2.3}$$

where CH_{BCC} is the BCC's E electronic channel and α, β are constants. Figure 2.15 shows a typical experimental two dimensional spectrum of BCC's E channel vs. fast plastic channel and Figure 2.16 shows the template for the BCC's E vs. ΔE (fast plastic). The solid lines are the valleys of the spectra. All the detectors are then matched to the template with two gain factors and two offsets in the x and y direction. The gain factors and offsets are written in a parameter file for later use with the physics tape program.

Also look-up tables of Z, A, and kinetic energy, E_k, are made from the template for physics tape program.

The advantage of the above method is three fold:

- One does not have to calibrate the detectors one by one. A program was used to match all the spectra to the templates which is much faster and more accurate.
- The calibration only has to be done once and the templates can be used for all the experiments done with the same detector set up. The templates are independent of the electronic gain.
- The method provided a foundation for a future fully automated computerized data reduction system.

Then the physics tapes were made which only contain the physics quantities such as multiplicity, Z, A, θ, ϕ, E_k and detector number.

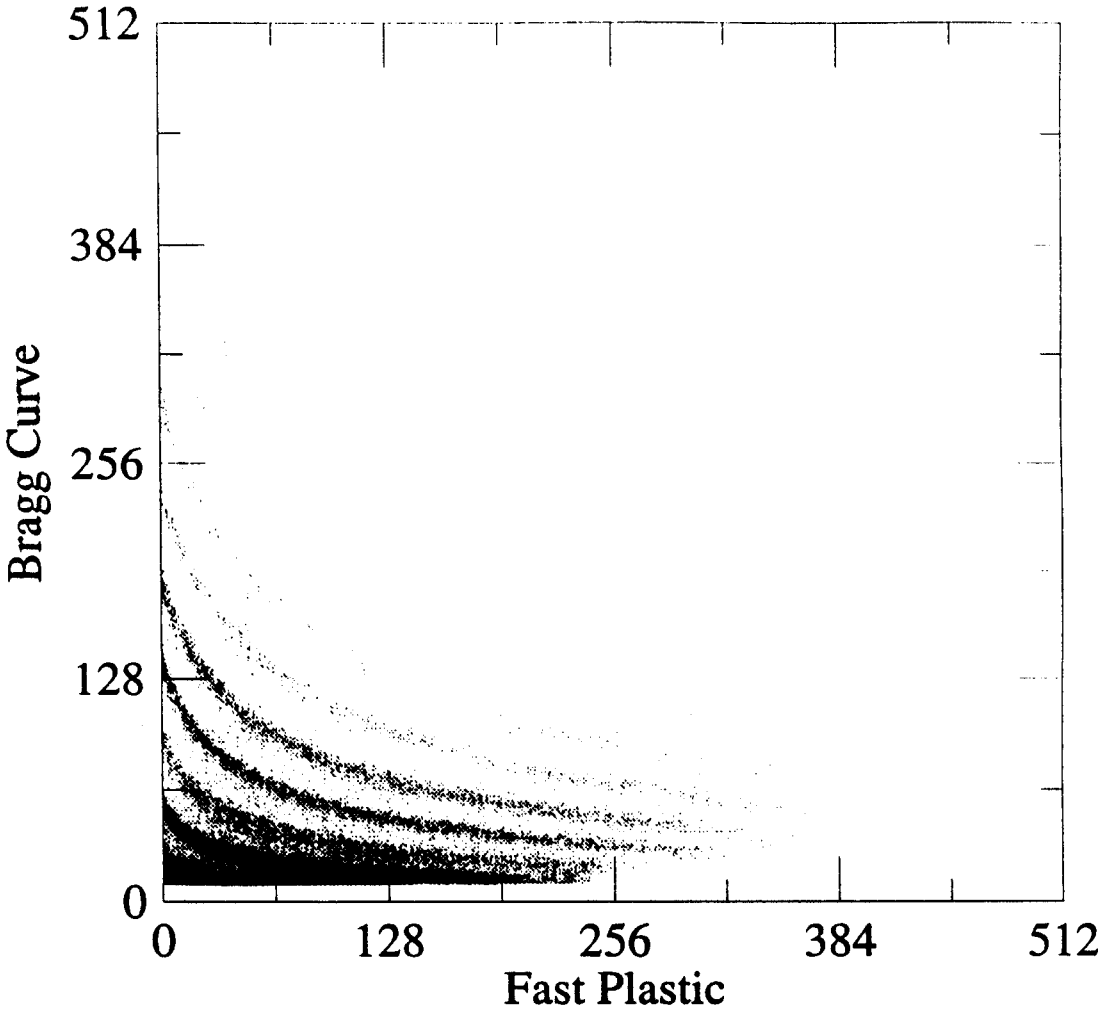

Figure 2.15: Experimental result of BCC electronic channel vs. Fast plastic electronic channel for Ar + Sc at 35 MeV/nucleon

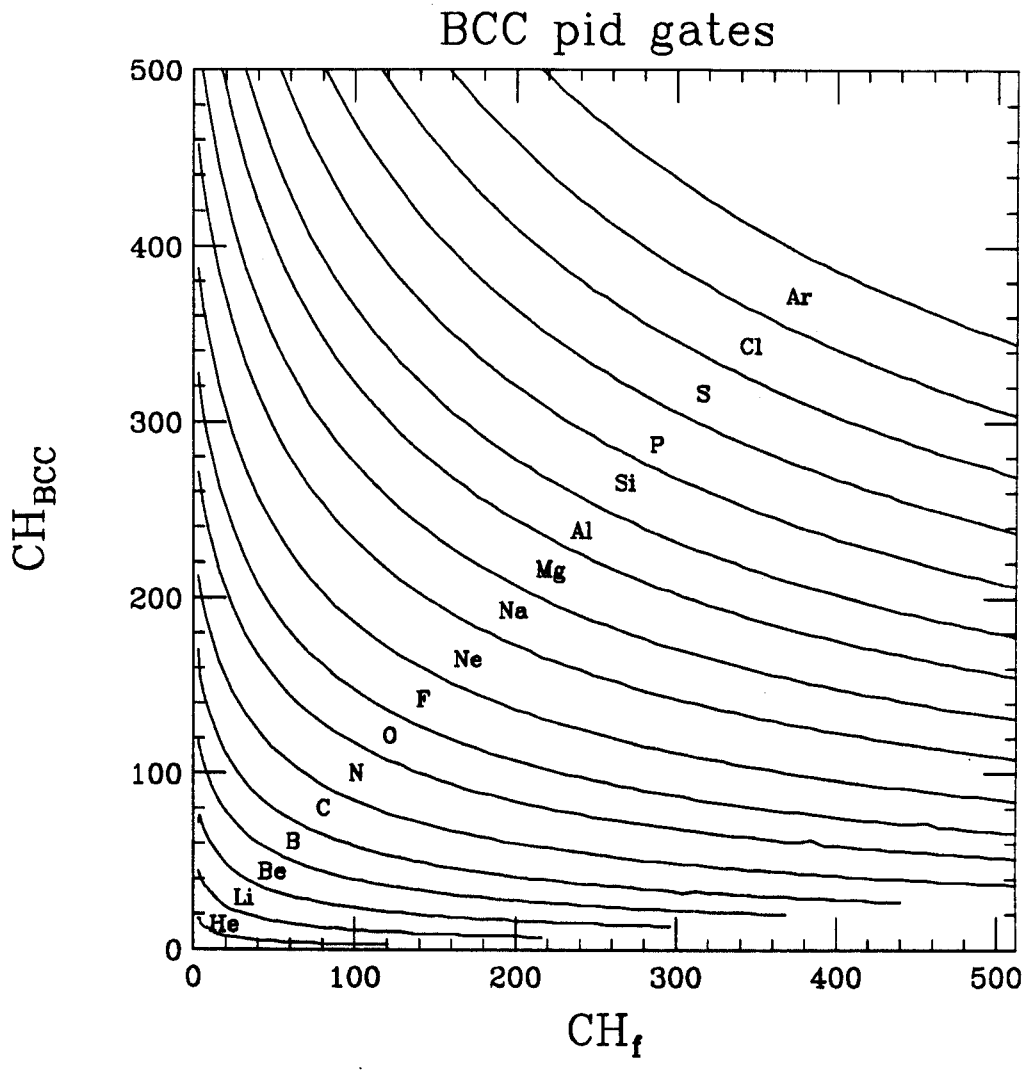

Figure 2.16: The particle gates Z=2 to 18 with the most probable isotopes for bragg curve detectors.

Chapter 3

Event Characterization

3.1 Introduction

A heavy ion reaction is conducted by accelerating projectile nucleus, P, to an initial momentum, **p**, colliding it with a target nucleus, T, with an initial impact vector, **b** (see Figure 3.1). After the collision, the production particles are detected by a detector system. The beam momentum is normally characterized by the beam kinetic energy per nucleon (MeV/nucleon) and the beam direction, which by convention is the z axis. An event is one collision of projectile and target. Event characterization involves the measurement of **b**.

Early inclusive heavy ion reaction measurements generated great interest [West76,

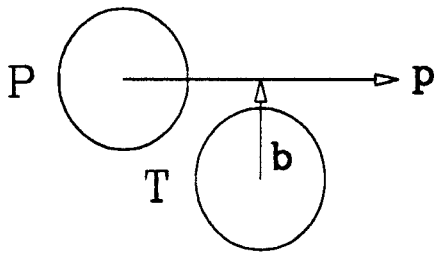

Figure 3.1: Three initial conditions for heavy ion reaction: reaction system, P+T, projectile momentum, **p**, impact vector, **b**

Goss77, Goss78, West82, Awes81, Awes82, Jaca87]. However the ambiguity of the inclusive measurements, which sum over all impact vectors, pushed the experimentalists to adopt much more advanced and expensive techniques to perform global measurements. These 4π measurements can discriminate head-on central collisions from peripheral collisions by gating on some global observable. First plastic ball experiments showed much promise [Gutb89a, Gutb89b]. Strong dynamical collective motions were observed. Dynamical collective motion can be used to determine both impact parameter, i.e. the amplitude of impact vector, and the reaction plane, i.e. the plane composed by impact vector and beam direction. These are the two initial conditions of heavy ion reaction. Prior to any study, the determination of the impact parameter and the reaction plane have to be studied and the errors associated with the different techniques have to be understood.

There are two major physical ideas underlying heavy ion reactions: **statistics** and **dynamics.** Statistical physics means that there is large randomization or "thermalization" during the reaction. Whether one can apply statistical theories and concepts to a system containing only 10^2 particles is still an open question, but the kinetic energy distributions do exhibit strong statistical behavior [Jaca87, Wada89]. The dynamics is shown by the collective motion, which is strongly dependent on initial conditions. This dependence on the initial conditions can be used to estimate the initial conditions.

If the reaction process is purely dynamical, then the global observables are monotonic functions of impact vector. The impact vector can then be measured with a high degree of accuracy. However the system is subject to statistical fluctuations, the relation between global observable and impact vector is not a single valued monotonic function. Rather it is the mean value of the global observable which is monotonically correlated with the impact vector. Thus, the determination of the impact vector is

alway accompanied by a large error bar. The direction of impact vector is expressed in terms of the reaction plane defined by the beam vector and impact vector. The projectile side of the reaction plane normally defined to be the positive direction, which can be opposite to the direction of impact vector if the interaction is attractive or parallel to the direction of impact vector if the interaction is repulsive.

If the projectile, its kinetic energy and target are chosen, the impact vector will determine the initial condition such as how much excitation energy is going to be deposited into the system and provide a reference frame for the study of collective motion. To determine the intial conditions perfectly, a complete measurement of all the production particles is needed. However the limitations of the detector resolution and detector coverage in solid angle and kinetic energy make the determination of the impact vector more uncertain.

Reaction plane determination was first attempted by applying a momentum tensor (see Equation 3.1) [Gutb89a] and sphericity analysis borrowed from high energy physics [Bran79, Wu79]. Using this method, dynamical properties such as flow angle have been observed. The reaction plane can be found using the eigen vector associated with the largest eigen value of the momentum tensor. Because of the large fluctuation caused by the finite multiplicity, effort has been put into developing different techniques to determine the reaction plane. Major progress was made by Danielewicz and Odyniec who initiated the transverse momentum method to determine the reaction plane [Dani85].

Impact parameter determination was done by cutting the reaction events based on its charged particle multiplicity. The participant-proton multiplicity defined as protons bound in light particles ($Z \leq 2$) by Doss et al. were throughly studied and used by plastic ball group [Doss86, Doss87, Gutb89a, Gutb89b]. Then some simulation studies were done comparing different global observable as a function of impact

parameter to see which one has the strongest correlation with the impact parameter [Ogil89b, Tsan89]. But since the studies are based on certain theoretical models that contain different dynamical and statistical ingredients, the results are not general.

In this chapter, first we introduce the methods of determining the reaction plane and the impact parameter. The errors associated with the different methods of the reaction plane and the impact parameter determinations are also going to be addressed.

3.2 Reaction Plane Determination

The dynamical measurement of heavy ion reactions started when the first 4π detector was put into operation [Doss86, Doss87, Gutb89a]. The reaction plane determination is based on collective motion studies. Phase space event shape analysis was first done using the sphericity tensor defined as:

$$F_{ij} = \sum_{n=1}^{m} p_i(n) p_j(n) \omega(n), \tag{3.1}$$

where $i, j = x, y, z$; $p_i(n)$ are x, y or z components of the momentum of nth particle of an event with a multiplicity m in center of momentum frame; and $\omega(n)$ is the weighting factor. Diagonalizing the tensor **F** gives three major axes associated with three eigen values which will give the flow angle defined to be the angle of the axis with the largest eigen value with respect to beam axis. The phase space shape also can be characterized by the three eigen values [Fai83]. However, the method is limited by the statistical fluctuations due to finite multiplicity. To cope with the large fluctuations, a transverse momentum method was proposed by Danielewicz and Odyniec [Dani85]. The transverse momentum method was successfully used for analysing plastic ball and streamer chamber experiments. Transverse momentum flow was observed (see Figure 5.1) [Doss86, Doss87, Gutb89b]. The dynamical studies then extended to lower energy in search of the disappearance of flow. Due to the long range mean

field attraction and short range nucleon-nucleon repulsion theoretical model such as Boltzmann-Uehling-Uhlenbeck (BUU) predicted that flow will change direction at lower beam energies. This change will give an observable called balance energy at which the flow disappears. When 4π detectors were built and used in intermediate energy, the lower multiplicity led to much larger fluctuations. To deal with the low multiplicities, a new technique called "azimuthal correlation" method was developed by Wilson et al. [Wils92].

In this section we will introduce the transverse momentum method and the azimuthal correlation method and compare the two methods.

3.2.1 Transverse Momentum Method

Q vector:

Transverse momentum method determines the reaction plane by defining a transverse vector:

$$\mathbf{Q} = \sum_{n=1}^{m} \omega_n \mathbf{p}_n^t \tag{3.2}$$

$$\omega_n = \begin{cases} 1 & \text{if } y_n > y_c + \delta \\ -1 & \text{if } y_n < y_c - \delta \\ 0 & \text{otherwise,} \end{cases}$$

where $\mathbf{p}_n^t$ is the transverse momentum of nth particle of an event with multiplicity m, ω_n is a weighting factor, y_n is the rapidity of nth particle, y_c is the center of mass rapidity, and δ is a cut to ignore the contribution from isotropic mid-rapidity particles which contribute to fluctuations.

The reaction plane is defined by $\mathbf{Q}$ and beam vector. The direction of $\mathbf{Q}$ is used as projectile side of the reaction plane, by convention taken as the P_x axis. The goodness of the method can be tested by randomly subdividing each event into two sub-events.

For each sub-event a $\mathbf{Q_i}$ $(i = 1, 2)$ can be calculated. Then the distribution of the azimuthal angle ϕ between the two $\mathbf{Q}$s is studied. Also Monte Carlo events were generated by mixing particles from different events into new events. The Monte Carlo events are then divided into two sub events. The experimental events showed a peak at 0 degree comparing with the flat distribution of the Mount Carlo events [Dani85]. The peak at 0° indicates that the method works well in determine the reaction plane. The flat distribution of Mount Carlo events shows that there are no systematic problem with the technique.

Self Correlation:

There is a self correlation when using vector $\mathbf{Q}$ to determine the reaction plane. Suppose there is an isotropic emitting source with a Boltzmann distribution. The total number of particles in the source is infinite. We take m particles each time as an event to study the flow of the source by using $\mathbf{Q}$ to determine the direction of the flow. If m is large enough, the azimuthal angular distribution of all particles from all 'events with respect to the determined flow direction would be flat, since the source is isotropic. But if m is small the autocorrelation effects can be large. This effect is caused by the involvement of the particle itself in determination of $\mathbf{Q}$. If m is large enough, the self correlation can be ignored. In heavy ion reaction, the number of particle in an event is small (less than 10^2) and the self correlation has to be corrected. The way to correct the self correlation is by simply taking the particle of interest (POI) out of the determination of the reaction plane when the relation between the POI and the reaction plane is studied. For example to study the projection of a particle's momentum to the reaction plane, $\mathbf{p}_l \cdot \mathbf{Q}$, the $\mathbf{Q}$ vector has to be calculated by not involving particle l

$$\mathbf{Q}_l = \sum_{n \neq l}^{M} \omega_n \mathbf{p}_n^t, \tag{3.3}$$

Notice that the sum does not involve lth particle. The method has been successfully used in the high energy heavy ion reactions. At intermediate energies, the multiplicities are lower and the fluctuations are larger. To improve the flow studies in this energy range, a better method to suppress the fluctuations and reduce the error of determining the reaction plane was needed. That is the motivation for the azimuthal correlation method [Wils92].

3.2.2 Azimuthal Correlation Method

Determination of the Plane:

The azimuthal correlation method is done on the transverse momentum plane, i.e. $p_x - p_y$ plane. A straight line is drawn such that the sum of the distances from each particle to the line is minimized. Therefore the total deviation, D^2, is a function of the slope of the reaction plane in $p_x - p_y$ plane: [Wils92]

$$D^2 = \sum_{n=1}^{m}[d_n^2] = \sum_{n=1}^{m}\left((p_n^x)^2 + (p_n^y)^2 - \frac{p_n^x + p_n^y a)^2}{1+a^2}.\right) \tag{3.4}$$

Minimizing D^2 with respect to a gives:

$$a = \frac{Y_2 - X_2 \pm \sqrt{(X_2 - Y_2)^2 + 4(XY)^2}}{2XY}$$

$$X_2 = \sum_{n=1}^{M}(p_n^x)^2,$$

$$Y_2 = \sum_{n=1}^{M}(p_n^y)^2,$$

$$XY = \sum_{n=1}^{M}(p_n^x p_n^y).$$

The method is illustrated by Figure 3.2 (the figure is from reference [Wils92]).

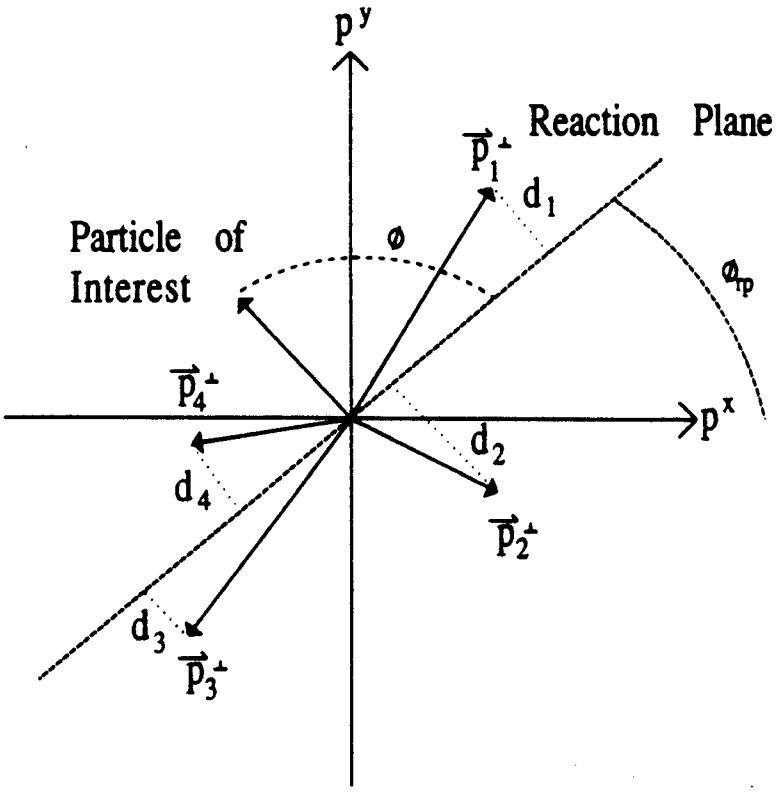

Figure 3.2: The quantities used in finding the reaction plane for an event projected on the $p^x - p^y$ plane. The angle of a POI with respect to the forward flow side of the reaction plane is labeled ϕ (from reference [Wils92]).

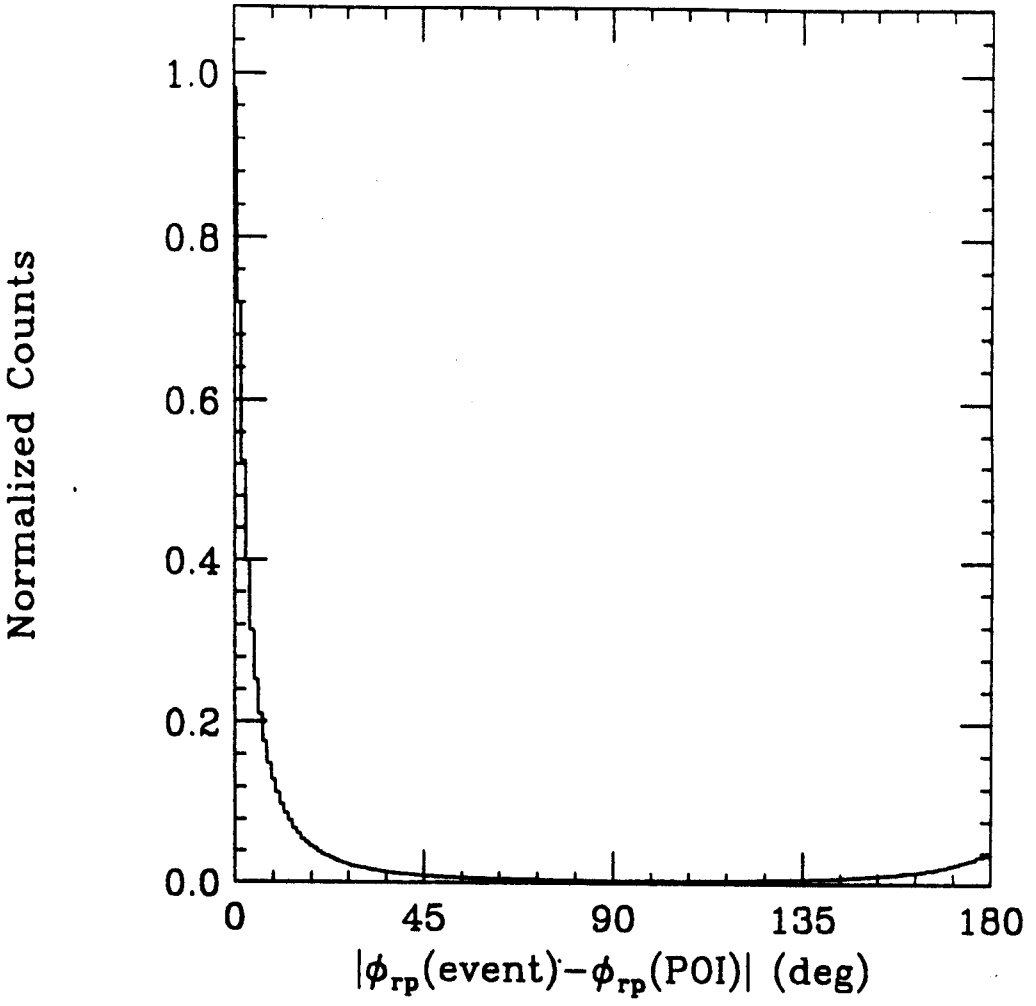

Figure 3.3: The azimuthal distribution of difference between reaction planes found for the entire events and reaction planes found leaving out POI (from reference [Wils92]).

This method does not give the projectile side or target side of the reaction plane. Therefore the transverse momentum method is used to calculate the **Q** vector to provide the required direction.

Self Correlation Correction:

As in the transverse momentum method, self correlation has to be removed. Figure 3.3 shows the difference of azimuthal angle distribution with respect to the reaction plane determined by all the particles (no correction of self correlation) and by removing the POI. First determine the flow direction by all the particles we get $\phi_{rp}(event)$ then remove POI we get $\phi_{rp}(POI)$, the distribution of $|\phi_{rp}(event) - \phi_{rp}(POI)|$ is plotted. One can see a peak around zero degrees.

3.2.3 Comparison of the Two Methods

To compare the two methods, simulation events are generated with known reaction plane. Then transverse momentum and azimuthal correlation methods are used to determine the reaction plane. The difference of determined reaction plane by the two methods from the true simulation reaction plane is plotted in Figure 3.4 (the figure is from reference [Wils92]). The azimuthal correlation method shows a smaller width than the transverse momentum method. This indicates a better reaction plane determination by azimuthal correlation method.

3.3 Impact Parameter Determination

A simple way of estimating the impact parameter of a nucleus-nucleus collision is to measure the charged particle multiplicity [Gust84]. This method suffers from the drawback that the number of observed particles may fluctuate widely at any given impact parameter depending on the decay mechanism. The decay process itself is a

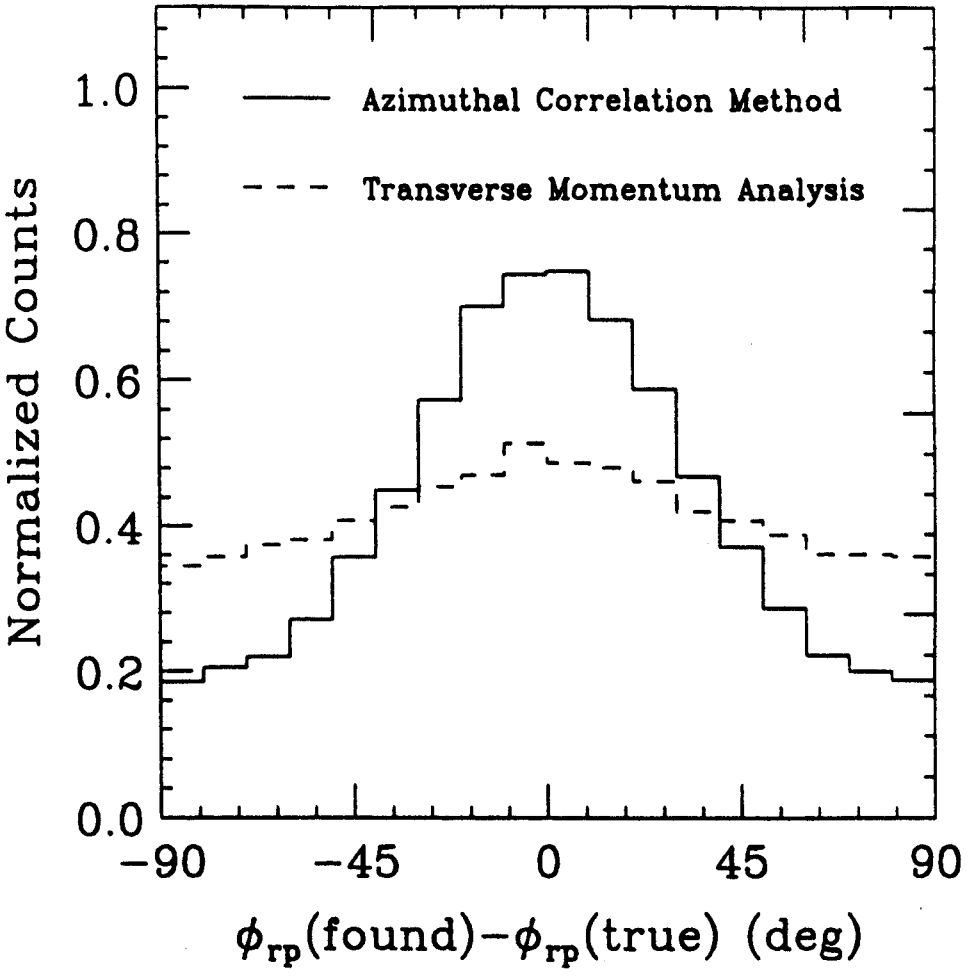

Figure 3.4: The distribution of differences between the found and true reaction planes for simulated events (from reference [Wils92]).

physical phenomena that is being studied in order to understand the dynamics of the reactions. The Plastic Ball group developed a method for determining the impact parameter based on the participant proton method [Gutb89a]. They showed that the number of protons, bound or unbound, that were not associated with the projectile or target decay could be related to the impact parameter. J. Péter et al. showed that the average parallel velocity was related to the impact parameter [Péte90a, Péte90b]. Ogilvie et al. used FREESCO filtered through the acceptance of the MSU 4π Array to test various methods of determining the impact parameter [Ogil89b]. They found that the best method for studying intermediate energy nucleus-nucleus collisions with the 4π Array was mid-rapidity charge, Z_{mr}, defined as the sum of the charge lying between 25% of target rapidity to 75% of projectile rapidity in center of momentum frame.

In this section we will present a method for determining the impact parameter in nucleus-nucleus collisions that is model independent and contains only a few assumptions. We will compare the results of this method to previous methods for determining the impact parameter in events observed with the MSU 4π Array. This method is analytic and is suitable for event-by-event analysis. We will analyze the accuracy of the method by comparing the correlation of the determined impact parameter using various observables.

3.3.1 Analytical Formula

If it is assumed that a given global observable q (such as mid-rapidity charge, total transverse momentum, average parallel velocity, multiplicity, etc.) is a monotonic function of impact parameter b [Cava90], then we can write the following relation:

$$\frac{2\pi b db}{\pi b_{max}^2} = \pm f(q)dq, \tag{3.5}$$

where b_{max} is the maximum impact parameter of the reaction and $f(q)$ is the probability density function of q, that is, $f(q)dq$ is the probability of detecting a collision with q between q and $q + dq$. $f(q)$ is normalized to unity and the plus and minus signs reflect the fact that q increases/decreases as b increases. If we now integrate equation (1) from b to b_{max}:

$$\int_b^{b_{max}} \frac{2bdb}{b_{max}^2} = \pm \int_{q(b)}^{q(b_{max})} f(q')dq', \tag{3.6}$$

and let

$$F(q) = \pm \int_{q(b)}^{q(b_{max})} f(q')dq', \tag{3.7}$$

then:

$$b/b_{max} = \sqrt{1 - F(q)}. \tag{3.8}$$

Equation 3.8 constitutes our formula for calculating impact parameter from a chosen global observable. The procedure for utilizing this formula is self evident; one only needs to construct a probability density distribution function for a chosen global observable (from experimental data) and employ it in Equation 3.8.

To further the study, the following three global observables can be defined:
Total Transverse Momentum: P_t, sum of transverse momentum (with respect to the projectile direction) of each detected particle in an event, ie.

$$P_t = \sum_{i=1}^{m} |\mathbf{p}_i^t|$$

Mid-Rapidity Charge: Z_{mr}, defined as:

$$Z_{mr} = \sum_{i=1}^{N_c} \epsilon_i Z_i \tag{3.9}$$

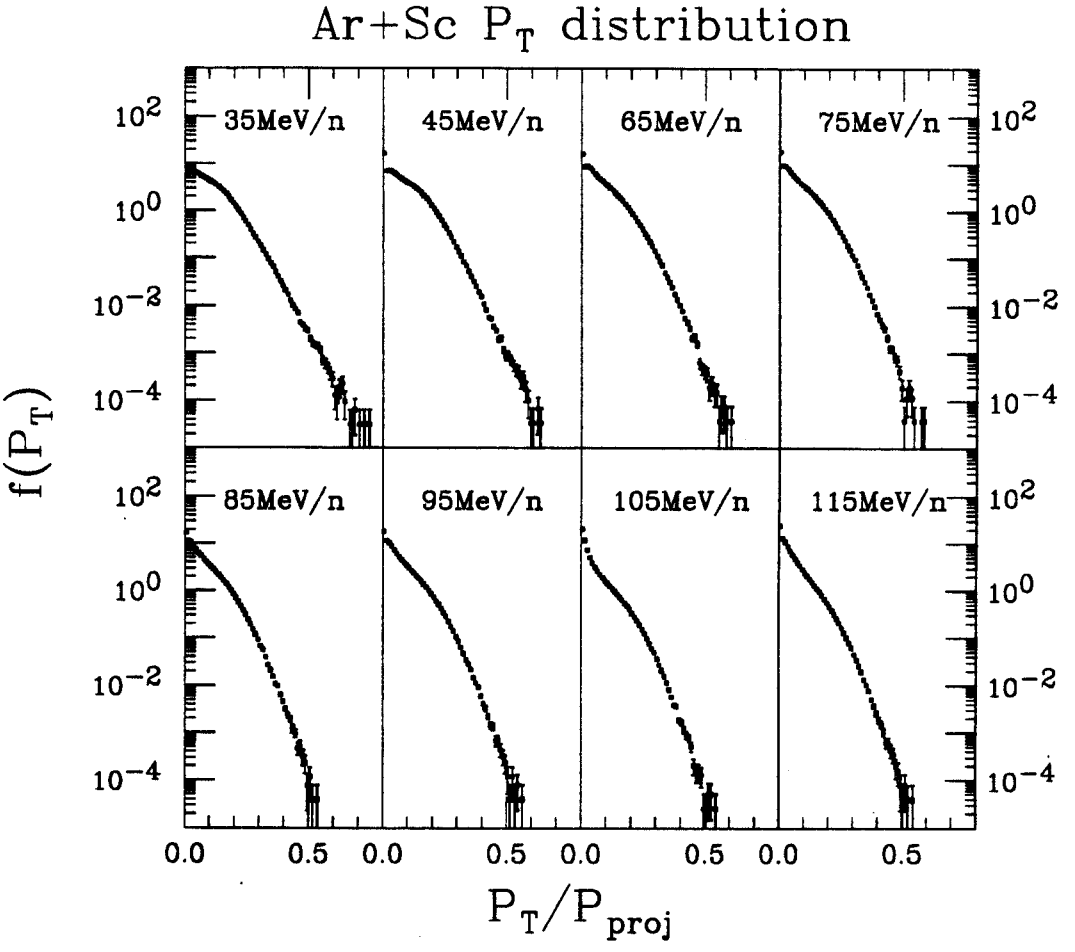

Figure 3.5: Total transverse momentum distribution for Ar + Sc from 35 to 115 MeV/nucleon.

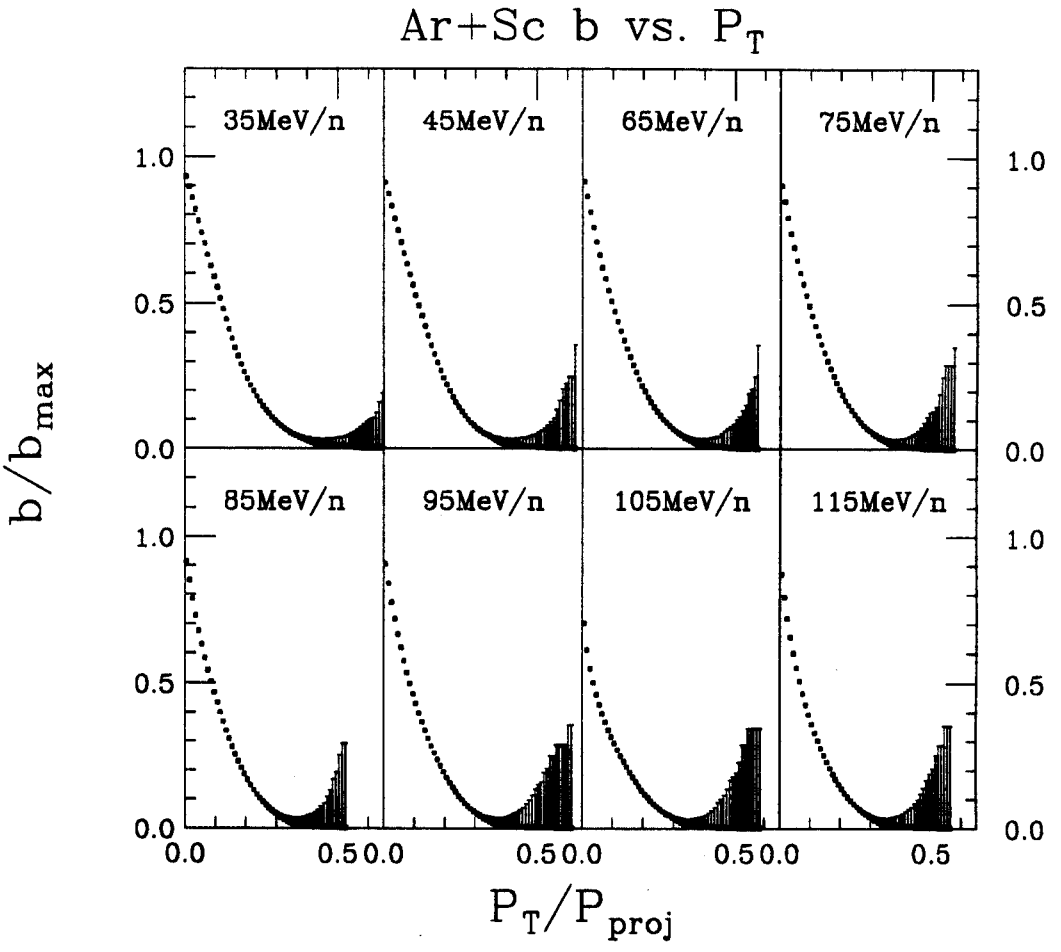

Figure 3.6: Impact parameter as a function of total transverse momentum for Ar + Sc from 35 to 115 MeV/nucleon.

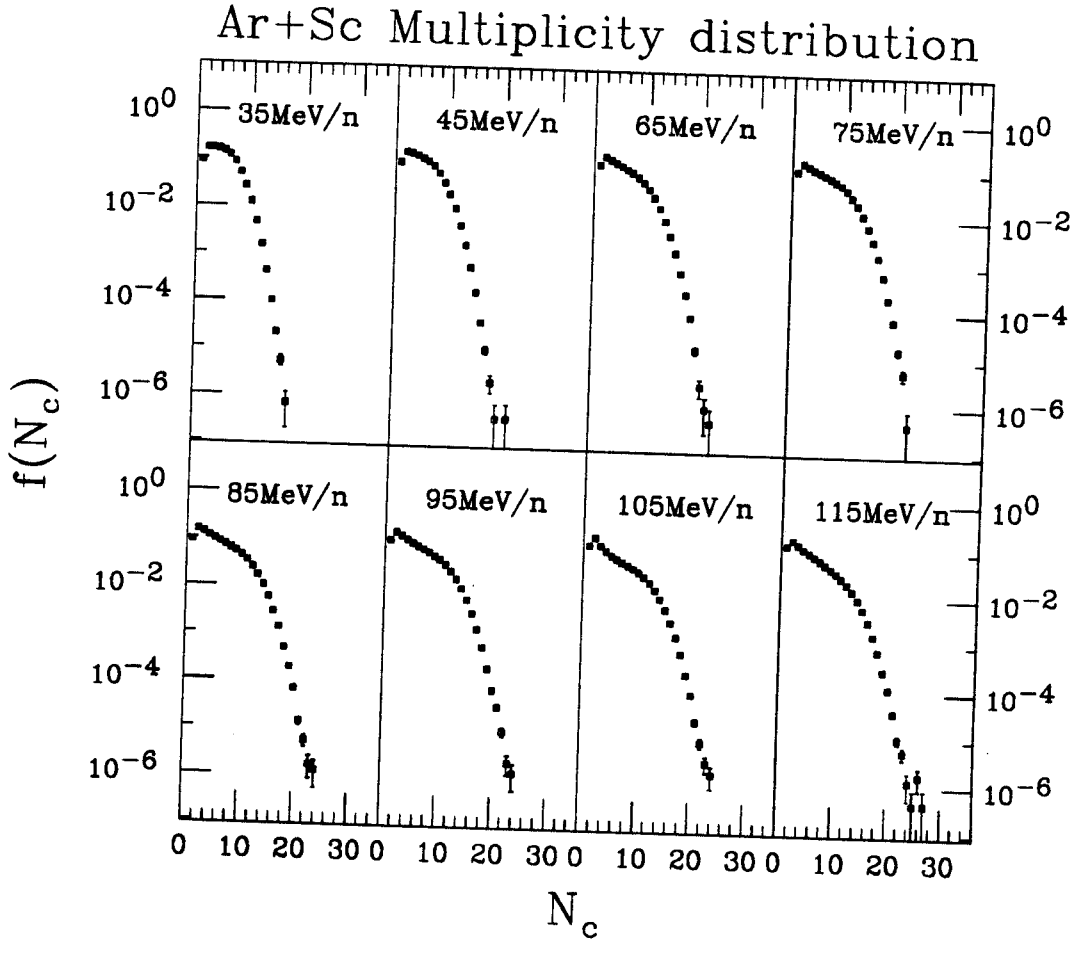

Figure 3.7: Charged particle multiplicity distribution for Ar + Sc from 35 to 115 MeV/nucleon.

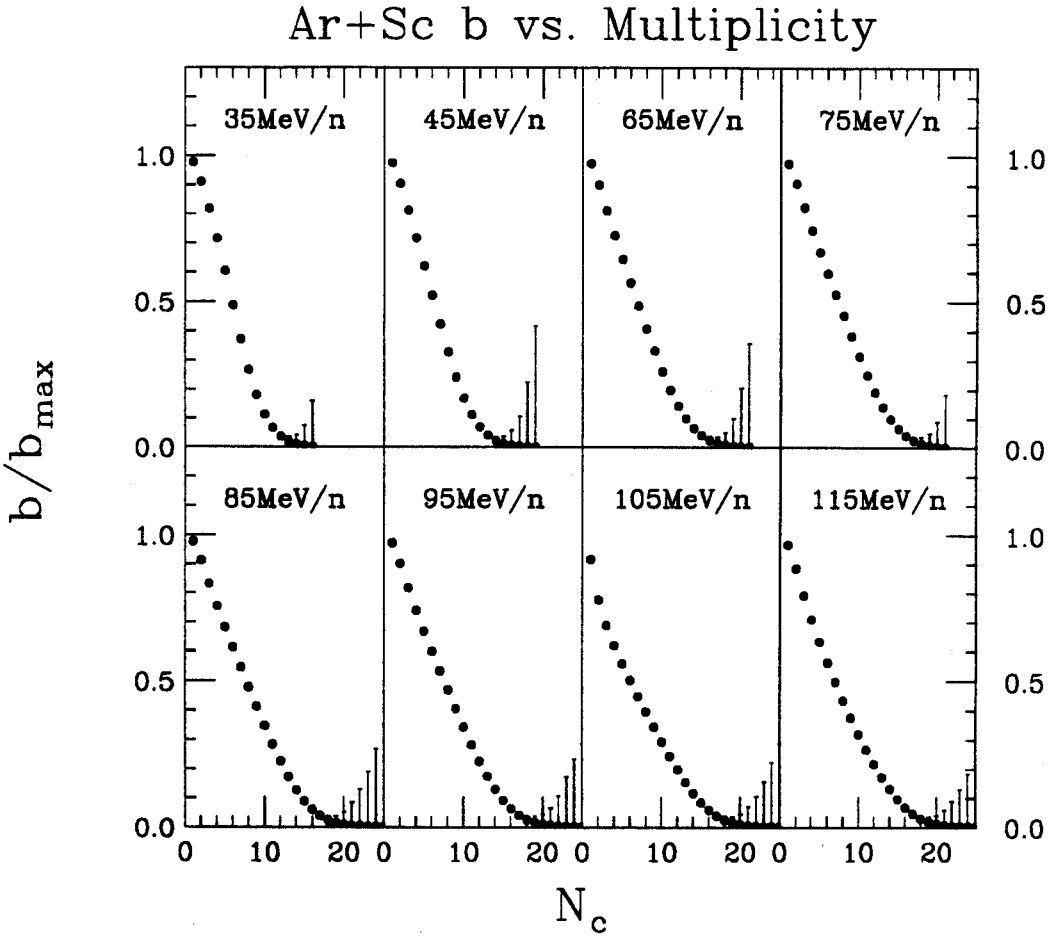

Figure 3.8: Impact parameter as a function of charged particle multiplicity for Ar + Sc from 35 to 115 MeV/nucleon.

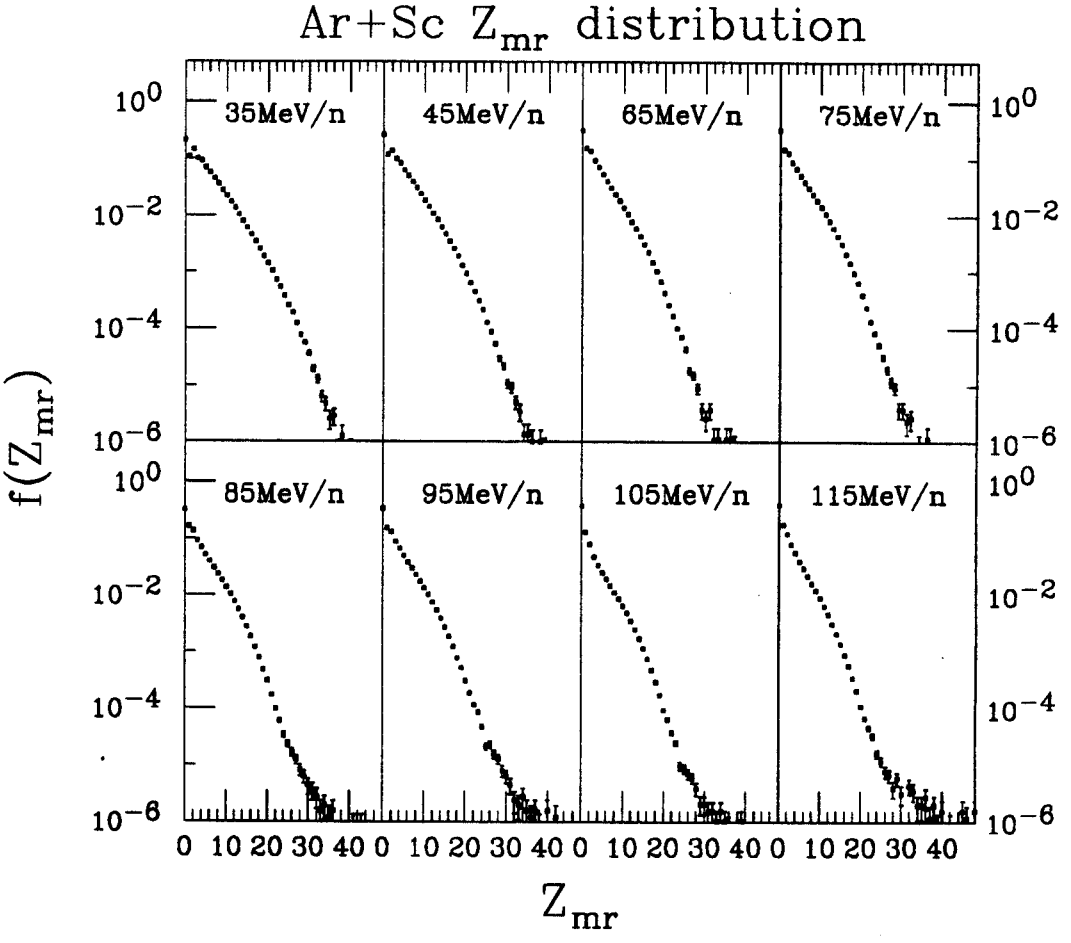

Figure 3.9: Mid-rapidity charge distribution for Ar + Sc from 35 to 115 MeV/nucleon.

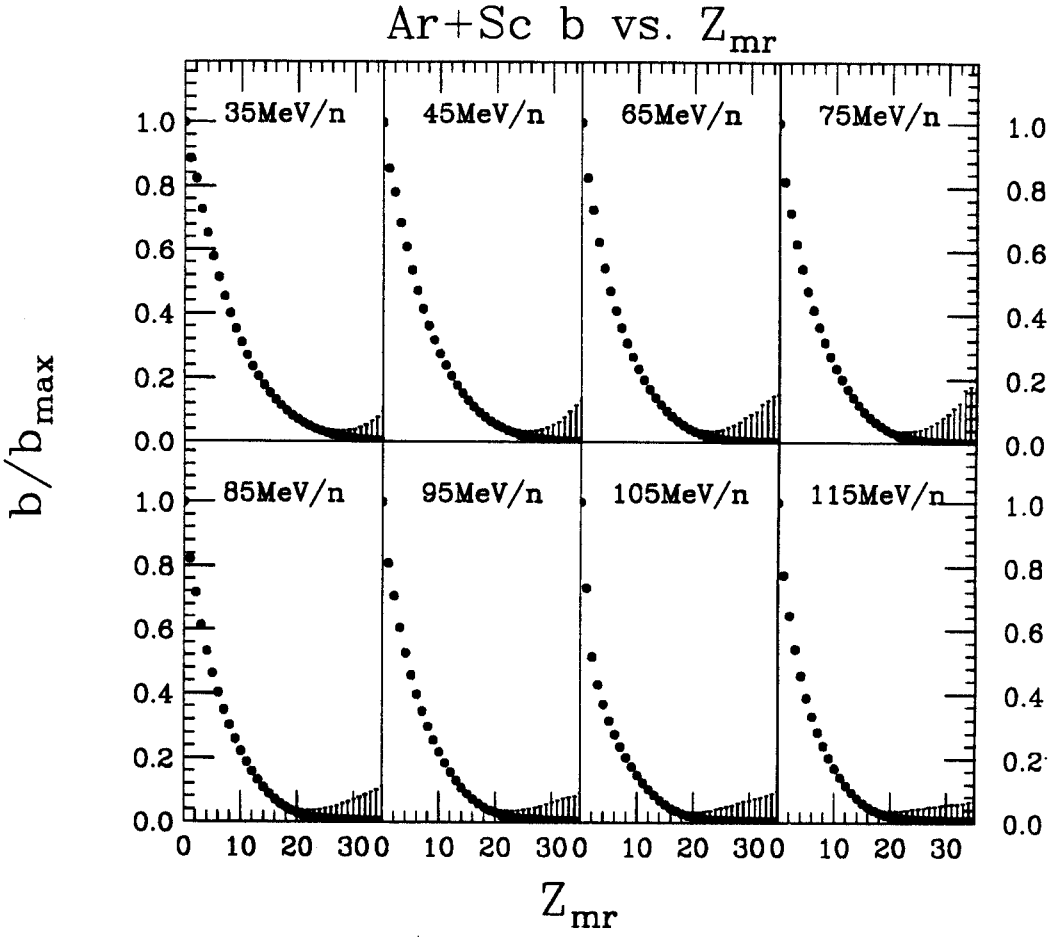

Figure 3.10: Impact parameter as a function of mid-rapidity charge for Ar + Sc from 35 to 115 MeV/nucleon.

$$\epsilon_i = \begin{cases} 1 & \text{if } 0.75y_t \leq y_i \leq 0.75y_p \\ 0 & \text{otherwise,} \end{cases} \tag{3.10}$$

where:

y_t → target rapidity
y_p → projectile rapidity
y_i → particle rapidity
Z_i → particle charge number

All the rapidities are in center of momentum frame. Z_{mr} is the sum of the detected charge which is between 75% of projectile and 75% of target rapidity for an event in center of momentum frame.

Charged Particle Multiplicity: N_c, defined as number of detected charged particle of an event.

For each of these global observables, the equation of 3.8 can be used to determine impact parameter. Figure 3.5 shows the total transverse momentum distributions for Ar + Sc at 35 to 115 meV/nucleon and Figure 3.6 shows the impact parameter (normalized to measured maximum impact parameter) as a function of total transverse momentum calculated from the total transverse momentum distributions by equation 3.8. The charged particle multiplicity and mid-rapidity charge also can be used to determine impact parameter by employing equation 3.8. Figure 3.7 shows the total charged particle multiplicity distribution and Figure 3.8 shows the relation between N_c and the impact parameter b. The mid-rapidity charge distribution is shown by Figure 3.9 and the relation between impact parameter b and mid-rapidity charge Z_{mr} is shown by Figure 3.10.

3.3.2 Comparisons to Earlier Work

The mid-rapidity charge global observable (Z_{mr}) has been extensively studied by our group [Ogil89b] as well as others [Péte90a, Tsan89]. These earlier studies exploited

simulation techniques to study the relationship between Z_{mr} and impact parameter. Here, we compare results extracted from our formula to some of these earlier results. In order to facilitate the comparison, we have adopted the event classifications (peripheral: $0 \leq Z_{mr} < 3$, mid-peripheral: $3 \leq Z_{mr} < 7$, mid-central: $7 \leq Z_{mr} < 12$), and central: $12 \leq Z_{mr}$) previously employed in reference [Ogil89b].

For each of the above Z_{mr} gates, impact parameter distributions were determined from $F(P_t)$ distributions using Equation 3.8. Figure 3.11 shows these impact parameter distributions along with the ungated (total) distribution for Ar + V at 45 MeV/nucleon. Figure 3.11 shows a striking resemblance to Figure 7 of reference [Ogil89b] indicating that both Z_{mr} and P_t provide a good measure for impact parameter. It is worth noting that the gated distributions in Figure 3.11 have all been normalized to the total distribution (those of reference [Ogil89b] were individually normalized). The total impact parameter distribution also shows a linear dependence on b in accordance with expectation.

3.3.3 Error Analysis

In our derivation of Equation 3.8 we did not take into account possible fluctuations in the values of a chosen global observable. In reality, for a certain impact parameter, the associated global observable is more likely a distribution characterized by an expectation value and a width. As a consequence, it is more realistic to assume that it is the expectation value of a given global variable which is a monotonic function of impact parameter (ie. $\langle q \rangle = \langle q(b) \rangle$). Then the determined impact parameter will be a distribution around a real impact parameter b_{real} with a certain width. In what follows, we attempt to estimate the width of this distribution using a few simple assumptions.

Let us assume that there are three measurable global observables $q_i (i = 1, 2, 3)$

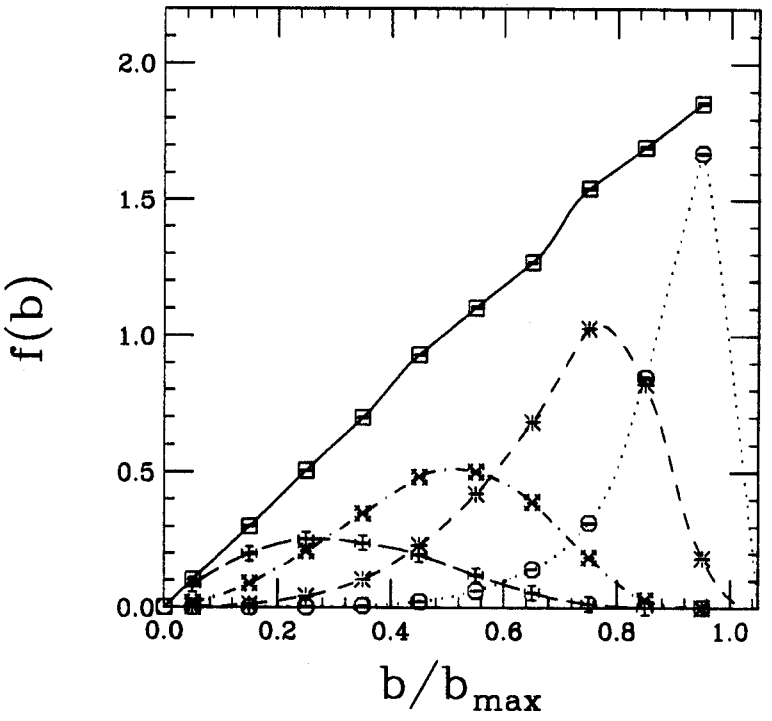

Figure 3.11: The impact parameter (determined by total transverse momentum P_t) distribution gated by mid-rapidity charge for central (daashes), mid-central (dot-dash), mid-peripheral (dash) and peripheral (dots) events. The total distribution (solid) shows a linear dependence on impact parameter b. The total distribution is normalized to unity.

which are monotonic functions of impact parameter. Then, $b_{q_i} = b(q_i)$ is the impact parameter derived from global observable q_i (i=1,2,3). We now construct three new random variables:

$$X = (b_{q_1} - b_{real}),$$

$$Y = (b_{q_2} - b_{real}),$$

$$Z = (b_{q_3} - b_{real}). \tag{3.11}$$

If the errors associated with these new variables are purely statistical, i.e. random, then X, Y, Z are normally distributed random variables centered at 0 with a variance of $\sigma^2_{q_1}$, $\sigma^2_{q_2}$ and $\sigma^2_{q_3}$ respectively. The $\sigma^2_{q_i}(i = 1,2,3)$ can not be directly measured or calculated since b_{real} is not known. However, if X, Y and Z are assumed to be independent of each other, then we can construct a secondary set of random variables:

$$R_1 = (X - Y) = (b_{q_1} - b_{q_2}),$$

$$R_2 = (Y - Z) = (b_{q_2} - b_{q_3}),$$

$$R_3 = (Z - X) = (b_{q_3} - b_{q_1}), \tag{3.12}$$

which are normally distributed with variances of σ^2_1, σ^2_2, and σ^2_3 respectively. $\sigma^2_i(i = 1,2,3)$ can be measured by calculating the impact parameter of the same event using all three global observables.

Using the central limit theorem, the variances of $b_{q_i}(i = 1,2,3)$ can be estimated as follows:

$$\sigma^2_1 = \sigma^2_{q_1} + \sigma^2_{q_2},$$

$$\sigma^2_2 = \sigma^2_{q_2} + \sigma^2_{q_3},$$

$$\sigma^2_3 = \sigma^2_{q_3} + \sigma^2_{q_1}. \tag{3.13}$$

The solution to these three equations yield:

$$\sigma_{q_1} = \sqrt{(\sigma_1^2 - \sigma_2^2 + \sigma_3^2)/2},$$

$$\sigma_{q_2} = \sqrt{(\sigma_1^2 + \sigma_2^2 - \sigma_3^2)/2},$$

$$\sigma_{q_3} = \sqrt{(-\sigma_1^2 + \sigma_2^2 + \sigma_3^2)/2}, \tag{3.14}$$

which can be used for an error estimate.

Figure 3.12 shows the distributions of $R_1 = (b_{P_t} - b_{Z_{mr}})$, $R_2 = (b_{Z_{mr}} - b_{N_c})$ and $R_3 = (b_{N_c} - b_{P_t})$ for the Ar + V system at 45 MeV/nucleon. The lines are fits which assume a normal distribution with $\sigma_1 = 0.130 b_{max}$, $\sigma_2 = 0.138 b_{max}$ and $\sigma_3 = 0.115 b_{max}$ respectively. Here b_{P_t} is the impact parameter determined by total transverse momentum, $b_{Z_{mr}}$ is the impact parameter determined by mid-rapidity charge and b_{N_c} is the impact parameter determined by multiplicity. The errors of the distributions in Figure 3.12 indicate that determination of impact parameter by using different global observables using Equation 3.7 are within 15% of maximum impact parameter b_{max}. If we employ Equation 3.13, we obtain $\sigma_{P_t} = 0.077 b_{max}$, $\sigma_{Z_{mr}} = 0.107 b_{max}$, and $\sigma_{N_c} = 0.088 b_{max}$. These results show that for the reaction of Ar + V at 45 Mev/nucleon if the random variables X, Y, Z are independent and errors of their distributions are statistical then using P_t, Z_{mr} and N_c to determine impact parameter gives a result accurate to 7.7%, 10.7% and 8.8% of b_{max} respectively.

It should be pointed out that if X, Y, Z are not independent, then the above analysis would be invalid. Nonetheless, the error analysis still shows the lower limits of the error associated with an estimate of the impact parameter from the three chosen global observables.

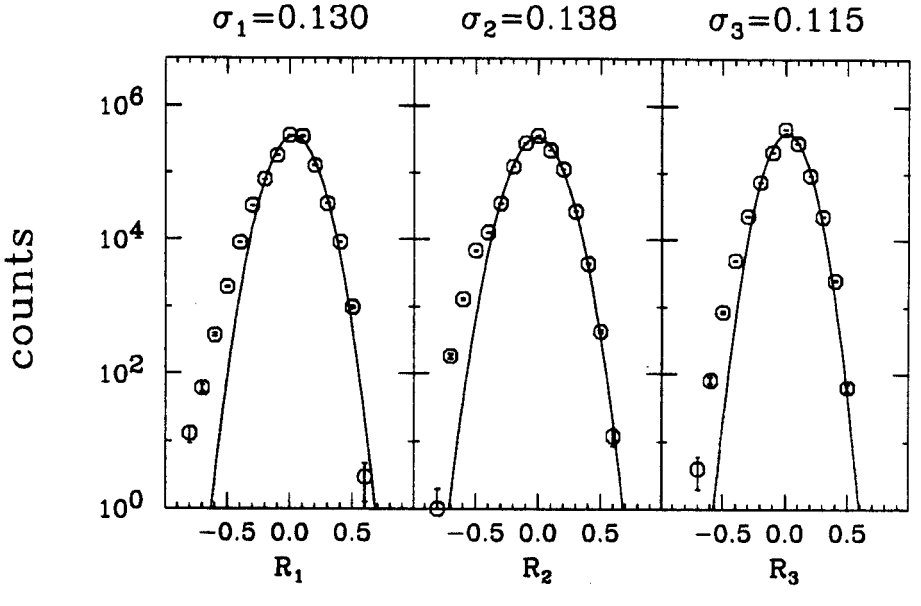

Figure 3.12: Distribution of R_1, R_2 and R_3 fitted with normal distributions which have $\sigma_1 = 0.130 b_{max}$, $\sigma_2 = 0.138 b_{max}$ and $\sigma_3 = 0.115 b_{max}$, respectively.

3.3.4 Combined Global Observable

When the above method is employed in cutting experimental data, one has to be aware of the gating bias introduced by the impact parameter determination with a certain global observable. For example, if one gates on events using charged particle multiplicity, then the multiplicity studies, such as light particle multiplicity and intermediate mass fragment multiplicity will be biased because of the charged particle multiplicity is directly correlated with all the other particle multiplicities. Also, if charged particle multiplicity is used to determine impact parameter, then the Z (charge number) distribution would be biased due to the charge conservation. If the total transverse momentum is used then the kinetic energy spectra in forward angle will be suppressed since particle in forward direction have little transverse momentum. In most cases, one would use the global observable which is not directly correlated with the observables under study.

To show the gating bias by single global observable, contour plots of normalized total transverse momentum of an event, $P_T = \frac{2}{\pi}\sum_{i=1}^{N_c} |p_t^i|$ vs. total parallel momentum of an event, $P_P = \sum_{i=1}^{N_c} |p_p^i|$. Figure 3.13 shows the contour plot of central collision gated by total transverse momentum with $0 \leq b \leq 0.25 b_{max}$. The isotropy ratio defined as [Strö83].

$$R = \frac{2\sum_{i=1}^{N_c} |\mathbf{p}_i^t|}{\pi \sum_{i=1}^{N_c} |\mathbf{p}_i^p|} = P_T/P_P, \tag{3.15}$$

where $\mathbf{p}_i^t$ and $\mathbf{p}_i^p$ are the transverse momentum and parallel momentum of ith particle in an event, can be used to estimate the goodness of the centrality cut for central collisions. The sum is over all charged particles of an event. The ratio R is used to measure the degree of isotropy in phase space. For isotropic events $R = 1$. We calculated $\langle R \rangle$ averaged over all events. Although the central collisions gated by total transverse momentum show that averaged $\langle R \rangle$ ratios are not significantly different

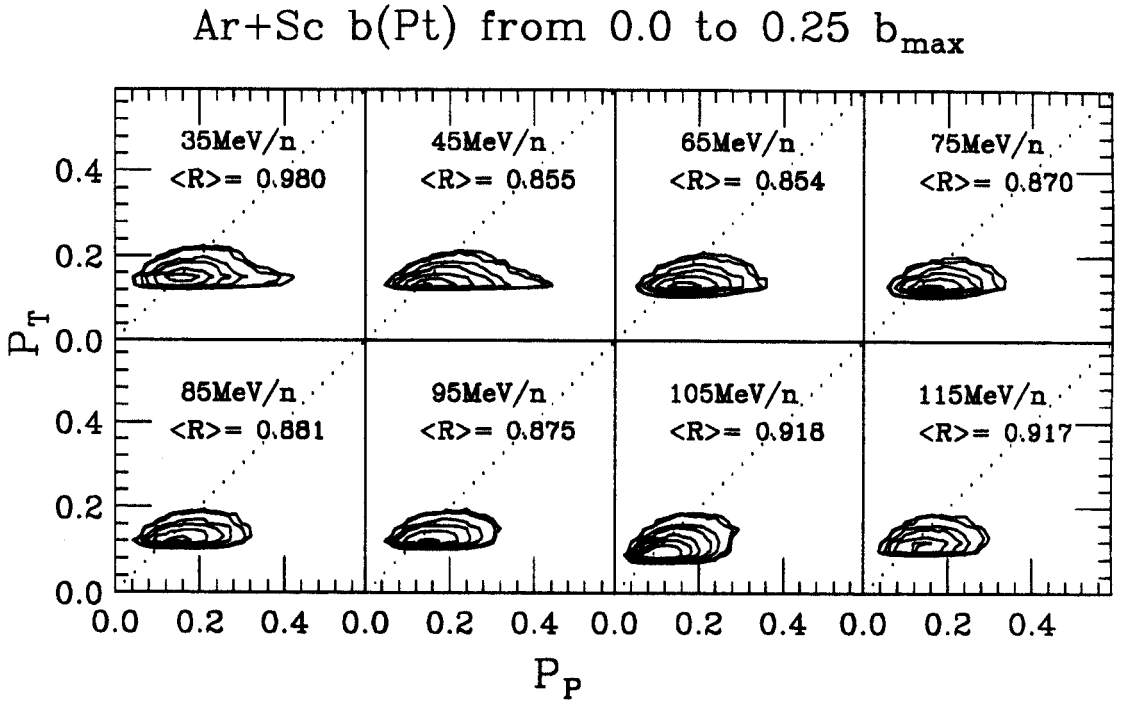

Figure 3.13: Contour plot of P_T vs. P_P of P_t gated central collisions with $0 \leq b \leq 0.25$. From top left to bottom right are 35, 45, 65, 75, 85, 95, 105, 115 MeV/nucleon Ar + Sc.

from central collisions gated by mid-rapidity charge (see Figure 3.18), the P_T vs. P_P contour plots show that the cut elongated the P_T -P_P shape. Gating events with a global observable which is not directly correlated with momentum will provide a satisfactory result. For example, one can use mid-rapidity charge to determine impact parameter to study momentum distribution. Figure 3.14 shows the contour plots of P_T vs P_P of central events ($0 \leq b \leq 0.25 b_{max}$) gated by mid-rapidity charge, Z_{mr}. The contour plots are smooth and the centers are close to the diagonal dotted line corresponding to $R = 1$.

If we choose different global observables to do different studies, then we cannot cross reference the studies. For an event, there is one and only one impact parameter. In order to determine the impact parameter for different studies, a three dimensional cut is necessary. A gate on the three dimensional space composed by Z_{mr}, N_c and P_T can be constructed to serve this purpose. For example, we use a combined global observable defined as:

$$g = \sqrt[3]{(N_c/N_{max})(Z_{mr}/Z_{tot})(P_T/P_{proj})}, \tag{3.16}$$

where N_{max} is the maximum charged particle multiplicity (39 for Ar + Sc), Z_{tot} is the total charge of the system and P_{proj} is the projectile momentum in the laboratory frame. A constant of g indicates a three dimensional parabolic surface. If we use g as a global observable and use Equation 3.7 and 3.8 to determine impact parameter, we get a common impact parameter measurement.

By using g to determine the impact parameter, we also can reduce detector bias. For example, high N_c event in which most particles are detected by forward array detectors will have low Zmr and low P_t, therefore is not a central collision.

Figure 3.15 shows the g distribution for Ar + Sc from 35 to 115 MeV/nucleon and Figure 3.16 shows the impact parameter as a function of g.

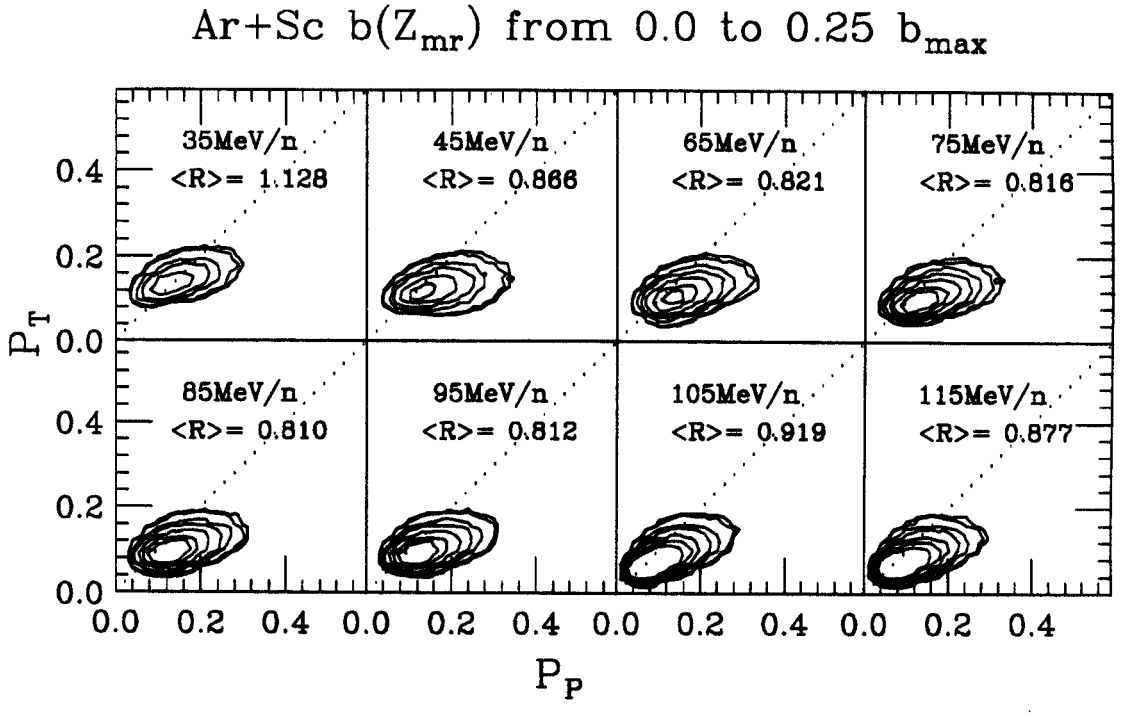

Figure 3.14: Contour plot of P_T vs. P_P of Z_{mr} gated central collisions with $0 \leq b \leq 0.25$. From top left to bottom right are 35, 45, 65, 75, 85, 95, 105, 115 MeV/nucleon Ar + Sc.

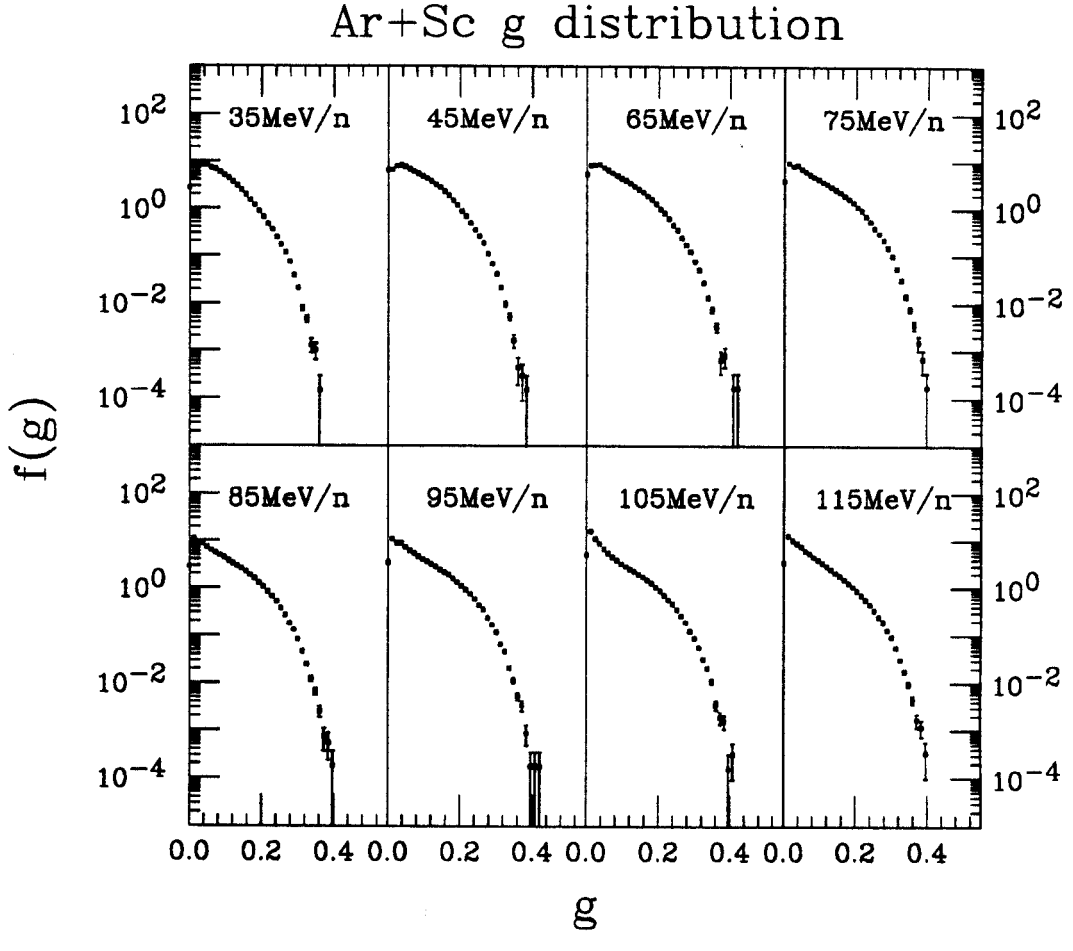

Figure 3.15: g distribution for Ar + Sc from 35 to 115 MeV/nucleon.

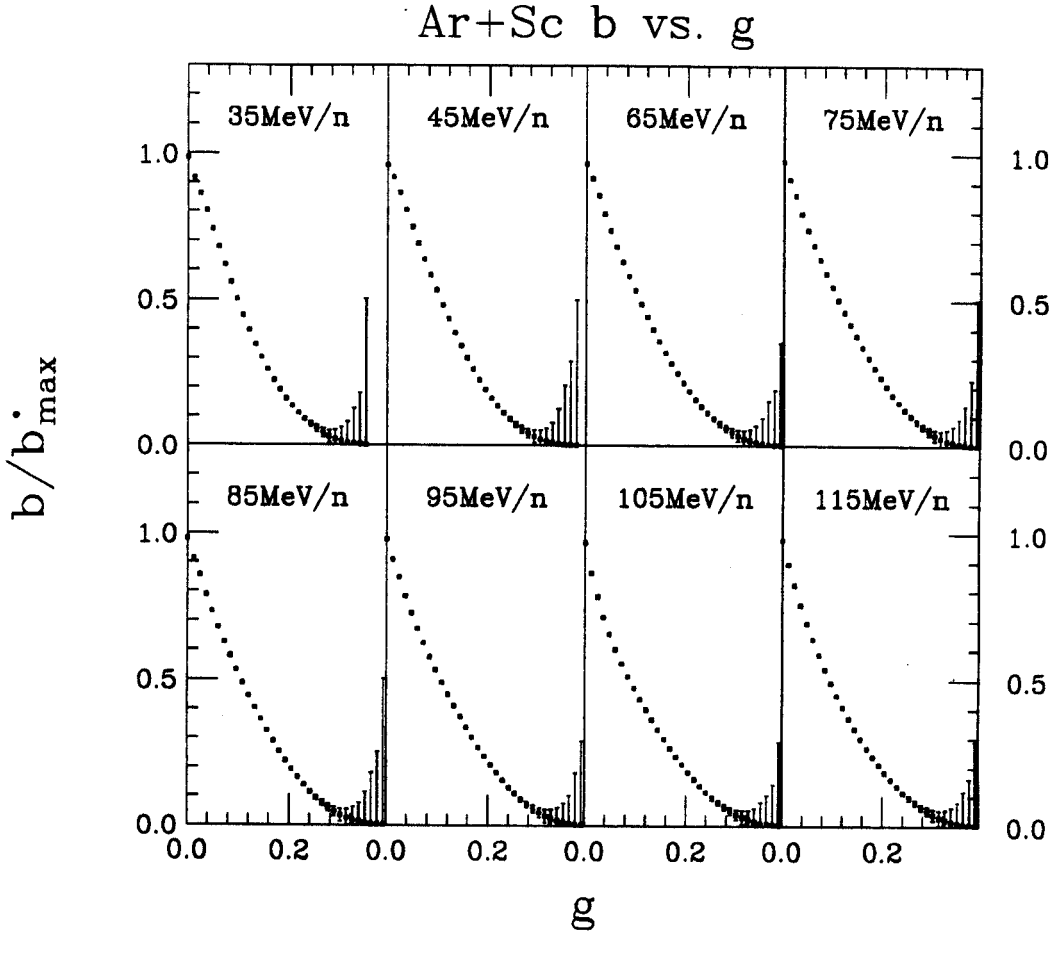

Figure 3.16: Impact parameter as a function of g for Ar + Sc from 35 to 115 MeV/nucleon.

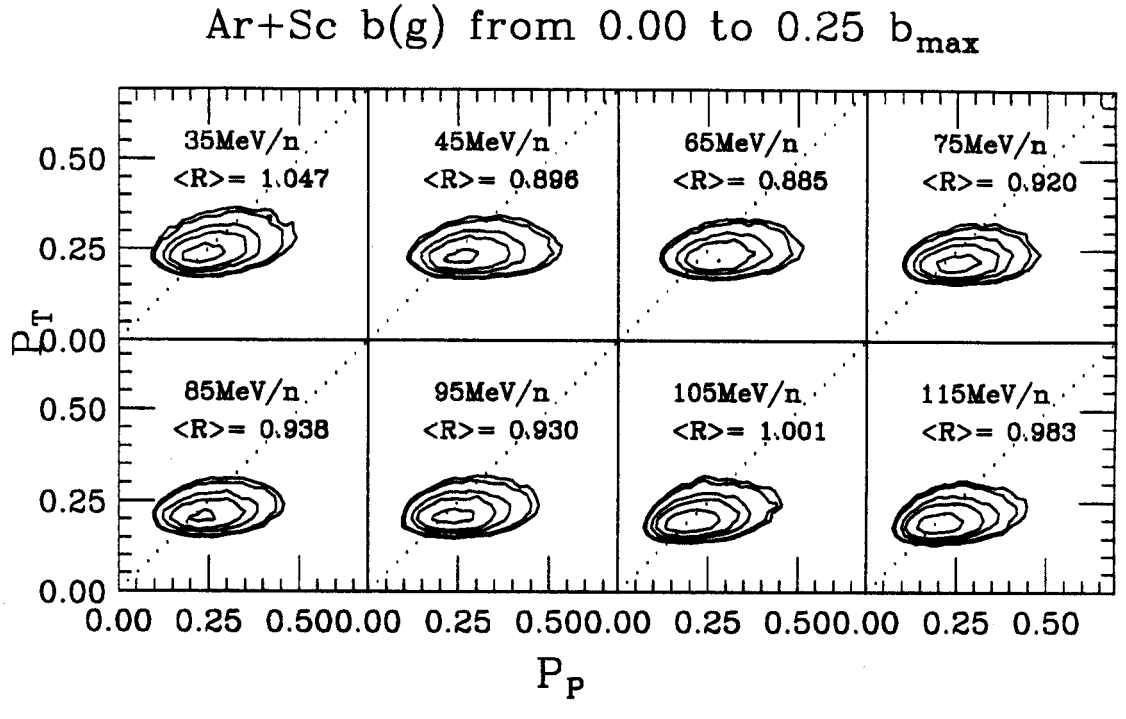

Figure 3.17: Contour plot of P_T vs. P_P of g gated central collisions with $0 \leq b \leq 0.25$. From top left to bottom right are 35, 45, 65, 75, 85, 95, 105, 115 MeV/nucleon Ar + Sc.

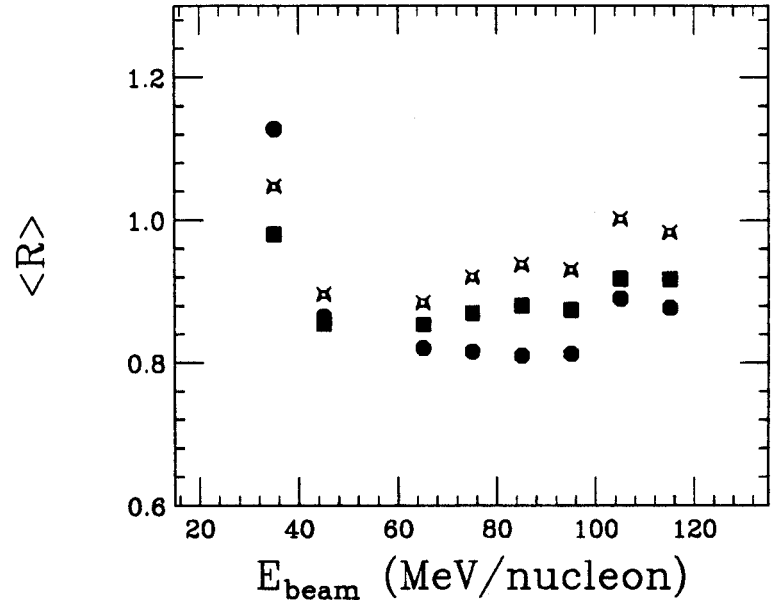

Figure 3.18: The average isotropy ratio $\langle R \rangle$ of central collisions gated by P_t (solid squares), Z_{mr} (solid circles) and g (crosses) for different beam energies.

Figure 3.17 shows the P_T vs. P_P contour plot for central collisions gated by g with $0 \leq b \leq 0.25$. Smooth contours shows the centrality cuts are smoother than those done with Z_{mr} and P_t gated central collisions. The averaged isotropy ratio vs. beam energies for the three gates, P_t (solid squares), Zmr (solid circles) and g (crosses) are shown in Figure 3.18. One can see that the central events gated by g are closer to 1.

3.4 Summary

The reason for the exclusive measurements is to estimate initial conditions by global observables. Therefore, the determination of initial conditions is a major effort for a 4π measurement prior to any study of physics. We introduced two methods of determining the reaction plane, i.e. transverse momentum method and azimuthal correlation method. The comparison of the two methods shows that the azimuthal correlation method gives a better reaction plane determination. In this thesis, the azimuthal correlation method is used. The impact parameter determination has been associated with a simple assumption that a certain global observable is a monotonic function of impact parameter. Then an analytical formula is derived which can be used to measure impact parameter through certain global observable. To obtain a common gate for all of our analysis, a three dimensional gate has been introduced. We constructed a combined global observable, g, which is used to determine the impact parameter.

Chapter 4

Multi-fragmentation and Liquid-gas Phase Transition

4.1 Introduction

Much activities has occurred in recent years in intermediate energy heavy ion reactions because of many transitional phenomena in this energy region. It is believed that the reaction goes through a transition from sequential decay to multi-fragmentation [Cebr90b, Frie89, Lópe89]. Several groups have demonstrated that multi-fragmentation may exist. [Boug88, Yenn90, Bowm91, Blum91, Yenn91, Ogil91, Hube91, Bowm92, Kim92, Sang92, Hage92, Grab92, Ogil93, Peas92]. At low beam energy, just above coulomb barrier, the projectile fuses with target to form a compound system. The excited compound system then evaporates light particles or goes through binary fission. Experimental evidence shows at low beam energy binary sequential decay model gives a better description of the reaction [Cebr90b]. At high beam energy, the excitation energy is high enough to cause the system to disintegrate in a very short time scale and undergo simultaneous multi-fragmentation. Multi-fragmentation is defined as the simultaneous emission of three or more fragments with $Z \geq 3$.

Theories of hadronic matter predict qualitative phase structure in terms of

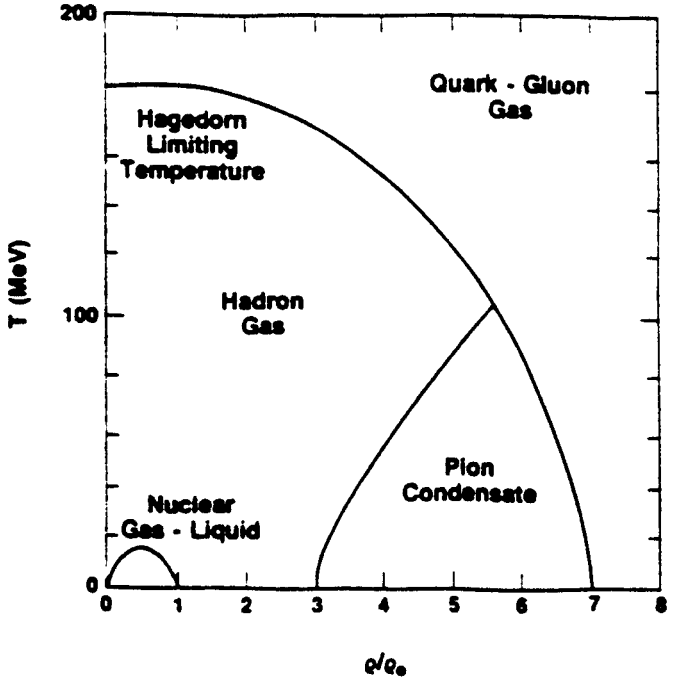

Figure 4.1: Theoretically expected phase diagram for the strong interactions. (from reference [Good84]).

temperature and nucleon density shown in Figure 4.1 [Good84]. At high temperature or high density, there is a first order phase transition from hadron gas to quark-gluon gas and at low temperature and high density there is pion condensation, which is a second order phase transition. While at low temperature and low density, the first order liquid-gas phase transition would terminate at a critical point which signatures a second order phase transition. The liquid-gas phase transition is in the region of intermediate energy heavy ion reaction.

The predicted liquid-gas phase transition in the intermediate energy region has been studied by numerous researchers. Nuclear matter exists in a liquid-like state in its ground state. When nuclear matter is heated to excitations high compared to its binding energy it behaves like a classical gas.

Due to the long range attractive interaction and short range repulsive nucleon-

nucleon interaction in nuclear reaction, a liquid-gas phase transition was predicted by comparing the nuclear equation of state (EOS) with the Van der Waals equation of state [Boal86, Good84, Jaqa84]. According to nuclear EOS, constructed from two body potential, when the system go through a isotherm expansion at low excitation energy, it goes through a first order liquid-gas phase transition. The liquid-gas phase transition terminates at a second order phase transition with a critical point. [Curt83, Good84, Jaqa84, Pana84, Kapu84, Bond85, Boal86, Cser86, Peth87]. The predicted critical temperature include from 15.3 MeV [Boal86], 17.3 [Glen86] to 21.5 MeV [Good84] for infinite nuclear matter and about 12 MeV in finite nuclei [Chit83, Schu82].

The signature of such phase transition is a power law like cluster distribution $\sigma(A) = \alpha A^{-\lambda}$ (where A is the size of a cluster, α and λ are constants) in the vicinity of the critical point predicted by both droplet model [Fish67, Pana84, Pori89] and percolation model [Baue88, Stau79]. At the critical point, the parameter λ reaches a minimum, τ, the critical exponent.

In terms of dynamics, nucleus-nucleus collisions have a transverse collective flow in phase space, which dominated by attractive mean field at low beam energies. At high beam energies, the flow is dominated by repulsive nucleon-nucleon collisions. The balance energy at which the attractive mean field and repulsive nucleon-nucleon collision cancel each other, may provide an experimental gauge to determine parameters of the EOS of nuclear matter through dynamic models such as BUU (Boltzmann-Uehling-Uhlenbeck) [Bert88]. All of the transitional information may be used to map the EOS of nuclear matter if the finite size effects are considered. The nuclear EOS can not be directly observed in terms of macroscopic quantities. Therefore, these transitional phenomena may play the definitive role for the nuclear EOS, which may explain some astrophysical calculations and observations of supernova and neutron

stars [Baro85, Baro87, Sumi92].

In this chapter, first we introduce the basic concept of a liquid-gas phase transition for infinite nuclear matter by looking at the EOS. Then we discuss both Fisher's droplet model predictions and percolation theory predictions. The existing problems will be discussed. The experimental results and new percolation calculations are presented, which give a general picture of a liquid-gas phase transition in finite nuclear matter.

4.1.1 Equation Of State (EOS) of Nuclear Matter

A nuclear equation of state derived from a Skyrme-type interaction shows a similarity with Van der Waals EOS [Good84, Boal86]. The EOS written in terms of pressure and nucleon number density is as follows:

$$P = -a_0\rho^2 + 2a_3\rho^3 + kT, \tag{4.1}$$

where P is the pressure and ρ is nucleon number density and T is the temperature, a_0, a_3 and k are constants which can be determined from ground state properties of nuclear matter.

The EOS looks like a Van der Waals EOS. It shows a region of instability for a first order liquid-gas phase transition which terminates at a critical point. Using ground state properties of nuclei including the binding energy of 8 MeV/nucleon and $\rho_0 = 0.15$ fm^{-3} one gets $a_0 = 293.33$ MeVfm^3 and $a_3 = 6666.66$ MeVfm^6, which corresponds to a compressibility $K = 224$ MeV [Good84]. Using these constants, we plot equation 4.1 in Figure 4.2. The critical point is determined by first and second order differentiation of the EOS in respect to ρ, i.e.

$$(\frac{\partial P}{\partial \rho})_T = 0,$$

$$(\frac{\partial^2 P}{\partial \rho^2})_T = 0, \tag{4.2}$$

which yield

$$\begin{aligned} \rho_c &= a_0/(6a_3) &&= 0.489\rho_0 \\ T_c &= a_0^2/(6a_3) &&= a_0\rho_c = 21.5MeV \\ P_c &= a_0^3/(108a_3) &&= \rho_c T_c/3 = 0.526MeV/fm^3. \end{aligned} \tag{4.3}$$

Below the critical point there is a liquid-gas co-existence region shown by the dashed line, which is obtained by Maxwell construction of equal area in a P-V (pressure vs. volume) plot. Above the critical point only the gas phase exists. We should note that the above EOS is for infinite nuclear matter although it used ground state nuclear properties which are measured using finite nuclear matter with nucleon numbers in the order of 10^2.

Another example of parameterizing the EOS of nuclear matter gives a very interesting result. It approximates the ground state energy as a parabolic function around the minimum energy [Kapu84]. In the vicinity of the minimum energy of the mean-field, the EOS can be written as:

$$P(\rho, T) = \frac{K\rho^2}{9\rho_0}(\frac{\rho}{\rho_0} - 1) + \frac{1}{6}c\rho^{1/3}T^2, \tag{4.4}$$

where K is the nuclear compressibility and c is a constant, which gives a critical temperature and density only in terms of ρ_0 and nuclear compressibility.

$$\begin{aligned} \rho_c &= \frac{5}{12}\rho_0 \\ T_c &= 0.326(K/m)^{1/2}\rho_0^{1/3}, \end{aligned} \tag{4.5}$$

where ρ_c and T_c are critical density and critical temperature, respectively. Using ground state density $\rho_0 = 0.15\ fm^{-3}$ and compressibility K=210 the critical temperature is 16.1 MeV and critical density is 0.417 ρ_0.

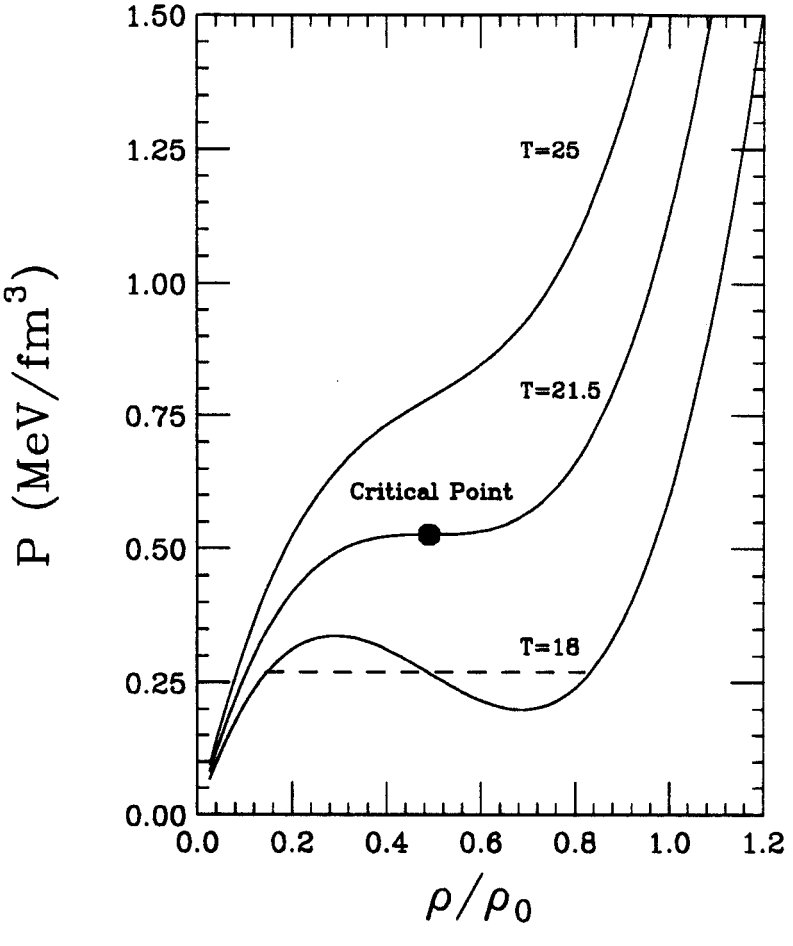

Figure 4.2: EOS of nuclear matter. The pressure vs. nuclear density at fixed temperature indicated on the plot.

If the critical temperature can be measured experimentally, it can be used as a calibration point for the nuclear EOS.

4.1.2 Fisher's Droplet Model

According to Fisher's droplet model [Fish67, Good84, Pana84], the size distribution of the droplets, or particle clusters, in the gaseous phase is:

$$\begin{aligned} P(A) &\sim A^{-\tau} X^{A^{2/3}} Y^{A} \\ X &= exp[-a_s(T)/T] \\ Y &= exp\{-[a_v(T) - \mu(T)]/T\}, \end{aligned} \tag{4.6}$$

where $a_s(T) = \alpha_s(T) - TS_s$ and $a_v(T) = \alpha_v(T) - TS_v$ are surface and volume free energy per particle respectively and $\mu(T)$ is chemical potential.

At the critical point, the surface free energy is zero and the Gibbs free energy per particle in the gaseous phase is also zero, i.e. $a_v(T) - \mu(T) = 0$. Then $X = 1$ and $Y = 1$ which leads to:

$$P(A) \sim A^{-\tau}. \tag{4.7}$$

When $T < T_c$, the gas phase and liquid phase coexist, the volume energy per particle in liquid phase is equal to the Gibbs free energy per particle in gaseous phase i.e. $a_v(T) - \mu(T) = 0$. Also $a_s(T) > 0$, therefore $Y = 1$ and $X < 1$. When $T > T_c$, if we assume the surface free energy is small ($a_s(T) \sim 0$) and $a_v(T) - \mu(T) > 0$, then $X = 1$ and $Y < 1$. Then around the critical point, equation 4.6 can be written into a power law form where the exponent λ will be temperature dependent:

$$P(A) \sim A^{-\lambda(T)}. \tag{4.8}$$

Then at the critical point T_c, $\lambda(T_c) = \tau$ will be a minimum. This minimum is an experimental observable. For a Van der Waals gas $\tau = 7/3$ [Good84].

4.1.3 Percolation Simulation

In the last ten years, mainly due to increased computing speed, the percolation studies for phase transition phenomena have increased dramatically. Looking at the phase transition problem in a simple microscopic view, the percolation model provides a statistical picture for a phase transition.

Let's do a simple mental experiment. If you threw sticky balls into a two dimensional array of square boxes called a lattice, each box has a probability of p_0 to be occupied. The balls occupying neighboring boxes will stick together to form a cluster. If we have infinite numbers boxes and balls, then when the p_0 is small we only have isolated balls and occasionally some small clusters (two or three balls). As p_0 increase, more big clusters will appear. Then at a certain value of p_0 there would be an infinite cluster (called network) formed and there is only one infinite cluster that can exist even if we further increase p_0. This is a universal phase transition, which means that it is independent of the different lattice structure. The point of p_0 at which the infinite cluster appears is called critical probability p_c. Rather than a theory, percolation is an experiment done by computer with the input of p_0. To compare with experiment, we may view the infinite cluster as a liquid surface and finite clusters as vapor or liquid droplets. If the temperature is high enough, then the probability p_0 is small and only the gas phase exist. But when the temperature decreases, p_0 increases, and more and more condensed droplets are formed. At the critical point, an infinite liquid drop (the liquid surface) is formed. Therefore percolation may be used to understand microscopic picture of a liquid-gas phase transition.

A more realistic percolation model for a liquid-gas phase transition is the bond breaking percolation model [Baue85, Baue86, Baue88, Stau79, Camp86, Camp88, Camp92, Biro86, Barz86, Desb87, Kim89, Phai92]. It assumes an already occupied

infinite lattice with sites connecting to nearest neighbors through potential bonds. Each bond has a probability of p, called bond breaking probability, to break. Then if we increase the bond breaking probability, the number of finite clusters will increase. At the critical probability p_c, the infinite cluster vanishes.

To apply the theory to nuclear fragmentation, a spherically shaped simple cubic lattice is assumed as the initial system. It is also assumed that the bond breaking probability is proportional to the excitation energy per nucleon and inversely proportional to the binding energy per nucleon of the system [Baue88], where

$$p = \frac{E^*}{E_B} = \frac{E^*}{E_{bond} z/2}, \tag{4.9}$$

where E^* is the excitation energy per nucleon and E_B is the binding energy per nucleon and E_{bond} is the bond breaking energy, the maximum energy a bond can absorb. z is the number of nearest neighbours per nucleon. There are two problems with the assumption. First, if the excitation energy is greater than the binding energy, the bond breaking probability is greater than 1 which is physically impossible. Second, the excitation energy for a nuclear reaction is not a direct observable. But the assumption provides a simple link between bond breaking probability to the statistical properties of the highly excited nuclear system which provides a hint concerning the physics of the nuclear break up in terms of how high excitation energy breaks bonds between nucleons in a statistical way. To compare with experimental results, the bond breaking probability is used as fitting parameter [Baue88].

To formulate the percolation results, a phenomenological scaling theory is proposed at the vicinity of the critical point. A cluster size distribution is derived as [Stau79]:

$$n_s = q_0 s^{-\tau} f_u[q_1(p - p_c)s^{\sigma}]; \qquad f_u(0) = 1, \tag{4.10}$$

where n_s is the number of clusters with size s and q_0 q_1 are lattice dependent scale

factors. The exponents σ and τ are lattice independent. At the critical point the cluster distribution for a infinite system is a power law, i.e. $n_s \sim s^{-\tau}$. This microscopic empirical result is similar to the one derived from the droplet model.

The importance of the percolation simulation is that it not only provides us a simple understanding of phase transitions, a class of amazing physical phenomena, from liquid-gas to superconductivity, but also, in the special case of heavy ion reactions, it provides a link between infinite matter phase transitions and a finite system phase transition. One can perform percolation for finite system and fit the experimental results for such phenomena as Z distributions. These results can be extended to infinite nuclear matter by simply increasing the number of sites until the observables do not change.

4.1.4 Observation and Problems

Proton induced reactions, p + Xe, Kr, at beam energy from 80 to 350 GeV were performed by the Purdue group at the Fermilab Internal Target Laboratory [Finn82, Mini82, Hirs84, Hüfn85]. Isotopic resolution of Z=3 to 14 was achieved with kinetic energy acceptance of 5 to 100 MeV. The fragments were measured by two time-of-flight (TOF) spectrometers, one at a laboratory angle of 76° for light fragments (Z $\leq$ 9) and the other positioned at 34 degree laboratory angle for heavy fragments (Z $\leq$ 40). The fragment mass distribution can be fit to a power law with an exponent of 2.64 for Xe and 2.65 for Kr compared with the 2.33 for Van der Waals gas. Later, beam energies of 1 to 19 GeV p + Xe were also used by the Purdue group with the same technique at the Brookhaven Alternating Gradient Synchrotron (AGS). The cluster distributions were fit to a power law and the apparent exponent τ showed a minimum at a proton energy of about 4 GeV. [Mahi88, Pori89]. Figure 4.3 shows the apparent τ parameter as a function of proton energy. A minimum at 4 GeV can be

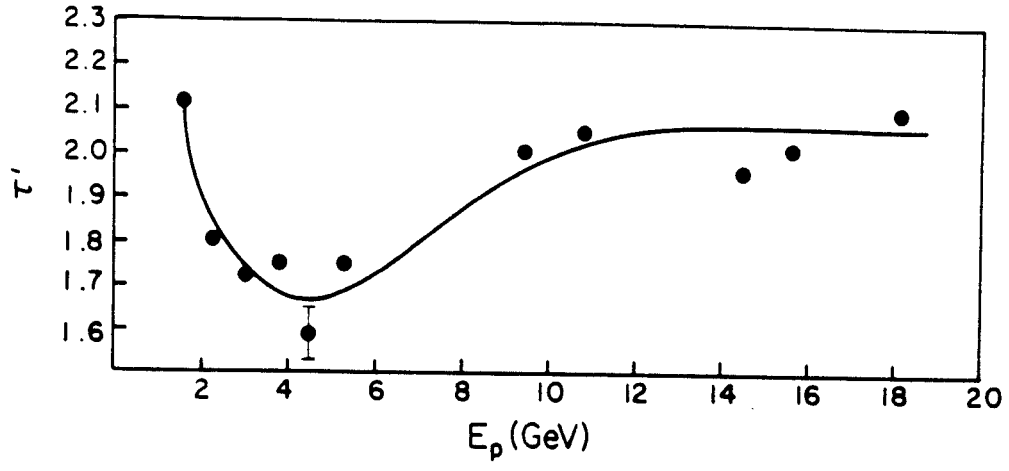

Figure 4.3: Dependence of τ on E_p. The curve is drawn to guide eye (from reference [Mahi88]).

seen.

The intermediate mass fragments production of light ion induced reaction also showed the power law feature [Jako82, Chit83, Yenn90]. The intermediate mass fragments production of ^{3}He + Ag at 480, 900, 1800, 2700 and 3600 MeV, reported by Yennello et. al. can be fit into a power law, and the apparent exponents decrease with beam energy, shown in Figure 4.4. The authors also showed the significant difference of backward angle ($\theta = 140°$) and forward angle ($\theta = 60°$).

Panagiotou et. al. summarized all the inclusive experiments of proton and light ion induced reactions. The temperature of each experiment is obtained either by moving source fit of the kinetic energy spectra or from ideal fermi gas [Pana84]. Then the apparent exponents of power law fitting as a function of temperature was obtained. It showed a temperature of 11-12 MeV. Although critics are strong on the method of

extracting temperature, the analysis did stimulate some further experimental studies.

There are two major problems in the interpretation of these experimental results as a liquid-gas phase transition:

- The fact that inclusive measurements summed over all possible impact parameters implies different deposition of excitation energies into the target nuclei. The excitation energy in the hot nuclear matter which breaks up statistically is uncertain. The mass distribution obtained from inclusive experiment is a sum of "cold" peripheral collisions and "hot" central collisions. The geometrical cross section for peripheral collisions is much larger than central collisions, therefore, it is still not clear if there is a critical behavior for central collisions with maximum excitation energy. Also, the measurements were at certain fixed laboratory angles. Although the authors pointed out that the forward and backward cluster distributions are qualitatively the same, the single angle measurements do not represent a global break up of a hot system.

- Fisher's droplet model is for infinite matter. Using the model without finding a link from infinite matter to finite matter makes the interpretation of the data as a critical behavior weak and unconvincing.

In order to gain an unambiguous understanding, the exclusive measurements in which the excitation energy can be estimated must be done. Also, a global measurement of all the fragments produced during the collision will provide an unambiguous result. The finite size of the system means that the thermodynamic properties such as EOS and phase transition may not be applicable to a system that only has 10^2 particles, because thermolization is the most questionable property for such finite system. Therefore, any equilibrium physics may not be applicable. Even if the phase transitions does exist, the fluctuation due to finite size may wash out any clear sig-

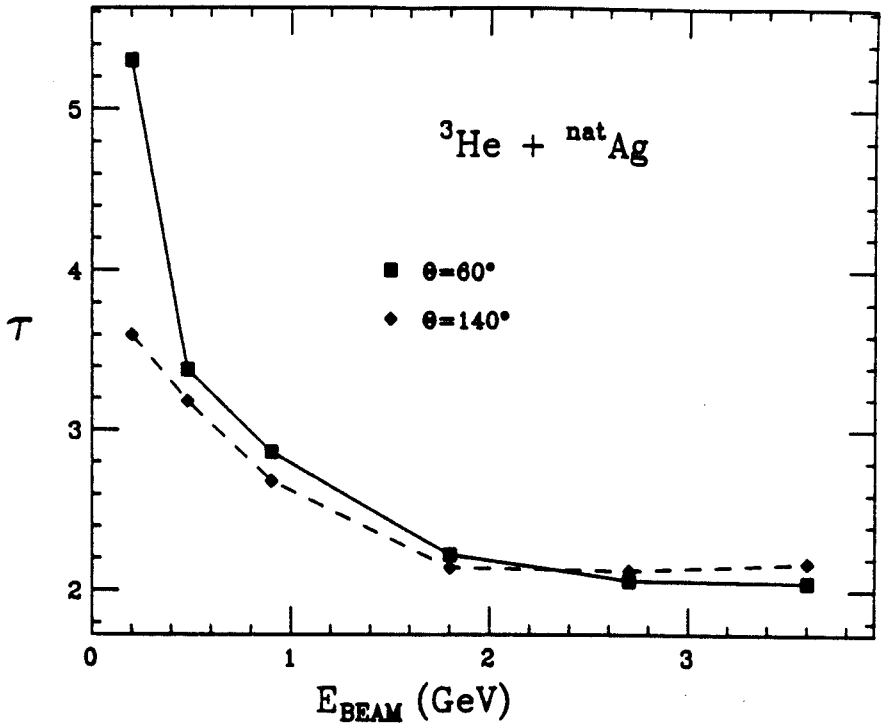

Figure 4.4: The power-law parameter for the ^{3}He + Ag system as a function of total bombarding energy. The power-law fit was performed to Z=4-10 elemental cross-section data (from reference[Yenn90]).

nal, although some theoretical effort has been done to predict the finite size effects [Jaqa84].

To summarize we need to answer the following questions:

- What are the size distributions in global measurement with well characterized impact parameter and excitation energy? Is there critical behavior?
- If the above distributions do exhibit critical behavior, then what are the finite size effects? Can we measure critical temperature for the thermodynamic limit (infinite matter) by finite experiments?

4.2 Experimental Results

In order to maximize the deposition of the excitation energy in the reaction zone for central collisions and also to eliminate the contribution from projectile and target spectators to the fragment distributions, we chose a nearly symmetric system, $^{40}Ar+^{45}Sc$. A wide range of beam energies, from 15 to 115 MeV/nucleon, is used to cover the region where a second order phase transition, predicted by theories, might occur [Boal86, Good84, Kapu84, Glen86, Chit83, Schu82]. An almost global (about 80% of 4π) detection was achieved using the MSU 4π Array [West85, Wils91, Cebr90a]. The low energy threshold, high charge resolution Bragg Curve Counters (BCC) [Cebr91, Li93] combined with fast slow plastic phoswich detectors provide a wide dynamic range for large fragment detection.

According to both Fisher's droplet model and percolation model, the signature of a liquid-gas phase transition is the cluster size distribution which can be parameterized as a power law at and around the critical point. The power law parameter λ reaches a minimum at the critical point. Therefore the measurement of the predicted liquid-gas phase transition will be the measurement of the exit particle size distribution of heavy ion reactions. Because our detectors mainly have excellent Z resolution, the observable measured is the charge distribution. Taking A$\sim$2Z we use Z-distributions as approximation of mass distributions. The 4π detectors have limitations in terms of both kinetic energy and solid angle coverage. The detector acceptance has to be considered before any studies of the experimental result can be understand. A better understanding of detector acceptance will help in the interpretation of the experimental results. In this section, first we look at our detector acceptance and the method we used to correct detector acceptance. Then the corrected and non corrected Z-distributions and conclusions will be presented.

4.2.1 Detector Acceptance Correction

To correct detector acceptance we need two components: simulation events and the detector filter. The simulation events after going through the detector filter have to resemble all the global properties of the experimental data for each beam energy. Then the correction factor can be obtained from the amount of particles rejected by the detector filter comparing with the particles generated by simulation events. Therefore, a most reasonable simulation event generator and a complete detector acceptance filter are needed for a good correction.

Detector Acceptance

There are four quantities in an event array $\mathbf{E} = (Z_i, E_i, \theta_i, \phi_i)$. To measure these four quantities the detector array has limitations for each of them. The kinetic energy acceptance for all three types of detectors are listed in Table 4.1 The 45 forward array (FA) phoswich detectors cover polar angle from 7 to 16 degrees and the solid angle coverage is 51% and the 170 ball phoswich detectors (BA) cover polar angle from 20 to 160 degrees with a solid angle coverage of 83%

The Z acceptance for BCC is from 2 to 12, for Ball phoswich detector is from 1 to 8 with Z=1 isotope resolution, and forward array is also from 1 to 12 with Z=1 isotopic resolution.

We modified the MSU 4π detector phase I filter code written by Ken Wilson [Wils90] to cover the BCCs and a detailed multiple hits correction was also added [Llop93].

Table 4.1: Kinetic Energy acceptance of BCC, Ball phoswich detector and FA phoswich detector for different charge number Z. The p, d, t is for proton, deuteron and triton, respectively.

Z	BCC(MeV/n)	BA phos.(MeV/n)	FA phos.(MeV/n)
p	N/A	21–180	34–135
d	N/A	14–220	23–160
t	N/A	11–220	18–180
2	3–14	14–170	17–164
3	3–17	17–151	17–144
4	4–21	21–160	19–152
5	4–24	24–166	21–157
6	5–28	28–184	24–174
7	5–30	30–187	25–176
8	5–30	30–190	27–178
9	5–30	N/A	27–170
10	6–31	N/A	29–180
11	6–32	N/A	29–174
12	6–33	N/A	32–183

Simulation Events

The major global properties of heavy ion reactions are: multiplicity distribution of the events; charge distribution, i.e. Z-distribution; kinetic energy and angular distributions. In order to obtain correction factor for the Z-distributions, the simulation events have to resemble all the global properties of the real events, i.e. the simulation events after going through the detector filter have to match all the global properties of the experimental data. Since the light particle and the IMF are from different processes in the reaction, we separately generate hydrogen multiplicity, helium multiplicity and IMF multiplicity and match all the multiplicity with experimental data after the detector filter. Then for each IMF particle we generate charge number, Z, from an exponential distribution, i.e. $\sigma(Z) \sim e^{-\beta Z}$, where β is a fitting parameter to be adjusted such that the Z-distribution after the detector filter will match

experimental Z-distribution (we checked with a power law function which gives the same result). For kinetic energy distribution a monte carlo of three Relativistic Boltzmann moving sources have been used. The three source parameters are obtained by fitting experimental kinetic energy spectra in laboratory frame with three Relativistic Boltzmann distribution [West76, Goss77, West82, Jaca87].

Nuclear fireball model assumes the projectile passing through the target and generating three sources which emits particles statistically [West76, Goss77, Goss78]. Shown as Figure 4.5, the intermediate source is the geometrical overlap portion of the projectile and target, which absorbs most of the excitation energy. The projectile source is the remains of projectile and target source is the remains of target. The projectile source moves with a velocity a little less than projectile velocity, while the target source moves with a velocity a little greater than zero in the laboratory frame. The projectile and target sources, also called spectator sources, have less excitation energy than the intermediate source.

If we assume each of the three sources is an independent and thermolized source which emits particle statistically, we can use the relativistic Boltzmann distributions to fit the kinetic spectra of the reaction products.

The relativistic Boltzmann distribution is of the form

$$\frac{d^2\sigma}{p^2 dp d\omega} = \frac{\sigma_0}{4\pi m^3} \frac{e^{-E/\tau}}{2(\tau/m)^2 K_1(m/\tau) + (\tau/m) K_0(m/\tau)}, \tag{4.11}$$

where σ_0 is the cross section, τ is the temperature (or slope parameter), m is the particle mass, E is the particle total energy in the source rest frame, and K_0, K_1 are MacDonald functions. To fit the kinetic energy spectra in laboratory frame, the Boltzmann distribution has to be transformed with the relation

$$\frac{d^2\sigma}{dE d\omega} = pE' \frac{d^2\sigma}{p'^2 dp' d\omega'}, \tag{4.12}$$

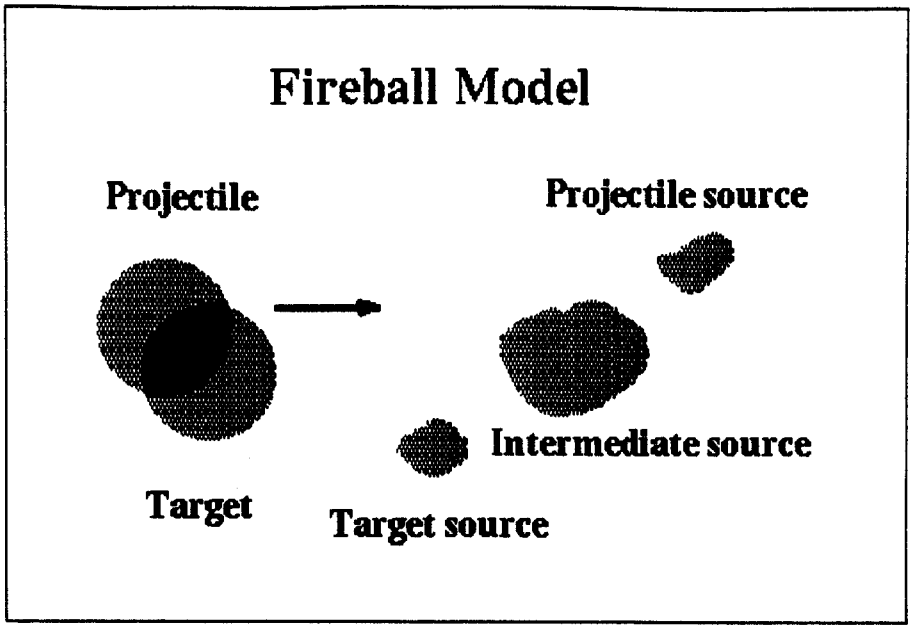

Figure 4.5: Fireball model.

where β is the source velocity in laboratory frame, $E' = \gamma(E - \beta pcos\theta)$ and $\gamma = 1/(1-\beta^2)^{1/2}$. The primed quantities are in the source rest frame and unprimed quantities are in the laboratory frame.

In cooperation with the three source picture, we use a summation of three moving Relativistic Boltzmann sources to fit the particle kinetic energy spectra.

$$\frac{d^2\sigma}{dEd\omega} = \sum_{i=1}^{3} \frac{d^2\sigma_i}{dE_i d\omega_i} \tag{4.13}$$

where $i = 1, 2, 3$ represent target, intermediate, and projectile sources respectively.

To fit the kinetic energy spectra, the three source velocities are fix at 10 % of projectile velocity for target source, 75 % of center of momentum velocity for intermediate source and 90% of projectile velocity for projectile source in laboratory frame. Note that the reaction system is nearly symmetric. The cross section of the three source, σ_i, is normalized such that $\sigma_1 = \sigma_3 = 0.25\sigma_{tot}$ and $\sigma_2 = 0.50\sigma_{tot}$. Then we use a least χ^2 fit to the rest of the parameters. The Z=1 to 5 kinetic energy

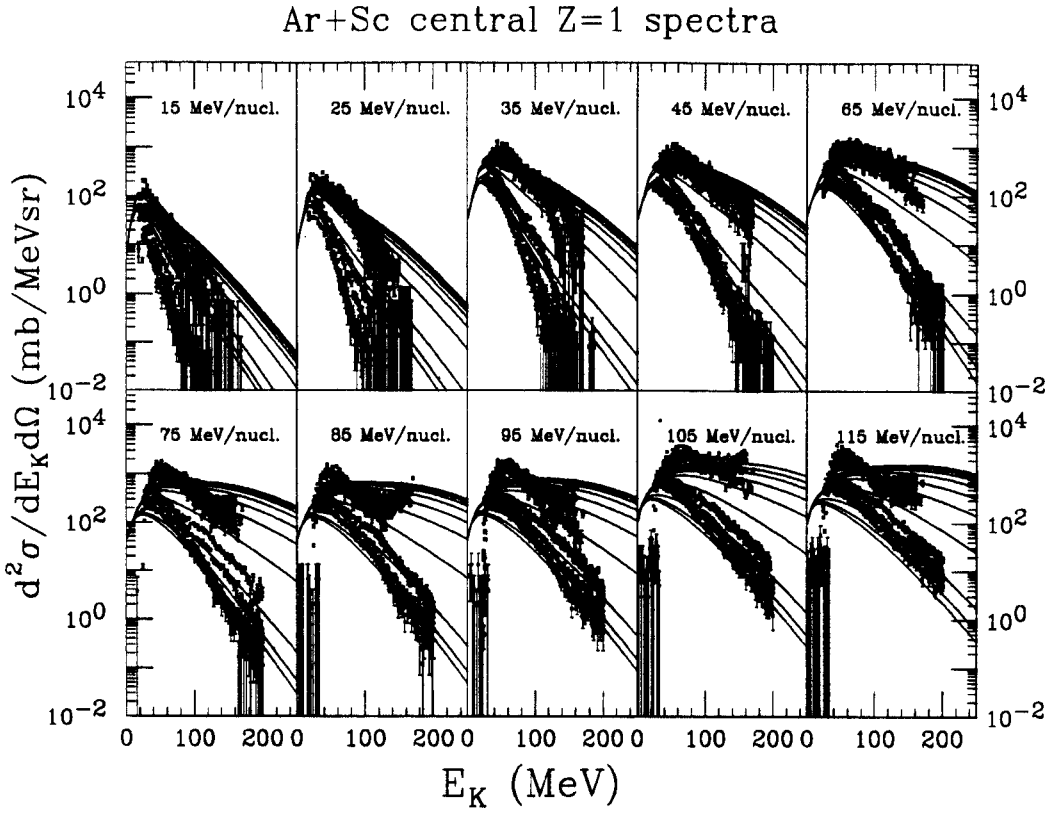

Figure 4.6: Z=1 kinetic energy spectra of Ar + Sc with three moving source fit.

spectra, fit by three moving relativistic Boltzmann source, shown in Figure 4.6 to 4.10. The spectra shown are for $\theta = 7°, 9°, 11°, 14°, 18°, 23°, 32°, 46°, 52°, 55°$. Figure 4.11 to 4.13 are kinetic energy spectra of proton, deuteron and triton for angle 23°, 32°, 46°, 52° and 55°.

The following is the logic of the simulation:

1. Multiplicity:

   Generate hydrogen multiplicity - Gaussian, input: mean, width

   Generate helium multiplicity - Gaussian, input: mean, width

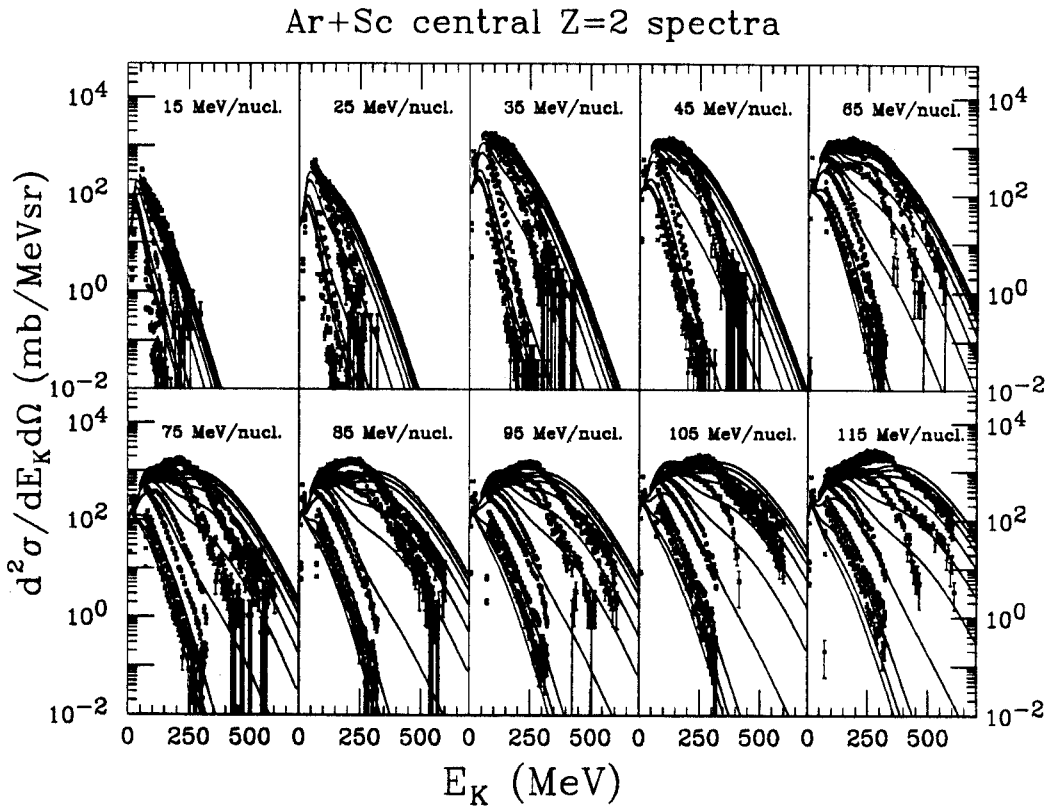

Figure 4.7: Z=2 kinetic energy spectra of Ar + Sc with three moving source fit.

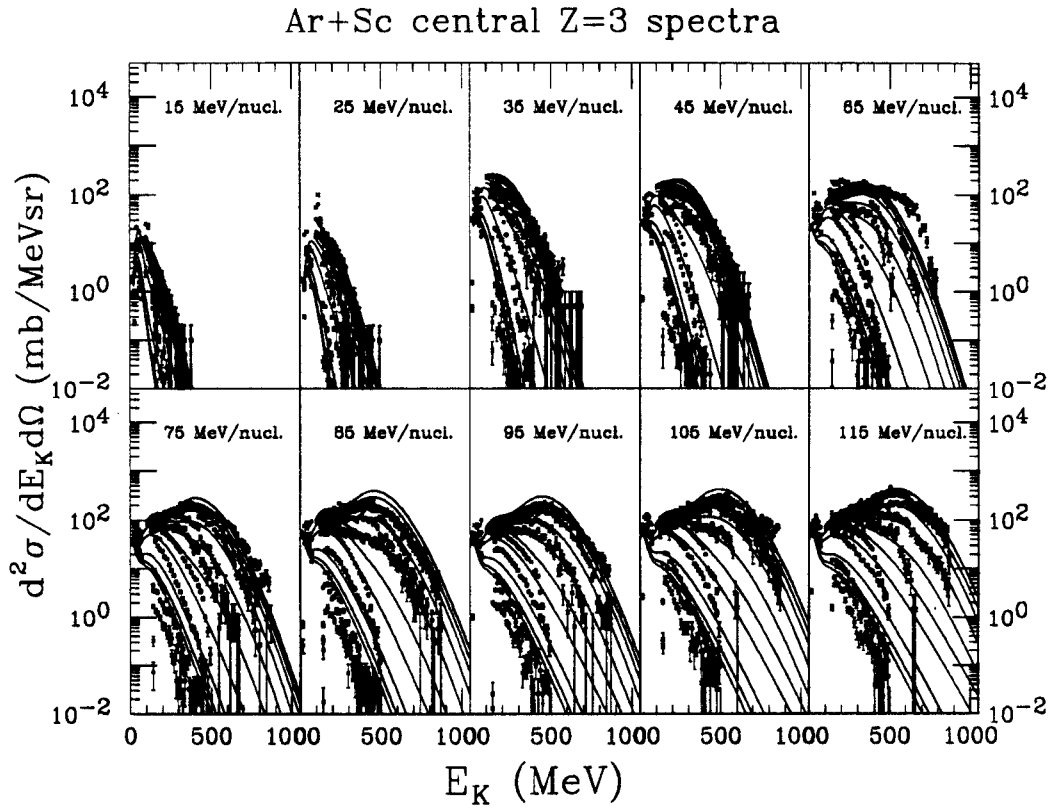

Figure 4.8: Z=3 kinetic energy spectra of Ar + Sc with three moving source fit.

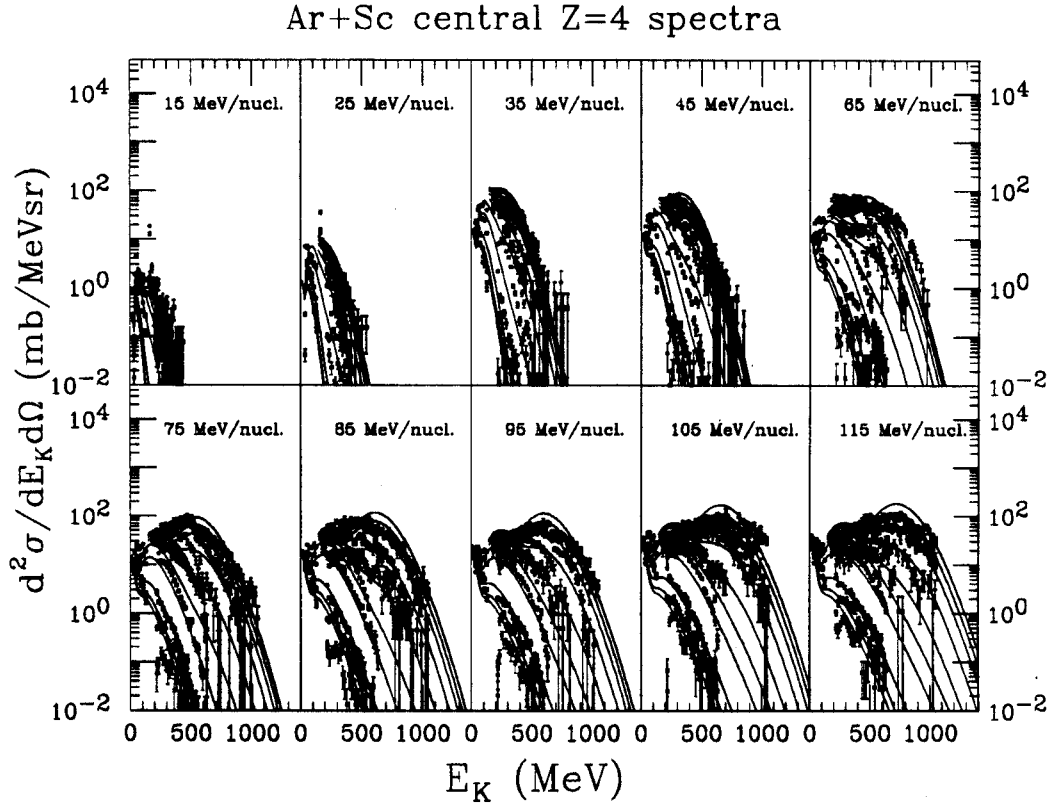

Figure 4.9: Z=4 kinetic energy spectra of Ar + Sc with three moving source fit.

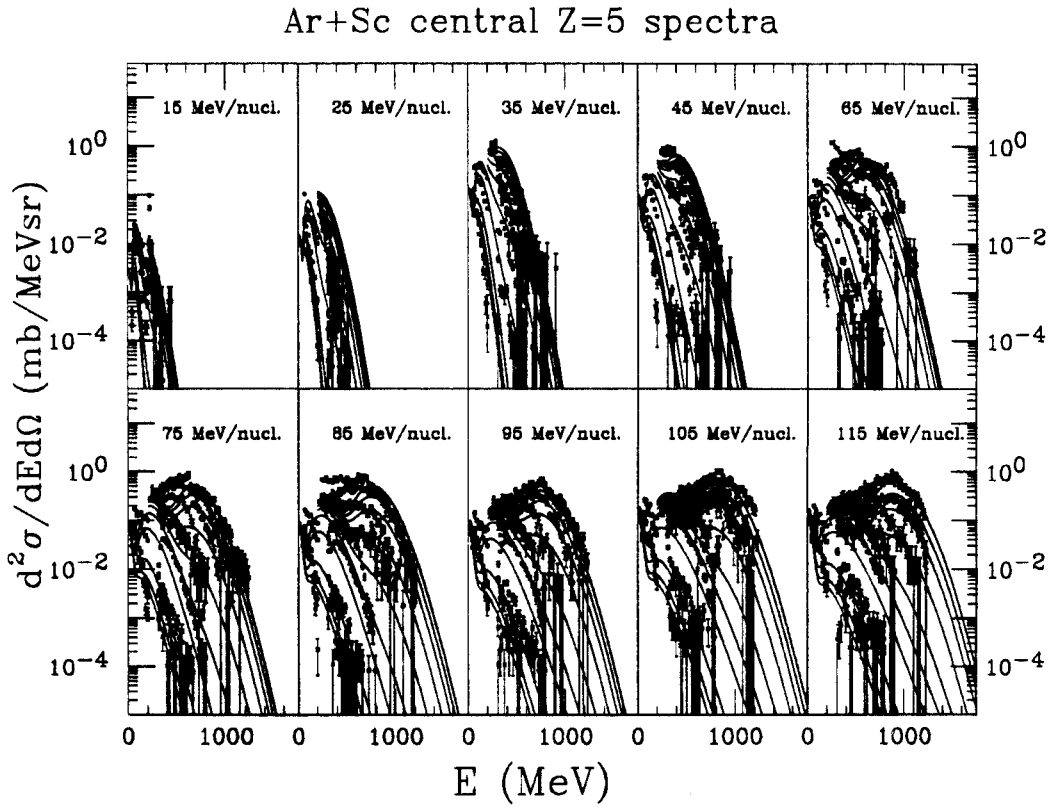

Figure 4.10: Z=5 kinetic energy spectra of Ar + Sc with three moving source fit.

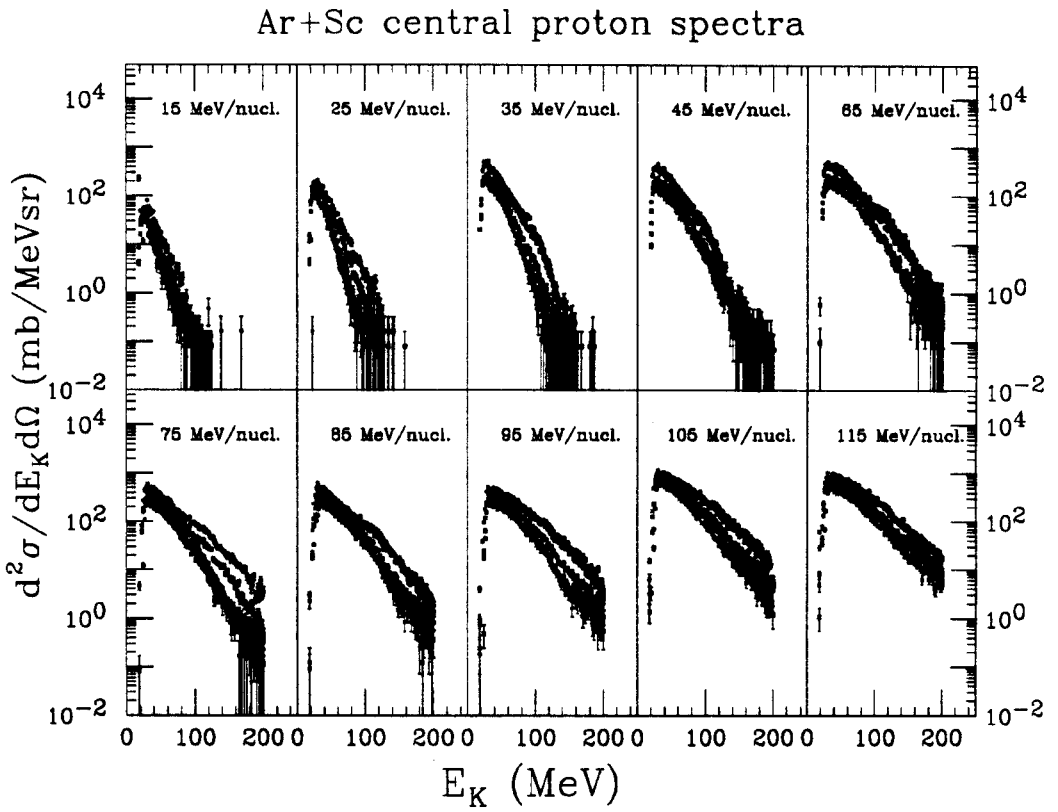

Figure 4.11: Proton kinetic energy spectra of Ar + Sc.

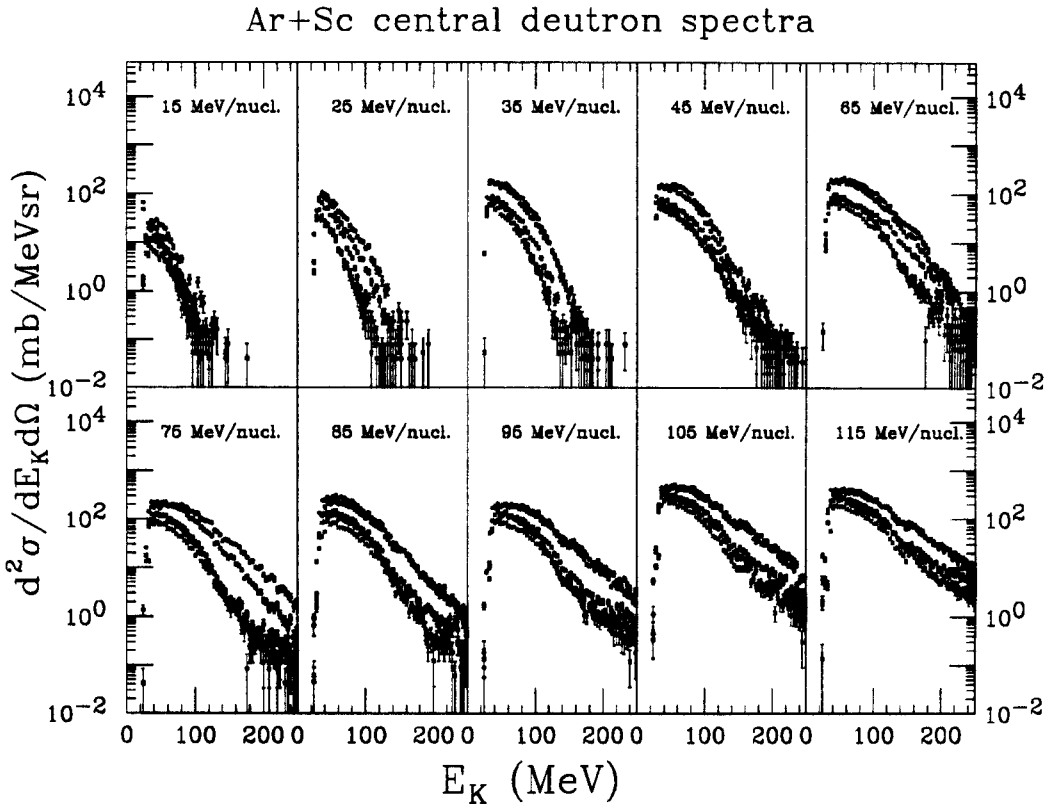

Figure 4.12: Deuteron kinetic energy spectra of Ar + Sc.

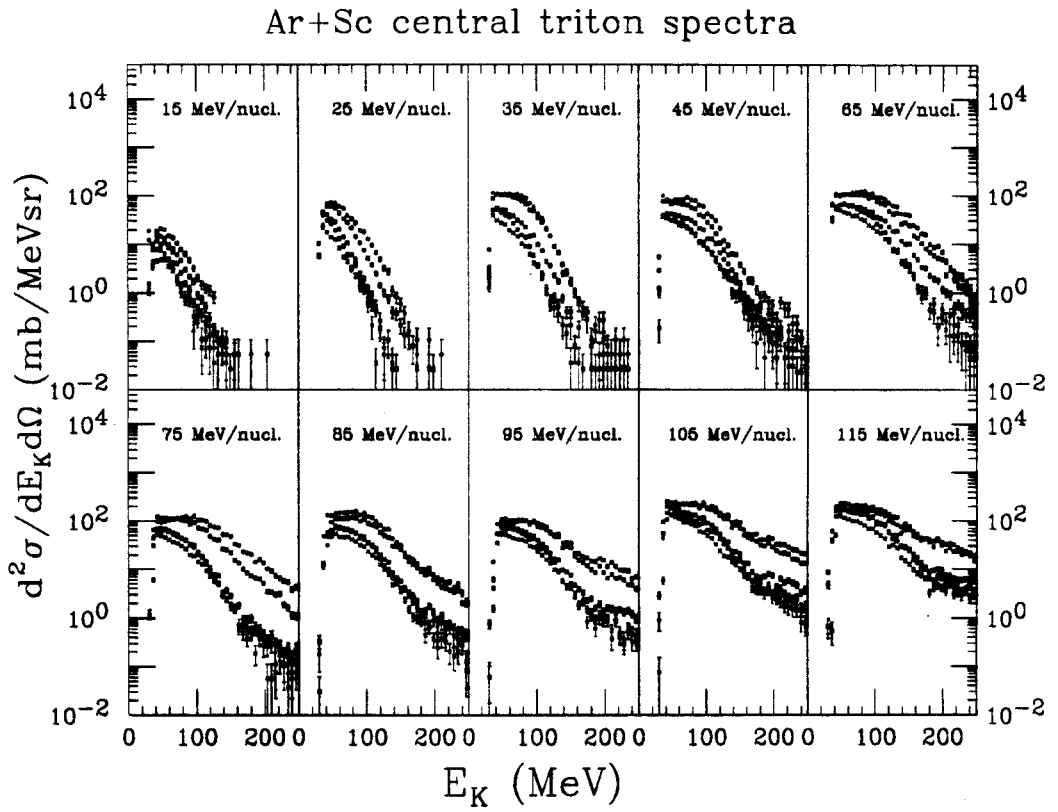

Figure 4.13: Triton kinetic energy spectra of Ar + Sc.

Generate IMF multiplicity - Gaussian, input: mean, width

2. Charge distribution:

   Generate IMF particle charge - Exponential, input: λ

   Check total charge conservation.

3. Kinetic energy of each particle:

   Determine which source the particle is emitted.

   Go to the source with T_i, V_i,

   i=1 - target source

   i=2 - intermediate source

   i=3 - projectile source.

4. Write out simulated event array:

   $E_{sim}(Z_i, E_i, \theta_i, \phi_i)_{i=1}^{M}$,

5. Go through detector filter.

6. Analyze the event array after the filter.

7. Compare the global properties:

   a) hydrogen multiplicity distribution

   b) helium multiplicity distribution

   c) IMF multiplicity distribution

   d) Z-distribution.

8. Obtain correction factor for each Z.

Figure 4.14 to 4.23 show the simulation comparing with experimental data for 15 to 115 MeV/nucleon Ar + Sc. The dashed curves are the simulation events before the detector filter and the solid curves are the simulation events after the detector filter and plotted symbols are the experimental data. The frames from the top to the bottom are hydrogen multiplicity, helium multiplicity, IMF multiplicity, total

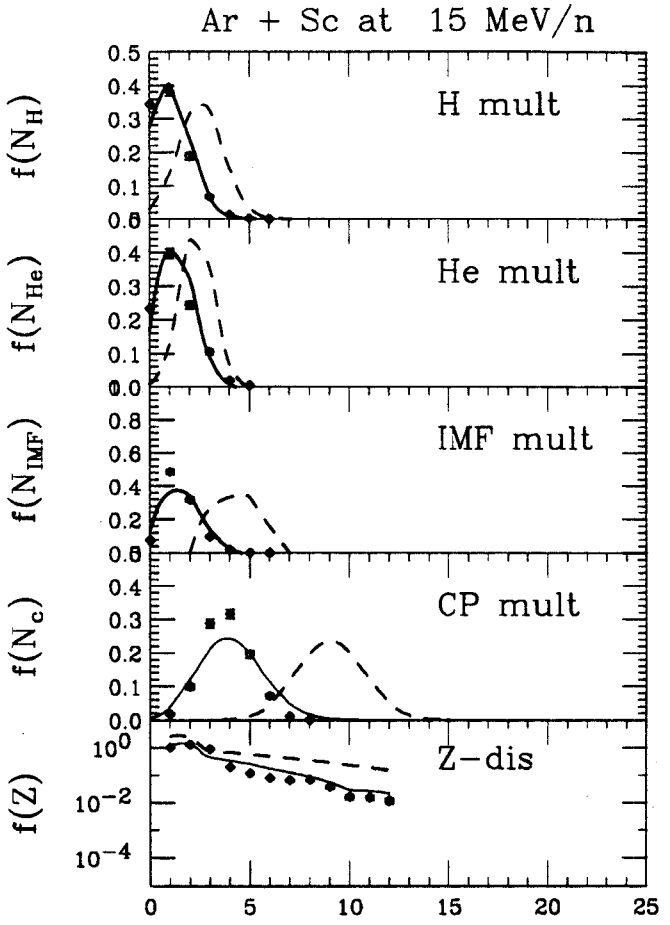

Figure 4.14: Simulation Events for Ar + Sc at 15 MeV/nucleon after the detector filter comparing with experimental data. The dashed curves are simulation before the detector filter, solid curves are simulation events after the detector filter and plotted symbols are the experimental result. From top to bottom frames: hydrogen multiplicity, helium multiplicity, IMF multiplicity, total charged particle multiplicity distributions and Z-distribution.

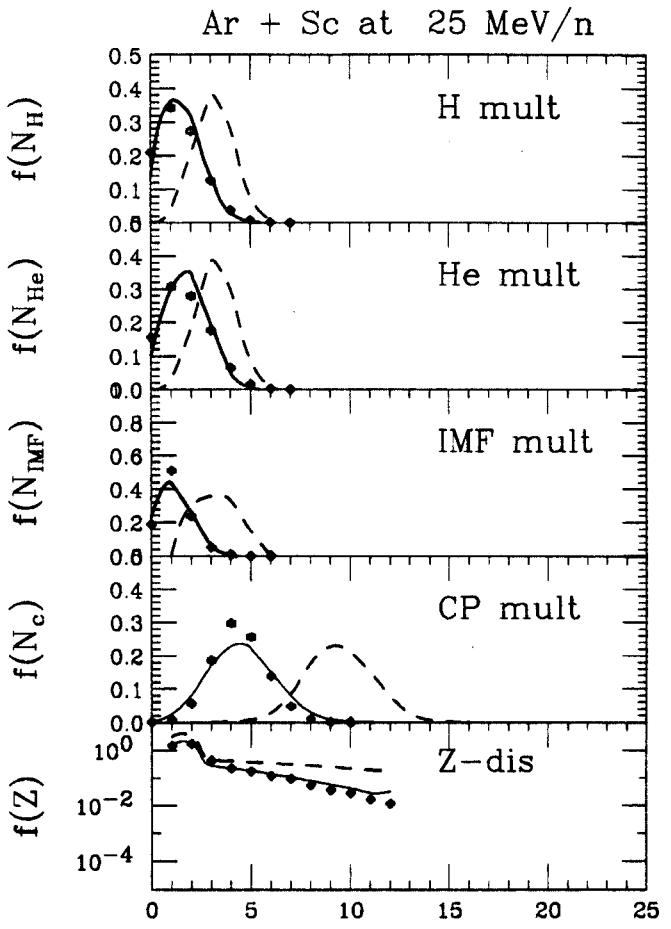

Figure 4.15: Simulation Events for Ar + Sc at 25 MeV/nucleon after filter comparing with experimental data. The dashed curves are simulation before the detector filter, solid curves are simulation events after the detector filter and plotted symbols are the experimental result. From top to bottom frames: hydrogen multiplicity, helium multiplicity, IMF multiplicity, total charged particle multiplicity distributions and Z-distribution.

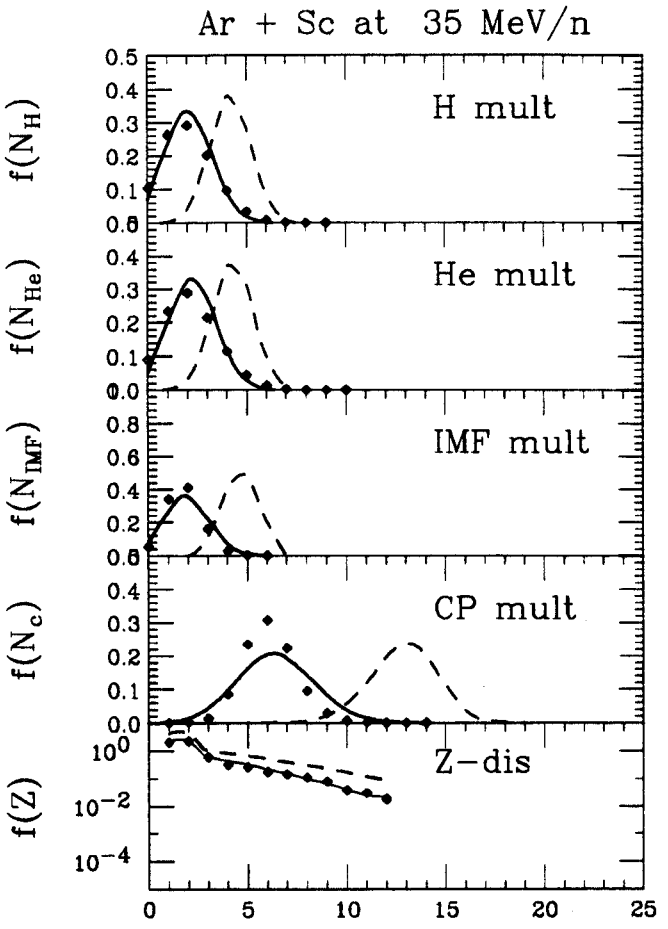

Figure 4.16: Simulation Events for Ar + Sc at 35 MeV/nucleon after the detector filter comparing with experimental data. The dashed curves are simulation before the detector filter, solid curves are simulation events after the detector filter and plotted symbols are the experimental result. From top to bottom frames: hydrogen multiplicity, helium multiplicity, IMF multiplicity, total charged particle multiplicity distributions and Z-distribution.

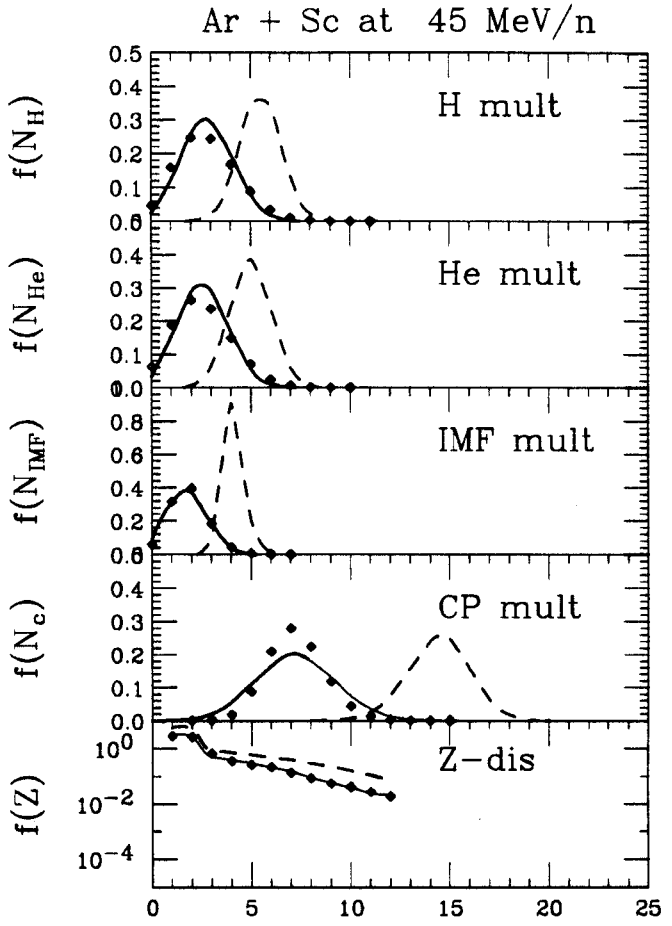

Figure 4.17: Simulation events for Ar + Sc at 45 MeV/nucleon after the detector filter comparing with experimental data. The dashed curves are simulation before the detector filter, solid curves are simulation events after the detector filter and plotted symbols are the experimental result. From top to bottom frames: hydrogen multiplicity, helium multiplicity, IMF multiplicity, total charged particle multiplicity distributions and Z-distribution.

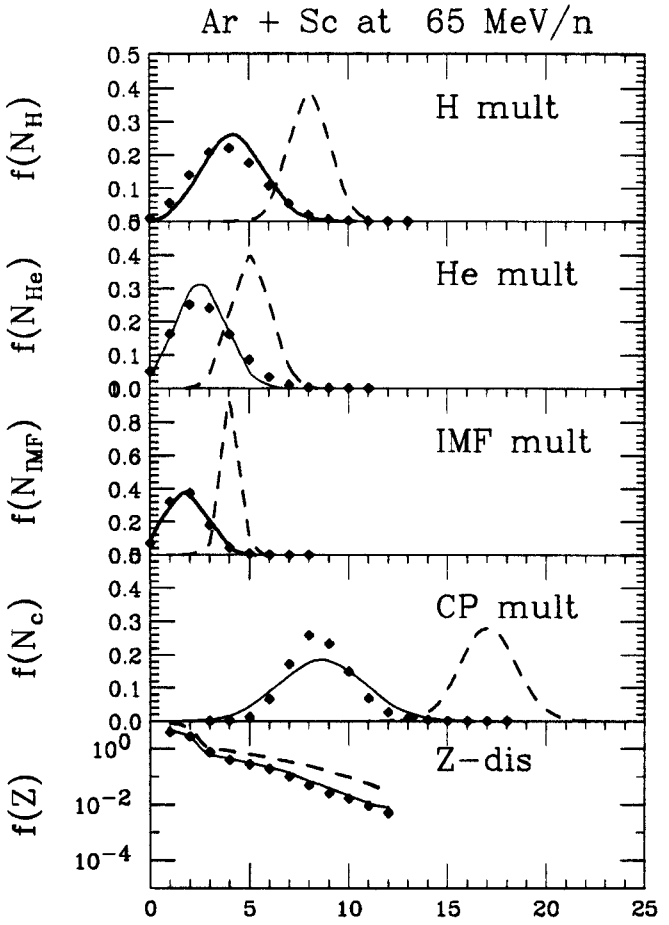

Figure 4.18: Simulation events for Ar + Sc at 65 MeV/nucleon after the detector filter comparing with experimental data. The dashed curves are simulation before the detector filter, solid curves are simulation events after the detector filter and plotted symbols are the experimental result. From top to bottom frames: hydrogen multiplicity, helium multiplicity, IMF multiplicity, total charged particle multiplicity distributions and Z-distribution.

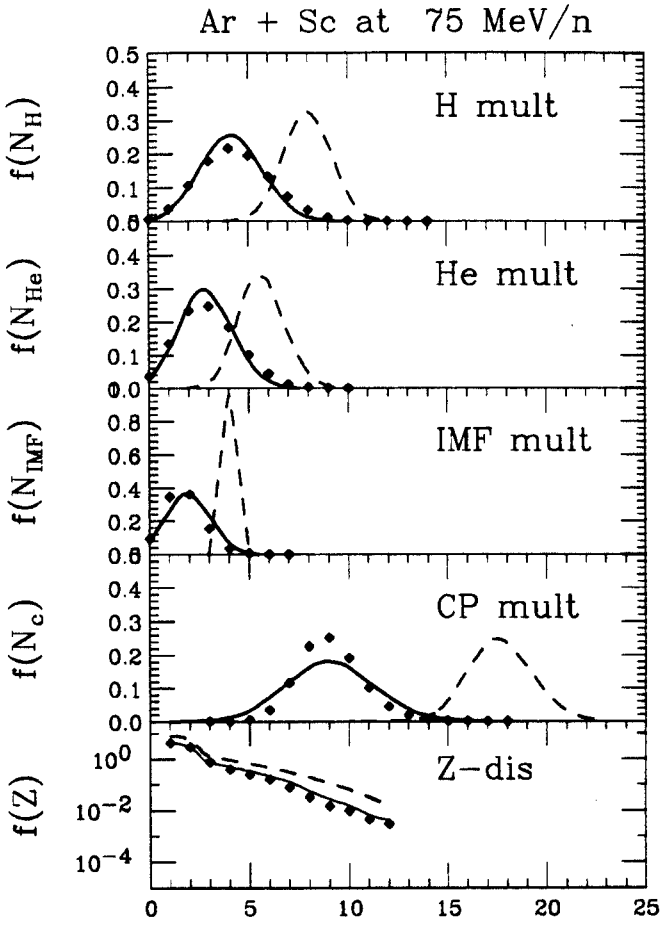

Figure 4.19: Simulation events for Ar + Sc at 75 MeV/nucleon after the detector filter comparing with experimental data. The dashed curves are simulation before the detector filter, solid curves are simulation events after the detector filter and plotted symbols are the experimental result. From top to bottom frames: hydrogen multiplicity, helium multiplicity, IMF multiplicity, total charged particle multiplicity distributions and Z-distribution.

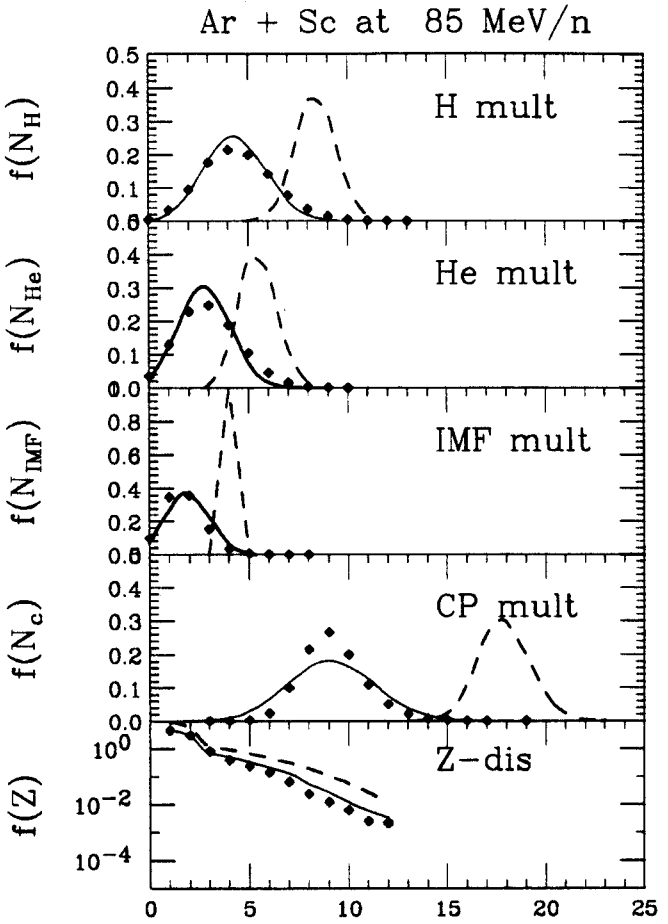

Figure 4.20: Simulation events for Ar + Sc at 85 MeV/nucleon after the detector filter comparing with experimental data. The dashed curves are simulation before the detector filter, solid curves are simulation events after the detector filter and plotted symbols are the experimental result. From top to bottom frames: hydrogen multiplicity, helium multiplicity, IMF multiplicity, total charged particle multiplicity distributions and Z-distribution.

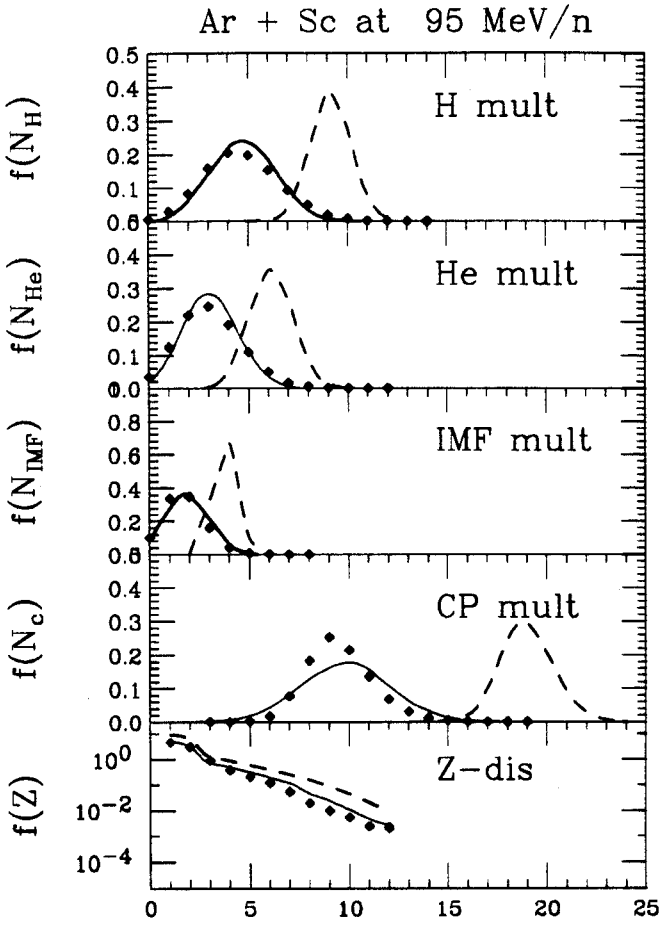

Figure 4.21: Simulation events for Ar + Sc at 95 MeV/nucleon after the detector filter comparing with experimental data. The dashed curves are simulation before the detector filter, solid curves are simulation events after the detector filter and plotted symbols are the experimental result. From top to bottom frames: hydrogen multiplicity, helium multiplicity, IMF multiplicity, total charged particle multiplicity distributions and Z-distribution.

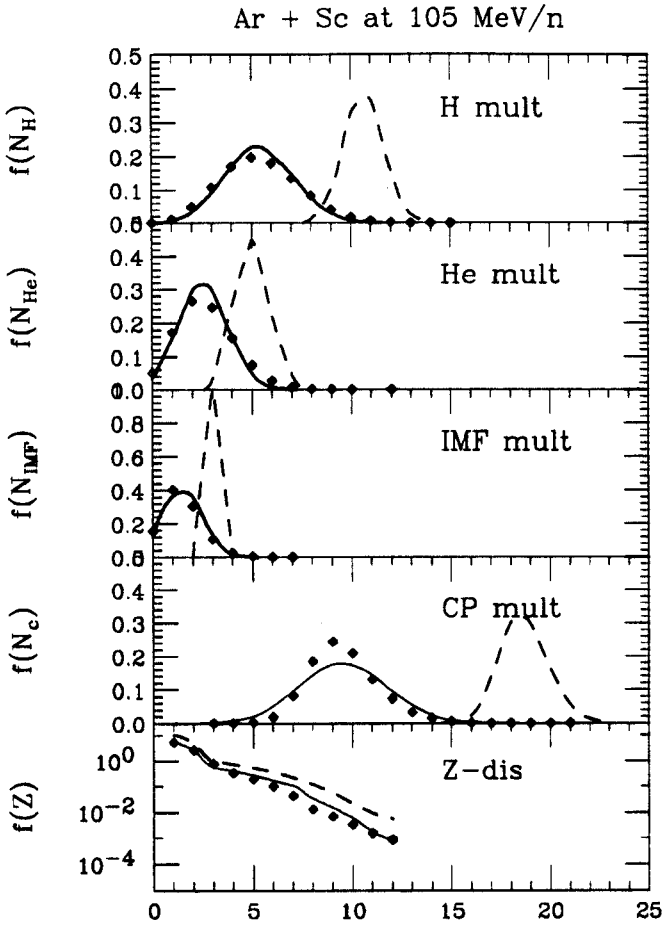

Figure 4.22: Simulation events for Ar + Sc at 105 MeV/nucleon after the detector filter comparing with experimental data. The dashed curves are simulation before the detector filter, solid curves are simulation events after the detector filter and plotted symbols are the experimental result. From top to bottom frames: hydrogen multiplicity, helium multiplicity, IMF multiplicity, total charged particle multiplicity distributions and Z-distribution.

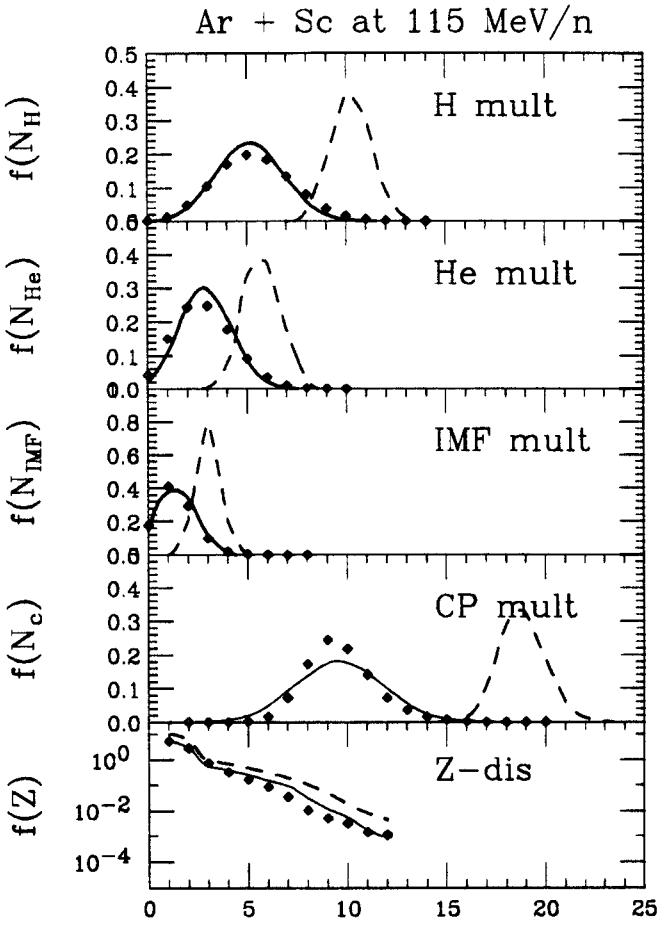

Figure 4.23: Simulation events for Ar + Sc at 115 MeV/nucleon after the detector filter comparing with experimental data. The dashed curves are simulation before the detector filter, solid curves are simulation events after the detector filter and plotted symbols are the experimental result. From top to bottom frames: hydrogen multiplicity, helium multiplicity, IMF multiplicity, total charged particle multiplicity distributions and Z-distribution.

charged particle multiplicity and Z-distribution, respectively. The distributions are normalized to one. i.e.

$$\int_0^\infty f(x)dx = 1$$

where $x = N_p$, N_{He}, N_{IMF}, N_c as different multiplicities and the Z-distribution is normalized by total number of events:

$$f(Z) = N(Z)/N_{event}$$

where $N(Z)$ is the counts of particles with Z and N_{event} is the total number of events analyzed. The error bars on experimental data are all statistical.

4.2.2 Corrected Z-Distribution

From the simulation we can get the ratio of total cross section for each Z after the detector filter vs. total cross section generated by the simulation $\alpha(Z) = f_{bf}(Z)/f_{af}(Z)$ where f_{bf} is the Z-distribution before the filter and $f_{af}(Z)$ is the distribution after the filter. Then the corrected Z-distribution can be obtained

$$\sigma_{cr}(Z) = \alpha(Z)\sigma_d(Z)$$

Where $\sigma_{cr}(Z)$ is the corrected cross section and $\sigma_d(Z)$ is the uncorrected cross section.

Both corrected and uncorrected Z-distributions are shown in Figure 4.24. The experimental data are shown by histogram and the corrected Z-distributions are shown by the solid circles. We fit the corrected Z-distributions to both a power law function, $\sigma(Z) = \sigma_0 Z^{-\lambda}$ (σ_0 and λ are fitting constants) shown as the dashed curves and an exponential, $\sigma(Z) = \sigma_0 e^{-\beta Z}$ (σ_0 and β are fitting constants), shown as the straight lines.

Both power law and exponential fitting parameters are listed in Table 4.2.

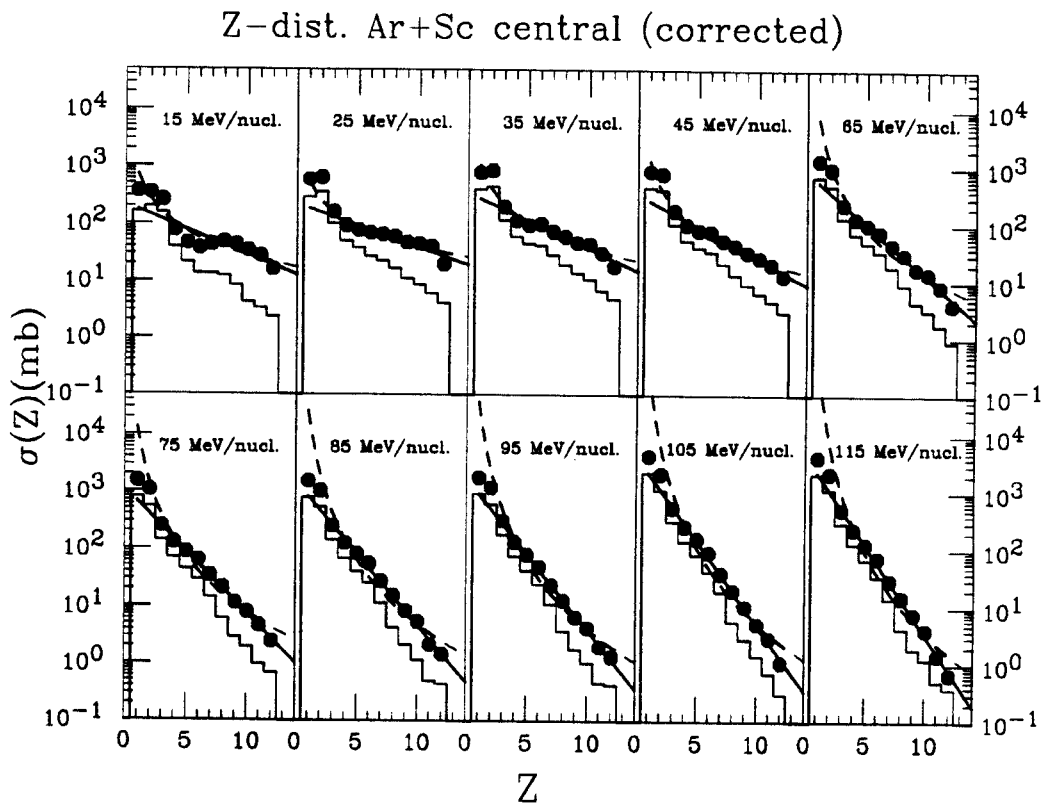

Figure 4.24: Z-distributions of Ar+Sc from 15 to 115 MeV/nucleon. The histograms are experimental data and the solid circles are data corrected for detector acceptance.

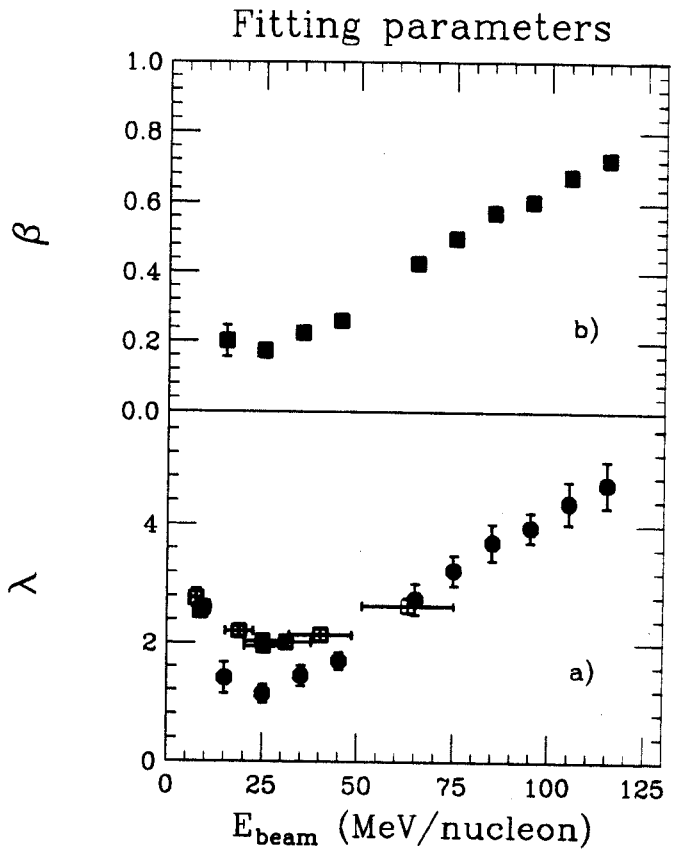

Figure 4.25: The exponential parameter and power law parameter vs. beam energy. The top frame is the exponential slope parameter and the bottom frame is the power law parameter λ vs. beam energy. The solid circles are the fitting parameters for the data corrected for detector acceptance and the open squares are GSI data: Au+C,Al,Cu at 600 MeV/nucleon

Table 4.2: The exponential and power law fitting parameters. The χ^2 is calculated per degree of freedom.

E beam	exponential			power law		
(MeV/A)	β	$d\beta$	χ^2	λ	$d\lambda$	χ^2
15	0.201	0.046	23.51	1.409	0.263	12.24
25	0.173	0.021	2.11	1.136	0.155	1.52
35	0.224	0.018	1.72	1.449	0.169	2.58
45	0.261	0.012	0.93	1.701	0.143	1.59
65	0.427	0.015	0.78	2.755	0.260	7.63
75	0.499	0.010	0.43	3.241	0.256	8.06
85	0.573	0.014	0.57	3.711	0.311	11.84
95	0.604	0.011	0.92	3.956	0.250	9.18
105	0.675	0.013	1.10	4.375	0.357	34.41
115	0.724	0.014	0.97	4.688	0.389	35.11

The χ^2 shown in Table 4.2 is calculated for χ^2 per degree of freedom for Z=3 to Z=12. The χ^2 for the power law fit is smaller at and around the minimum while χ^2 is smaller for the exponential fit at higher beam energy. The χ^2 per degree of freedom vs. beam energy is shown in Figure 4.26.

The errors of the fitting parameters are calculated by changing χ^2 by 1. These fitting parameters are plotted in Figure 4.25. The top frame shows the exponential fitting parameter β vs. beam energy (MeV/nucleon) and the bottom frame shows the power law fitting parameter λ. The open circles are the fits for experimental data without correction for detector acceptance and the solid circles are the fits of data corrected for detector acceptance. We can see a minimum at about 25 MeV/nucleon. In the bottom frame we also plot the GSI data: Au+C, Al, Cu at 600 MeV/n [Ogil91]. The equivalent beam energy for GSI data is calculated from the excitation energy given by reference [Ogil91] to an equivalent excitation energy of a symmetric system assuming a complete inelastic collision. The λ parameters of both sets of data show a clear minimum, but the minimum of λ is smaller for Ar + Sc system; and also the

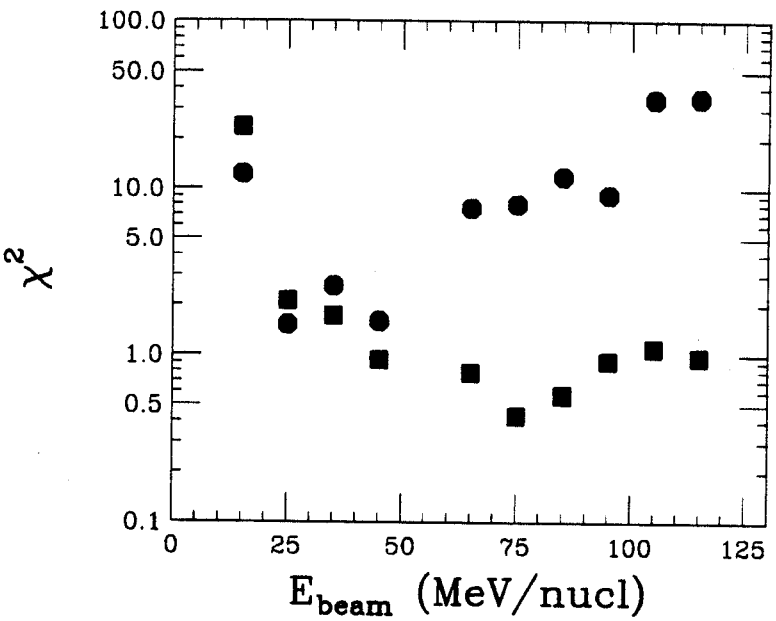

Figure 4.26: The χ^2 per degree of freedom of power law and exponential fits to the Z-distribution vs. beam energy.o The solid squares are the power law fits and solid circles are exponential fits.

λ_{min} of Ar + Sc is much smaller than the theoretical prediction of $2.0 \leq \lambda \leq 2.6$. The difference of the minimum λ value is believed due to the size difference of the two reaction system which will be discussed in the next section.

4.2.3 Summary of Experimental Result

- The Z-distributions of Ar + Sc from 15 to 115 MeV/nucleon can be fitted by both exponential and power law. There is a minimum at about 25 MeV/nucleon beam energy for both power law apparent exponent and the slope of exponential function.

- The exponential χ^2 is smaller at high beam energy which is far from the minimum and the χ^2 of power law fitting is smaller when close to the minimum as expected by theories.

- Comparing with GSI experiment of Au + C, Al, Cu at 600 MeV/nucleon, the minimum of power law parameter λ is smaller for Ar + Sc.

4.3 Percolation Calculation

As mentioned in section 1.1.3, the bond breaking percolation model is a microscopic simulation of the liquid-gas phase transition. It is assumed that each particle is "linked" with nearest neighbors by a potential bond. Each bond can absorb a maximum energy called the bond breaking energy, E_b, and has a probability of P_b to break. Such simulations have allowed the fitting of P_b to experimental data [Baue88].

4.3.1 Basic Assumptions

In the present work, we assume that the energy distributed into each bond, ϵ_b, can be described by a Boltzmann distribution with a mean energy $\langle \epsilon_b \rangle$. Each site of the

lattice has an average of α bonds. The average excitation energy deposited per site is $\langle E_s \rangle = \alpha \langle \epsilon_b \rangle$; and the binding energy per nucleon of the initial nuclear system is $B = \alpha E_b$. When the system expands, any bond which has an energy greater than E_b will break, therefore, the bond breaking probability is:

$$\begin{aligned} P_b &= \int_{E_b}^{\infty} \sqrt{\epsilon_b} e^{-\epsilon_b/t_b} d\epsilon_b \Big/ \int_0^{\infty} \sqrt{\epsilon_b} e^{-\epsilon_b/t_b} d\epsilon_b \\ &= \int_B^{\infty} \sqrt{E_s} e^{-E_s/T_s} dE_s \Big/ \int_0^{\infty} \sqrt{E_s} e^{-E_s/T_s} dE_s. \end{aligned} \tag{4.14}$$

Where $t_b = \frac{2}{3}\langle \epsilon_b \rangle$ and $T_s = \alpha t_b = \frac{2\alpha}{3}\langle \epsilon_b \rangle = \frac{2}{3}\langle E_s \rangle$ are slope parameters. We note that the bond breaking probability P_b calculated by equation 4.14 is independent of α. Thus the calculation is independent of the lattice structure.

We also note in passing that this approach is consistent with the introduction of the mean coordination, $\langle c \rangle \equiv \alpha \cdot (1 - p_b)$. It can be shown that, for example, the mean multiplicity of clusters per lattice site is very different for different lattice structures when plotted as a function of p_b. But there is hardly a difference between different lattice structures, if one plots the same quantity against $\langle c \rangle$. This is again an example of the independence of the physical quantities from the lattice structure, once the trivial α-dependence is removed.

It should also be pointed out here that the relevant degrees of freedom in the above equation are *not* the bonds (the number of which is somewhat arbitrary and dependent on the specific lattice structure chosen), but the sites (i.e. nucleons), whose number is fixed. We chose to use the classical Boltzmann statistics, but at the excitation energies relevant here and in the limit of large number of nucleons, this classical approximation should be sufficient. One can also obtain a formula similar to the one above by constructing an analogy between the bond percolation model and the Ising model of ferromagnets [Coni79, Herr81, Bind84].

By fitting the proton kinetic energy spectra with a single moving Boltzmann source

[West76, West82, Jaca87], we obtain the slope parameters T_s for each beam energy.

4.3.2 Source Size

The initial size of the lattice for the percolation calculation is assumed to be given by the fireball geometry for an overlap region of projectile and target with impact parameter of 0.25 b_{max} where b_{max} is the sum of the radii of the projectile and the target nuclei. We used an initial cubic lattice of 68 sites for ^{40}Ar + ^{45}Sc with impact parameter of 0.25 b_{max}. Also 150 sites is used for the Au + C, Al, Cu, GSI experiment. A spherical shaped lattice is assumed for both calculations.

4.3.3 Result of the Percolation

The bond breaking probabilities are calculated by equation 4.14 using the slope parameters of protons and a binding energy of 7.8 MeV/nucleon. The binding energy was used as a fitting parameter. The slope parameters of protons are obtained by fitting proton kinetic energy spectra with a single moving Boltzmann source. Figure 4.27 shows the moving source fit for θ=32°, 46°, 52°, 55°, 65° laboratory polar angle. We also compare this calculation to the fragmentation data of 600 MeV/nucleon Au + C, Al, C in reference [Ogil91]. We convert the excitation energies calculated by reference [Ogil91] to beam energies of a symmetric system (projectile and target have equal masses) assuming a totally inelastic collision. Then the same beam energy as ^{40}Ar + ^{45}Sc and proton slope parameters are used with an initial lattice of 150 sites to reproduce the Au + C, Al, Cu data. For Au + C, Al, Cu. A 7.0 MeV/nucleon binding energy was used.

Figure 4.28 a) shows the bond breaking probability vs. slope parameter T_s calculated using equation 4.14 with B = 7.0 MeV/nucleon (dotted curve) and B = 7.8 MeV/nucleon (solid curve). The slope parameters for each beam energy are shown

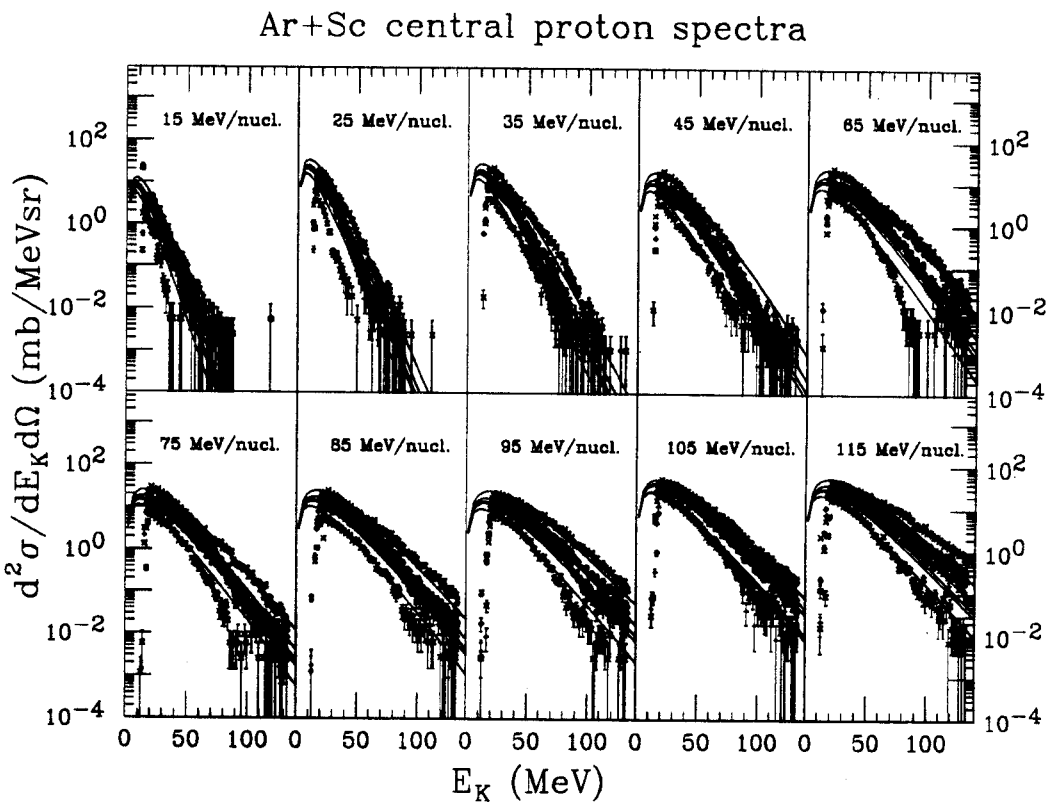

Figure 4.27: Proton kinetic spectra for Ar + Sc fitted by a single moving Boltzmann source.

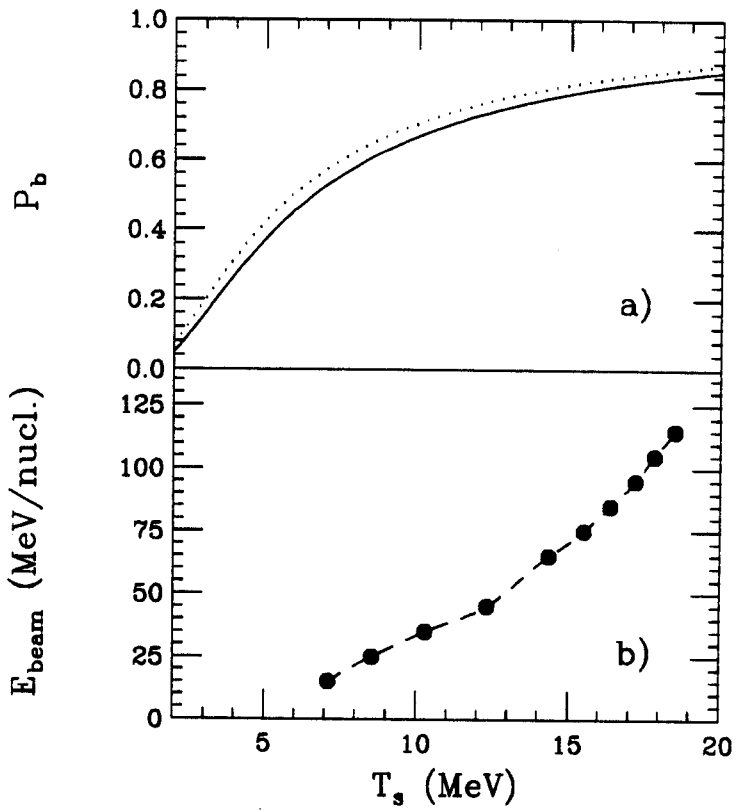

Figure 4.28: The beam energy vs. kinetic energy slope parameter of proton (bottom frame) and bond breaking probability vs. the slope parameter (top frame). The dotted curve is for a binding energy of 7.0 MeV/nucleon and the solid curve is for a binding energy of 7.8 MeV/nucleon.

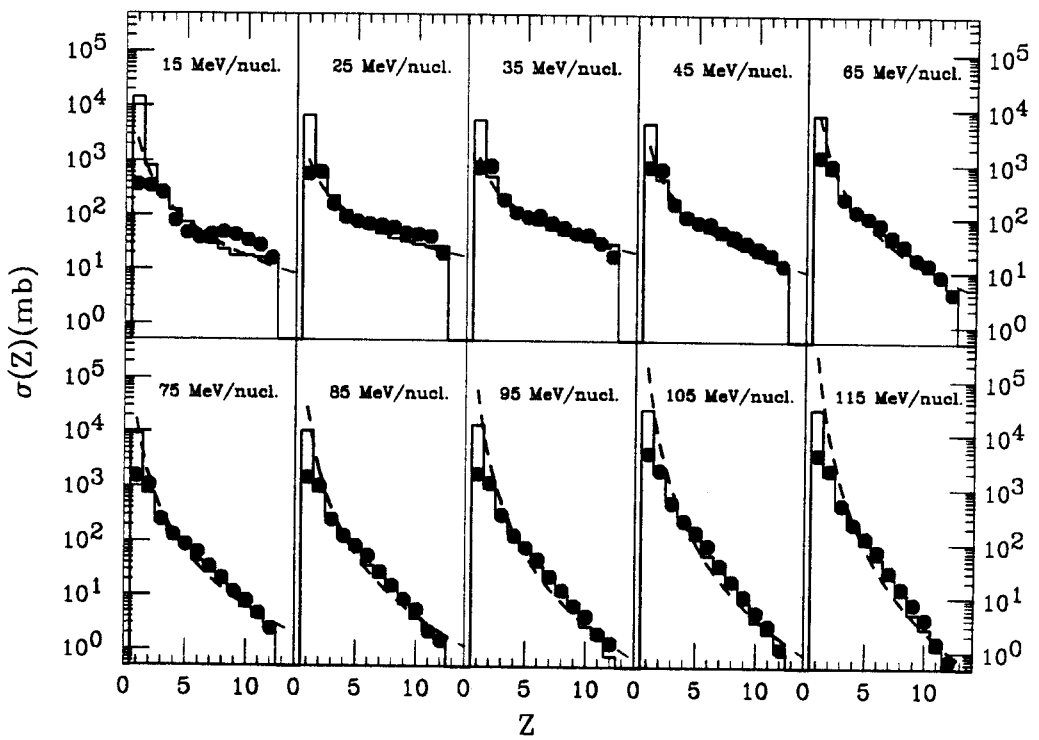

Figure 4.29: Z-distributions of Ar+Sc at 15 to 115 MeV/nucleon. The histograms are the percolation calculation, the solid circles are data corrected for detector acceptance. The straight line is the fitting of the percolation Z-distribution to an exponential function $\sigma(Z) = \sigma_0 e^{-\beta Z}$ and the dashed curves are the fitting of the percolation Z-distributions to a power law $\sigma(Z) = \sigma_0 Z^{-\lambda}$

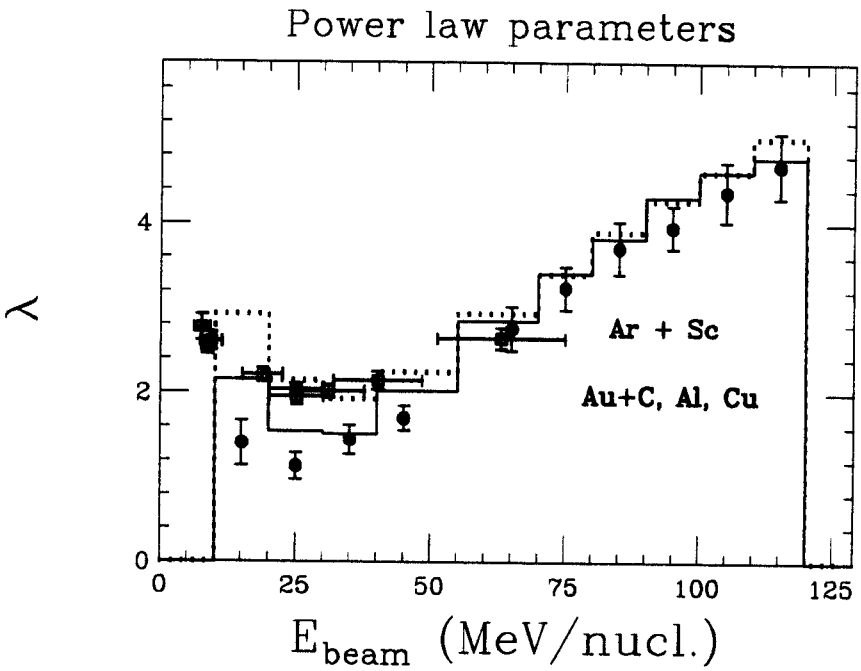

Figure 4.30: The λ parameter of the power law fit. The solid circles are the power law fit to the corrected experimental data of Ar + Sc at 15 to 115 MeV/nucleon and the open squares are the power law fit to the experiment of Au + C, Al, Cu at 600 MeV/nucleon. The solid histogram is the power law fit to the percolation calculations with lattice size of 68 and a binding of 7.8 MeV/nucleon, the dashed histogram is the percolation with lattice size of 150 and a binding energy of 7.0 MeV/nucleon.

in Figure 4.28. Figure 4.29 shows the experimental Z-distributions corrected for detector acceptance from central collisions of ^{40}Ar + ^{45}Sc at beam energies from 15 to 115 MeV/nucleon (solid circle) compared to our percolation calculation (histogram). The dashed curve is the percolation calculation fitted to a power law distribution, $\sigma(Z) \propto Z^{-\lambda}$. The percolation results are normalized to the experimental data for $3 \leq Z \leq 12$. The apparent exponent of the power law, λ, vs. beam energy is shown in Figure 4.30. The solid circles are the power law fits to the experimental data of ^{40}Ar + ^{45}Sc and the solid histogram is the percolation calculation with 68 sites and a binding energy of 7.8 MeV/nucleon. The open squares are GSI data of Au + C, Al, Cu at 600 MeV/nucleon [Ogil91] and the dotted histogram is the percolation calculation with 150 sites and 7.0 MeV/nucleon binding energy. The equivalent beam energy on the plot for the GSI data is obtained by converting the excitation energy calculated by reference [Ogil91] to a symmetric system assuming a totally inelastic collision. To obtain the critical exponent, τ, we fit the λ vs. E_{beam} with a four term polynomial. For ^{40}Ar + ^{45}Sc we get $\tau = 1.21 \pm 0.01$ at a beam energy of 23.9 ± 0.7 MeV/nucleon. The percolation calculation with 68 sites and a binding energy of 7.8 MeV/nucleon gives $\tau = 1.5 \pm 0.1$ at a beam energy of 28 ± 0.4 MeV/nucleon. For GSI data of Au + C, Al, Cu we get $\tau = 2.0 \pm 0.01$ at a beam energy of 29 ± 0.2 MeV/nucleon. The percolation calculation with 150 sites and a binding energy of 7.0 MeV/nucleon gives $\tau = 1.98 \pm 0.03$ at a beam energy of 32.7 ± 0.1 MeV/nucleon. All errors are statistical.

4.3.4 Finite Size Effects

Percolation model gives not only a microscopic view on how the system breaks up statistically, but also a link from infinite matter critical properties to finite matter critical properties. If we keep all other input parameters the same but only change

the size of the system from a small lattice to a very large one, then we can estimate the asymptotic limit of the critical behavior.

In order to estimate the finite size effects and to obtain the critical excitation energy for infinite nuclear matter, we performed percolation calculations using a binding energy of 8 MeV/nucleon for different lattice sizes ranging from 50 sites to 800 sites, and for slope parameters T_s ranging from 5 MeV to 19 MeV. The critical excitation energy increases when the lattice size increases. Above 400 sites, the critical value for the slope parameter converges to 13.1 ± 0.6 MeV. This value can be compared with the theoretical calculation of 15.3 MeV given by Ref. [Boal86]. In Figure 4.31 a) we plot the λ parameter vs. slope parameter T_s for different lattice sizes. The solid curves are four term polynomial fits for T_s of 7 MeV to 19 MeV, made in order to extract the critical value. The diamonds are for size 50, squares are for size 100, crosses for size 200 and circles for size 500. For size 800 (not shown in the Figure) the points are almost coincident with size 500, which indicates that the critical value of T_s approaches an asymptotic limit at large size. Also, for 100 sites, we performed calculations for different binding energy to illustrate the sensitivity of the critical point with the binding energy. Figure 4.31 b) shows the calculation for $B = 6$ MeV/nucleon (solid circles) $B = 7$ MeV/nucleon (solid squares) and $B = 8$ MeV/nucleon (solid diamonds). All error bars in the figures are statistical. Figure 4.32 a) shows the critical value of slope parameter $T_c = T_s(\tau)$, extracted from the polynomial fits vs. the size of the lattice. Figure 4.32 b) shows the critical exponent τ as a function of the lattice size. It approaches a limit of 2.3 ± 0.2 at a large size.

In conclusion, the Z-distributions of Ar + Sc have been observed and power law fits show a minimum in the λ parameter, $\tau = 1.21 \pm 0.01$ at a beam energy of 23.9 ± 0.7 MeV/nucleon. The percolation calculation, using binding energy of nuclei and proton kinetic energy slope parameters, reproduced both Ar + Sc and Au + C, Al, Cu. The

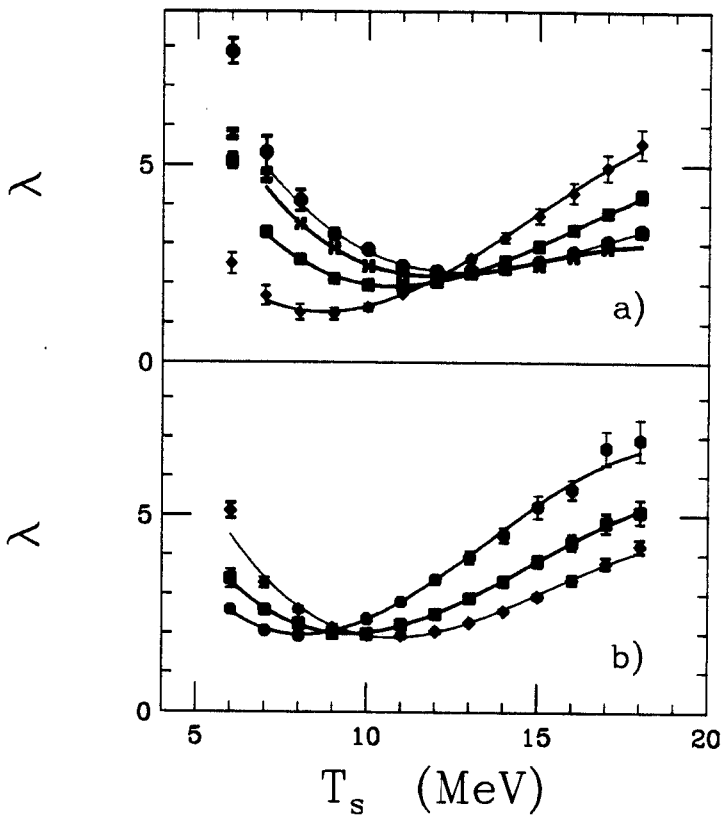

Figure 4.31: a) The apparent exponent of the power law fits, λ, as a function of the slope parameter T_s for different initial lattice size. The solid diamonds are for size 50, the squares are for size 100, the crosses are for size 200 and the solid circles are for size 500. The solid curves are 4 term polynomial fits to the points. b) The power law parameter as a function of T_s with different binding energies. The lattice size is 100 and the binding energies are 6 MeV/nucleon (solid circles), 7 MeV/nucleon (solid squares) and 8 MeV/nucleon (solid diamonds). All error bars are statistical.

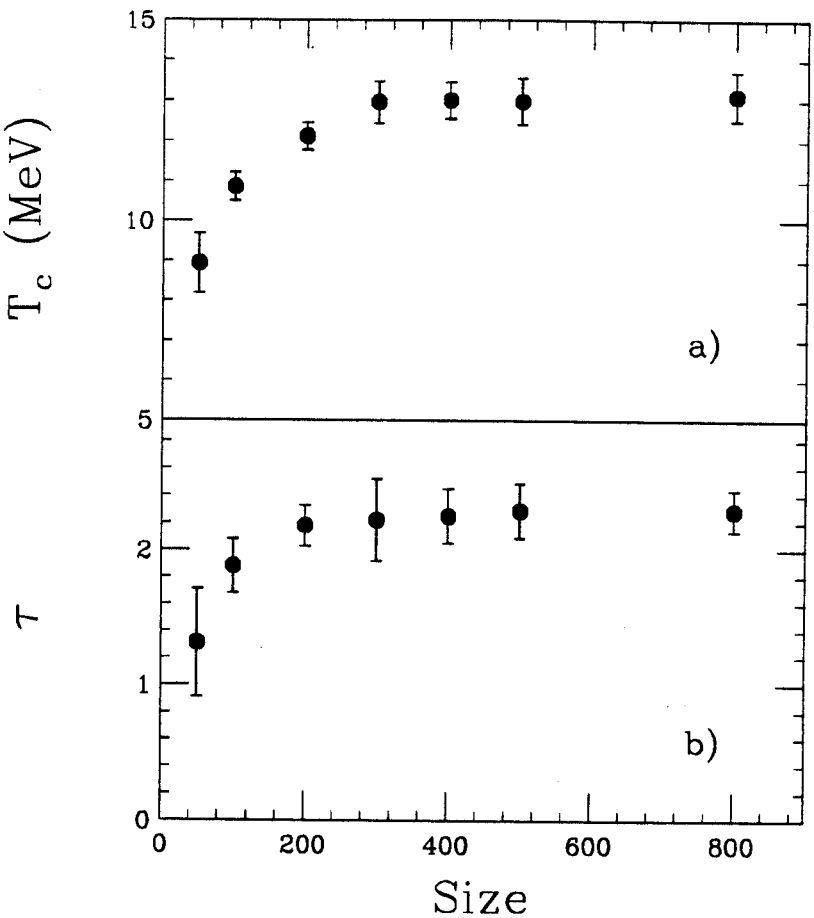

Figure 4.32: The size dependence of the critical value of slope parameter $T_c = T_s(\tau)$ and the critical exponent τ. a) The critical slope parameter T_c with different initial lattice size. b) The critical power law exponent τ as function of initial lattice size.

percolation calculation shows a clear phase transition for different size lattices. The critical temperature for infinite nuclear matter is about 13.1 ± 0.6 MeV for a binding energy of 8 MeV/nucleon.

4.3.5 Finite System Phase Transition

To obtain a global picture of a liquid-gas phase transition for a finite system in the context of the percolation calculation, we generated cluster size distribution for a system with 100 nucleons and a binding energy of 8 MeV/nucleon for temperature below and above the critical point. Figure 4.33 shows that at low temperature the distribution has a peak at size close to 1 and a peak at large size close to $A = 100$ which indicates light particle (the small size peak) evaporated from the compound system, the large peak indicates the evaporation residue of the compound system. The two peaks show the system goes through the mechanical instable region where liquid and gas phase coexist. While at high temperature, $T = 13$ MeV for example, only low A peak exists which indicates that only gaseous phase exists. At the critical temperature where the high A peak merged into the low A peak, the fragments size distribution is the flattest with a minimum of apparent exponent, λ, for a power law fit.

Imagine if we increase the size of the system to infinity, then at low temperature the high A would be peaked at infinity which means a liquid surface. At high temperature only gaseous phase, the liquid droplets and gas exists. At the critical temperature, the liquid surface – the infinite cluster disappears. For infinite matter, the critical phenomena shows a sudden change, the liquid surface evaporated at a certain point, while for finite matter, the liquid residue merge into gaseous phase gradually which cause a flat cluster size distribution. The finite size of the system does reduce the sudden change of phases, but the critical behavior can still be observed.

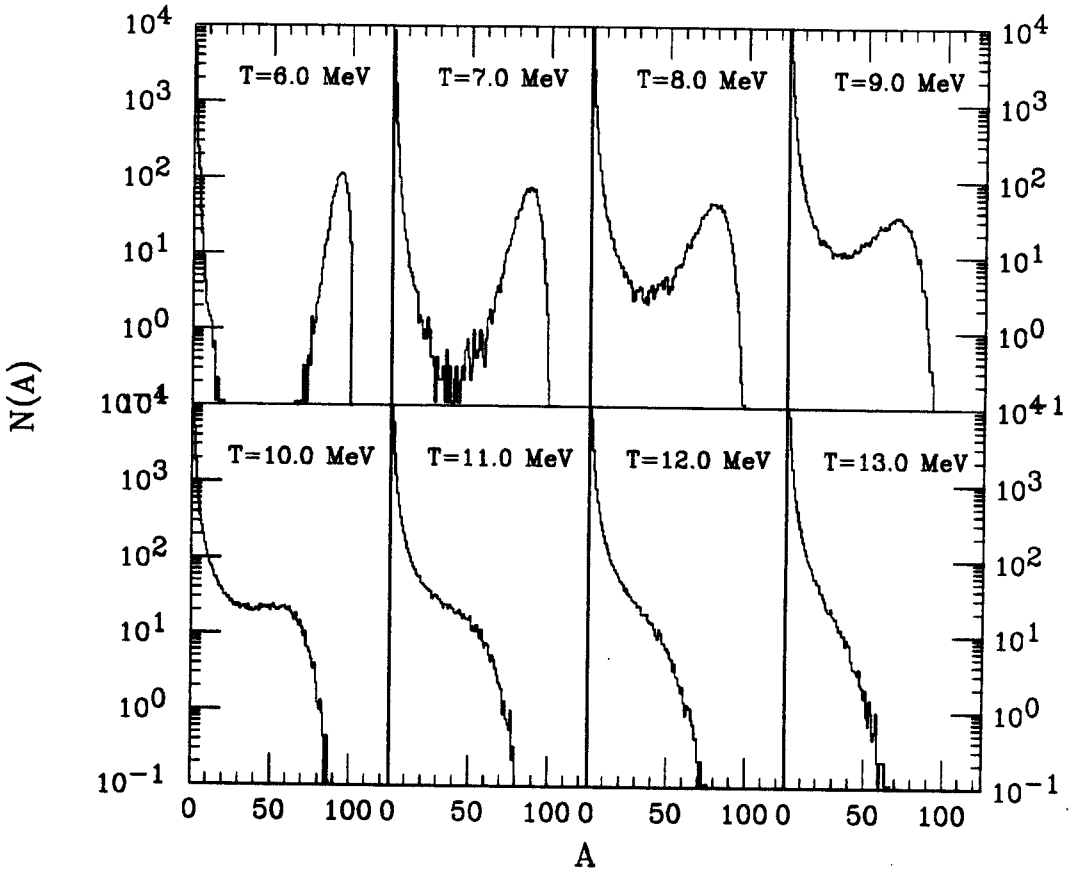

Figure 4.33: Percolation calculation for a system of 100 nucleons with a binding energy of 8 MeV/nucleon.

4.4 Summary

The experimental Z-distributions of central collisions of Ar+Sc corrected for detector acceptance have been fitted to both power law and exponential function. A minimum of power law parameter λ at 23.1±0.4 MeV/nucleon beam energy is observed. At the minimum, the power law fitting has a smaller χ^2 per degree of freedom, and away from the minimum the exponential χ^2 is smaller.

A new assumption for the percolation calculation linking the bond breaking probability to system temperature by Boltzmann distribution leads to successful explanations of both the minimum of λ and the critical temperature for Ar + Sc and Au + C, Al, Cu. The finite size effect has also been studied and an asymptotic limit of the critical temperature is observed at about 13.1±0.6 MeV with a binding energy of 8 MeV per nucleon. If we assume that for the infinite nuclear matter, the phase transition can be described by both microscopic percolation model and the macroscopic thermodynamical EOS, then the asymptotic critical point can by used to calibrate the nuclear equation of state.

Chapter 5

Dynamics: Transverse Flow and Disappearance of Flow

5.1 Introduction

Studies of heavy ion reaction in phase space showed strong dynamical phenomena as collective motion. Event shape analysis in phase space for heavy ion reactions at several hundred MeV/nucleon exhibited rotational motion, transverse flow and squeeze out motion [Ritt85, Gutb89a, Gutb89b]. These modes of collective motion are the result of the interactions inside the reaction zone. Therefore, they can provide information about the dynamical aspects of heavy ion reaction.

Because of the short time scale of the reaction (10^{-22} to 10^{-23} seconds), strong dynamical properties will appear in the final state if the statistical thermal motion and uncertainties of the measurement are not strong enough to wash out the dynamical effects. Experimental data of heavy ion reactions at intermediate energies do exhibit unambiguous dynamical properties, such as transverse flow [Ogil89a, Ogil89c, Krof92, Krof91, Krof89, Ogil90, Zhan90, Sull92, Beav92, Herr93], azimuthal distributions[Wils90, Ma93] and azimuthal correlations[Lace93]. Dynamical observations are means of probing the interactions during the collision. For heavy ion reactions, through dynamical observations, a better knowledge of mean field inside

the reaction region may be obtained using dynamical model such as BUU (Boltzmann-Uehling-Uhlenbeck) calculation [Moli85, Bert87, Bert88, Dani88].

It is believed that there are two major interactions dominating the nuclear reaction in intermediate energy region, the attractive nuclear mean field and the repulsive nucleon-nucleon (n-n) interaction. The nuclear mean field is directly linked with the nuclear EOS [Bert88]. Thus, studies of the dynamics of heavy ion reactions mainly concentrate on a better understanding of the EOS of nuclear matter which plays a major role in explaining some astronomical observations such as supernova and neutron stars.

The first step of a dynamical study is the flow tensor analysis discussed in Chapter 3. The phase space shape analysis indicates that some transverse properties can be observed such as flow or flow angle, which is the angle of the major eigen vector corresponding to the largest eigen value with respect to the beam axis [Ritt85, Gutb89a, Cugn82, Cugn85] in center of momentum frame. Early dynamical theories such as hydrodynamical and intranuclear cascade calculation predict different event shape in phase space. Hydrodynamical study predicts that a flow angle of 90 degrees will occur for zero impact parameter and 0 degree flow angle – prolate shaped event along beam axis would be observed for grazing collisions and it is independent of projectile and target combination. Because cascade calculations predict small flow angles for all impact parameters, the different predictions strongly promoted the search of experimental evidences.

The finite event multiplicities in heavy ion reactions cause difficulties in the event shape analysis because of fluctuation in calculating the momentum tensor. Later studies then focused on transverse momentum analysis. The transverse flow is the sideward deflection of the reaction products in phase space [Dani85, Doss86, Doss87, Ogil89a, Ogil90, Krof89, Krof91, Krof92, Beav92]. The most well studied parameter

of the EOS is the nuclear compressibility, K which is defined as:[Bert88]

$$K = \frac{9k}{\rho} = 9(\frac{\partial P}{\partial \rho})$$

where P is the pressure and ρ is the nuclear number density and $k = \rho(\partial P)/(\partial \rho)$. It represents the "hardness" of nuclear matter against compression. Since we do not have the luxury of directly measuring the nuclear EOS as we can for classical EOS of ordinary matter, the mapping of different observations to constrain the nuclear EOS becomes essential.

In this chapter we introduce the concept of how the dynamical calculations can be compared with experiments and provide information on the nuclear compressibility. First, we look at the flow and the disappearance of flow in intermediate energy region. Then we compare the experimental results to the BUU calculations, which is the most commonly used theory in the flow experiments. Finally, we discuss how the experimental results can provide information on EOS of nuclear matter.

5.2 Flow and Disappearance of Flow

5.2.1 Transverse Flow

The transverse flow analysis is done in the reaction frame (see chapter 1.2.3) which is a rotation of the P_X axis of the center of momentum frame to the direction of the projectile side of the reaction plane. The phase space shape can be expressed in terms of a phase space flow tensor $F_{i,j}$. The flow tensor can be diagonalized with three eigen values and eigen vectors. The three eigen vectors give three major axis. The event shape in phase space also can be projected on the reaction plane which produces an ellipsoid in the $P_X - P_Z$ plane shown as Figure 5.3 top frames. For simplicity, the phase space shape (distribution) can be expressed in terms of the average in-plane transverse momentum for different rapidity bins shown in the figure 5.3 bottom

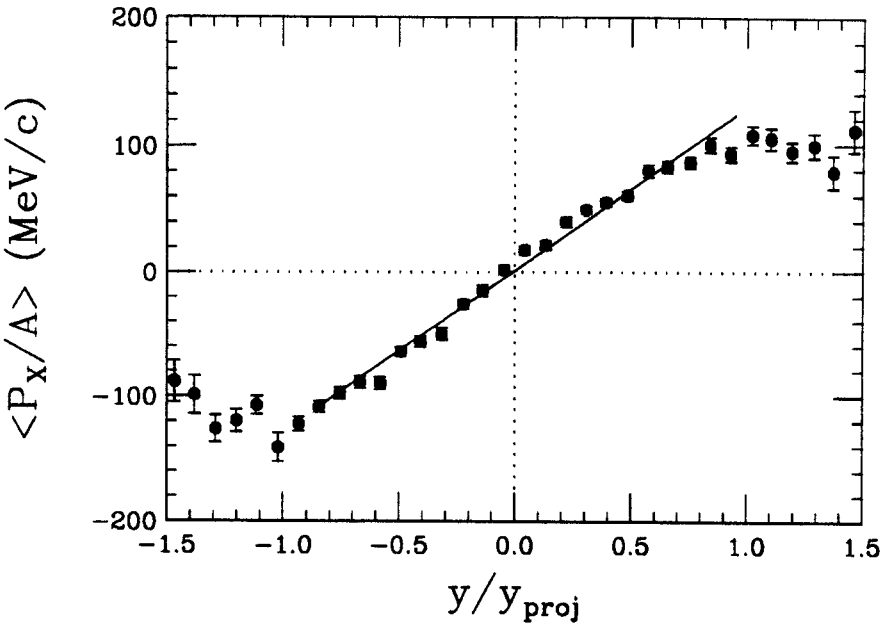

Figure 5.1: Transverse flow of Nb + Nb at 400 MeV/nucleon (from reference [gutb89a]).

frames. The slope of the average transverse momentum $\langle P_X \rangle$ vs. rapidity y is called flow.

The transverse flow is due to the interactions inside the reaction zone. Early Plastic ball experiments showed the strong transverse flow. Figure 5.1 shows the transverse flow for Nb + Nb at 400 MeV/nucleon[Gutb89a]. The rapidity y normalized by the projectile rapidity y_{proj} and the average transverse momentum per nucleon is projected to the reaction plane as $\langle P_X/A \rangle$.

The absolute value of the in-plane transverse momentum is strongly affected by the accuracy of reaction plane determination and the detector acceptance. The projection of the transverse momentum on the reaction plane is $P_x = P_t cos\phi$ where ϕ is the

angle between transverse momentum and projectile side of reaction plane. The error in determining ϕ can reduce the value of P_x. Also, the detector acceptance can affect both the accuracy of determining the reaction plane and the transverse momentum itself. In chapter 3.2 we discussed the width of the determined reaction plane with respect to the real reaction plane is significantly large. The value of P_x has to be corrected if direct comparison of data and BUU are made.

However, no reaction plane corrections are applied to present data. At low beam energies, the transverse flow is dominated by an attractive interaction and the flow is expected to be negative. At high beam energies, the flow is dominated by n-n repulsive interaction and the flow is expected to be positive. At a given beam energy, the attractive interaction and repulsive interaction are balanced which causes a zero flow. The balance energy is independent of the accuracy of reaction plane determination and do not require correction for comparison with BUU.

5.2.2 Disappearance of Flow and Balance Energy

There is a long range attractive potential inside the nuclear reaction zone called the mean field. The mean field is often expressed in terms of the nuclear density:

$$U(\rho/\rho_0) = A(\rho/\rho_0) + B(\rho/\rho_0)^\sigma, \tag{5.1}$$

where ρ is the nucleon number density, ρ_0 is the saturation density and A, B, σ are constants which can be determined by the ground state binding energy[Bert88]. Figure 5.2 shows two different parameterization. The solid curve is for a stiff EOS with A=-124 MeV, B=70.5 MeV, $\sigma = 2$ which give a nuclear compressibility $K = 380$ and the dotted curve is for a soft EOS with A=-356 MeV, B=303 MeV, $\sigma = 7/6$ which gives a nuclear compressibility $K = 210$.

In short range, there is n-n hard core repulsive interaction. The free space n-n

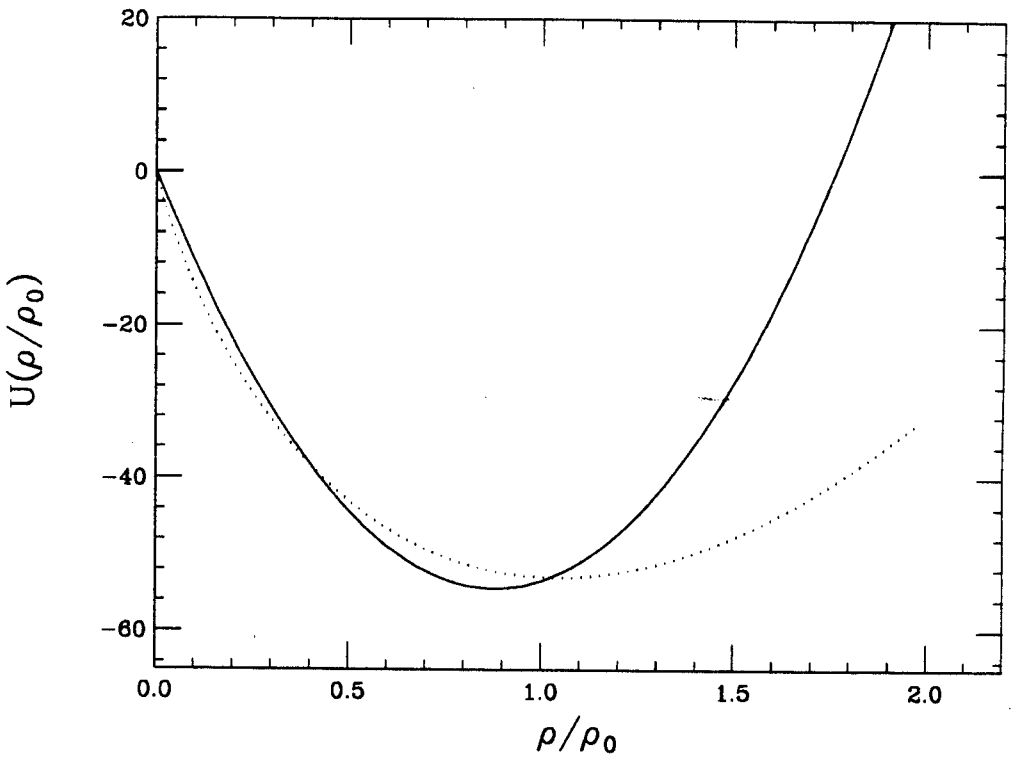

Figure 5.2: Mean field constructed from a Skrym type of interaction as a function of nucleon number density. The solid curve is for a stiff EOS with K=380 MeV and doted curve is for soft EOS with K=240 MeV

cross section is well known and it is a function of the n-n center of momentum energy [Bert88]. At low beam energy the de Broglie wavelength of a projectile nucleon is greater than the distance between target nucleons so a projectile nucleon will interact with target nucleons mainly through the mean field, which is an attractive interaction. This interaction produces a negative deflection of the particles after the collision. This negative deflection gives a negative flow angle as shown in Figure 5.3 right frames as attractive flow. At high beam energies, the de Broglie wavelength is smaller than the distance between target nucleons, the n-n collision – a hard core repulsive interaction will dominate, which leads to a positive flow angle shown in Figure 5.3 left frames as repulsive flow.

At the beam energy where the repulsive interaction balances the attractive interaction, the transverse flow disappears. The beam energy at which the transverse flow disappears is called the balance energy, $E_{balance}$ [Krof92, Krof91, Fan92, West90a, West90b, West92, West93]. The balance energy is an observable which can be directly measured and compared with dynamical calculations such as BUU.

The effect of the detector acceptance and the accuracy of determination of reaction plane may affect the observed value of the transverse flow. The effect of both detector acceptance and accuracy of determination of reaction plane have to be corrected, if one compares the observed value of transverse flow to theoretical calculations. Because flow disappears at the balance energy, the observed zero flow will not be affected by the accuracy of determination of reaction plane and detector acceptance.

The first observation of the disappearance of flow was reported by Krofcheck et. al. for the system of ^{139}La+^{139}La at beam energies of 50, 70, 130 MeV per nucleon. The in-plane transverse momenta per nucleon were analyzed for proton, deuteron, triton and helium fragments. The flow was defined as the average in plane transverse momentum per nucleon for the projectile rapidity [Krof89]. Zero flow was

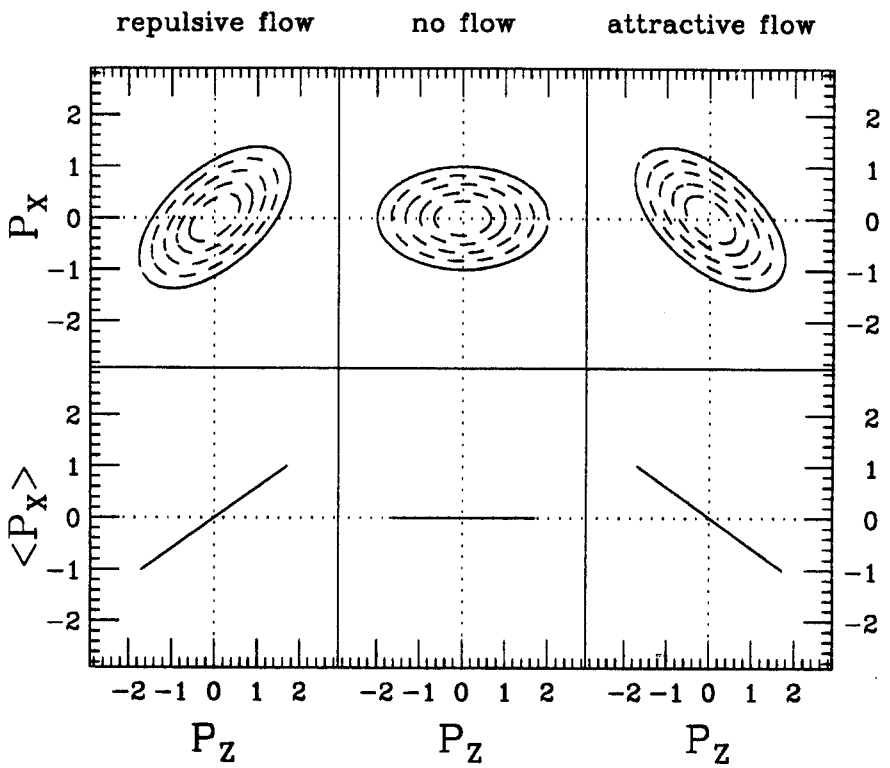

Figure 5.3: Transverse flow in phase space. Top frames are the phase space shape of a heavy ion reaction in reaction frame. Bottom frames are the average P_X for each P_Z bin.

found near 50 MeV/nucleon beam energy. Ogilvie et. al. observed the balance energy for ^{40}Ar + ^{51}V at $E_{balance} \geq 76$ MeV/nucleon using the reaction of ^{40}Ar + ^{51}V at 35 to 85 MeV/nucleon [Ogil90]. Later a measurement for ^{40}Ar + ^{51}V at 100 MeV/nucleon was done which gave the balance energy as $E_{balance} = 85 \pm 10$ MeV/nucleon [Krof91, West90a, West90b]. Collisions of Au + Au at 75, 150, 250, 400 and 600 MeV/nucleon were studied by Zhang et. al.. For central collisions of Au + Au, the balance energy was measured to be $E_{balance} \leq 60$ MeV/nucleon [Zhan90]. Sullivan et. al. also reported the balance energy for Ar + Al reactions in the range of 70 to 80 MeV/nucleon for central collisions [Sull90].

5.3 Experimental Result of Ar + Sc

For the Ar + Sc system the initial conditions is determined by the method discussed in Chapter 3. The reaction plane is determined by the azimuthal correlation method. Only central events ($b \leq 0.25 b_{max}$) are studied. Transverse flow is shown by plotting the average in-plane transverse momentum normalized by the total transverse momentum, $\langle P_x/P_t \rangle$ vs. center of momentum rapidity normalized by projectile rapidity.

Figure 5.4 to 5.8 shows $\langle P_x/P_t \rangle$ for proton, deuteron, triton, helium, and lithium for beam energy of 35, 45, 65, 75, 85, 95, 105 and 115 MeV/nucleon. The average transverse momenta projected on the reaction plane show a slope in the mid-rapidity region. The reduced flow F_r is defined as the slope of $\langle P_x/P_t \rangle$ vs. rapidity y at $y = 0$. where y is the center of mass rapidity.

$$F_r = \left(\frac{d\langle P_x/P_t \rangle}{dy}\right)_{y=0}. \tag{5.2}$$

To obtain the reduced flow, we fit the $\langle P_x/P_t \rangle$ vs. y with a straight line from $y = -0.1$ to $y = 0.1$ and the slope of the straight line is used as the reduced flow F_r.

Reduced flow can be observed for both low beam energy and high beam energy.

At an intermediate beam energy the $\langle P_x/P_t \rangle$ vs. y is flat. The positive reduced flow for the low beam energy is due to the definition of P_x as the projection of transverse momentum on the projectile side of the reaction plane.

Figure 5.9 shows the reduced flow as a function of beam energy. From top to bottom frame, proton, deuteron, triton, helium and lithium reduced flow are shown. The dashed curve is a polynomial fit to obtain the balance energy. For all fragments, the reduced flow has a minimum at 85 MeV/nucleon. The offset at the minimum from zero is due to the inaccuracy of determining the reaction plane when the flow disappeared. From the above observation, we obtain $E_{balance}$. For Ar + Sc, we find that $E_{balance} = 87 \pm 12$ [West93]. The error is determined by fitting the polynomial function in different range. This balance energy can be used to constrain theoretical calculation in order to gain knowledge of EOS of nuclear matter. Figure 5.10 shows the reduced flow as a function of beam energy for Z=4,5,6,7. The balance energies of Z=4,5,6,7 are the same as low Z particles which indicate that the disappearance of flow is independent of particle charge number.

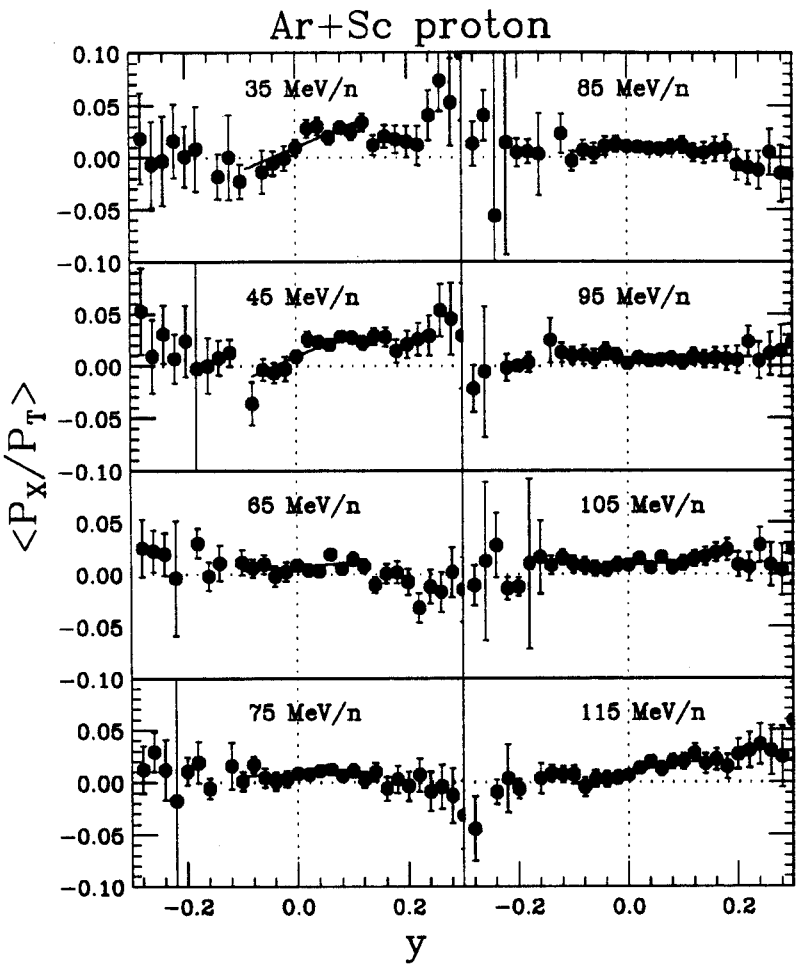

Figure 5.4: Proton transverse flow of Ar + Sc at beam energy of 35 to 115 MeV/nucleon. The straight line is a linear fit to the data from y from -0.1 to 0.1.

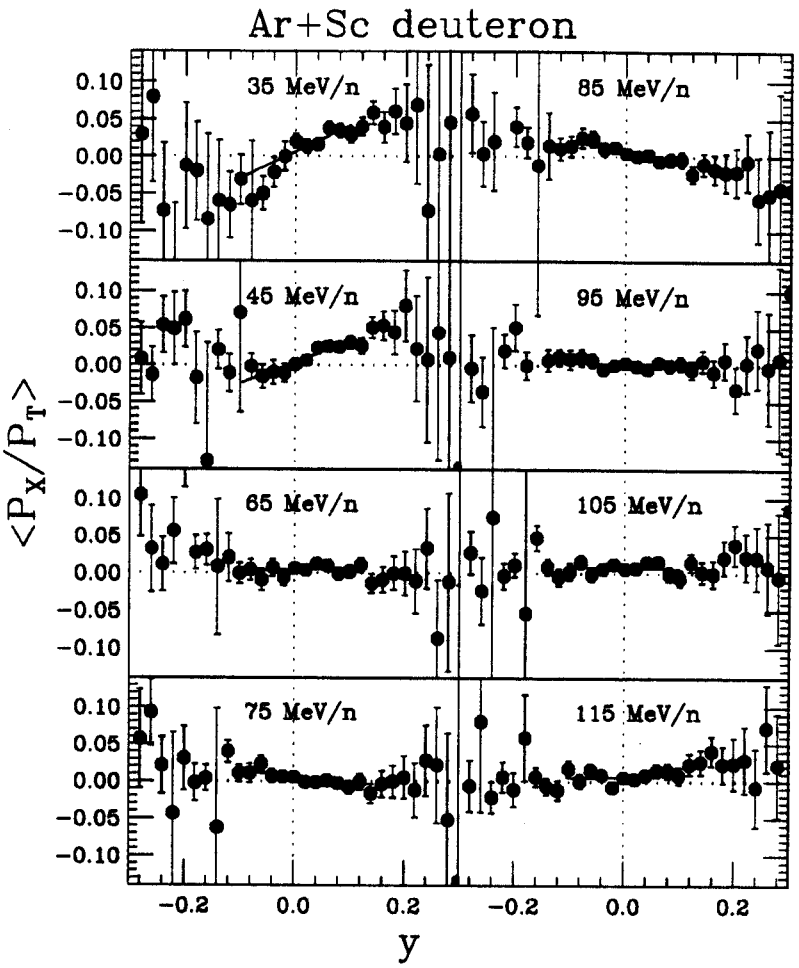

Figure 5.5: Deuteron transverse flow of Ar + Sc at beam energy of 35 to 115 MeV/nucleon. The straight line is a linear fit to the data from y from -0.1 to 0.1

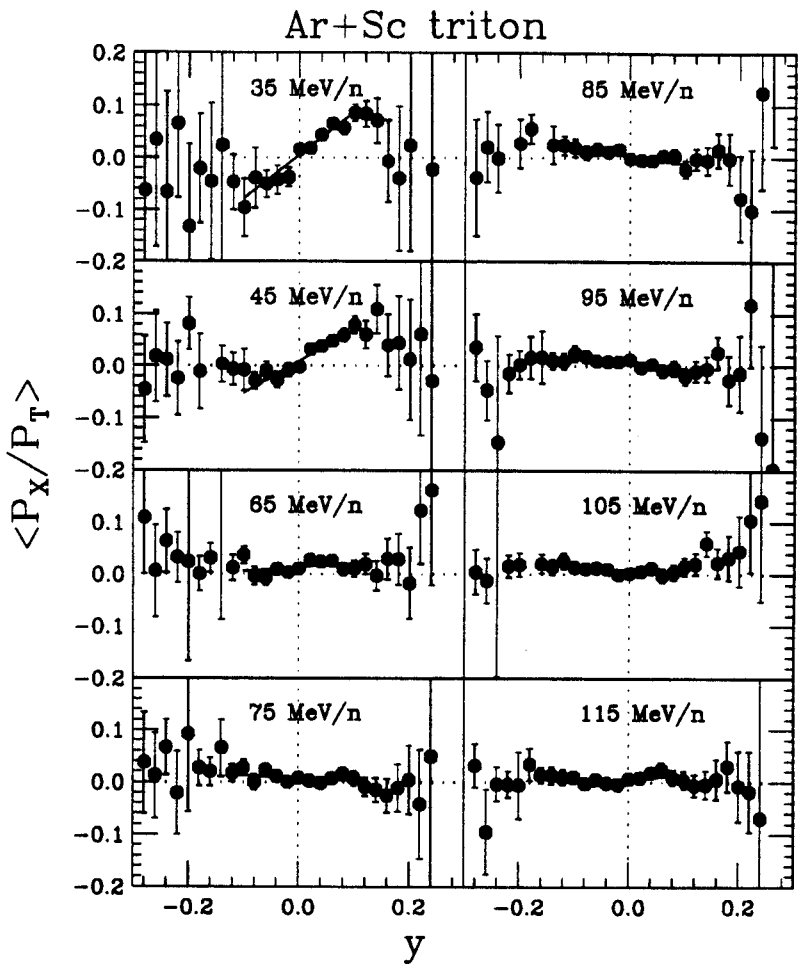

Figure 5.6: Triton transverse flow of Ar + Sc at beam energy of 35 to 115 MeV/nucleon. The straight line is a linear fit to the data from y from -0.1 to 0.1

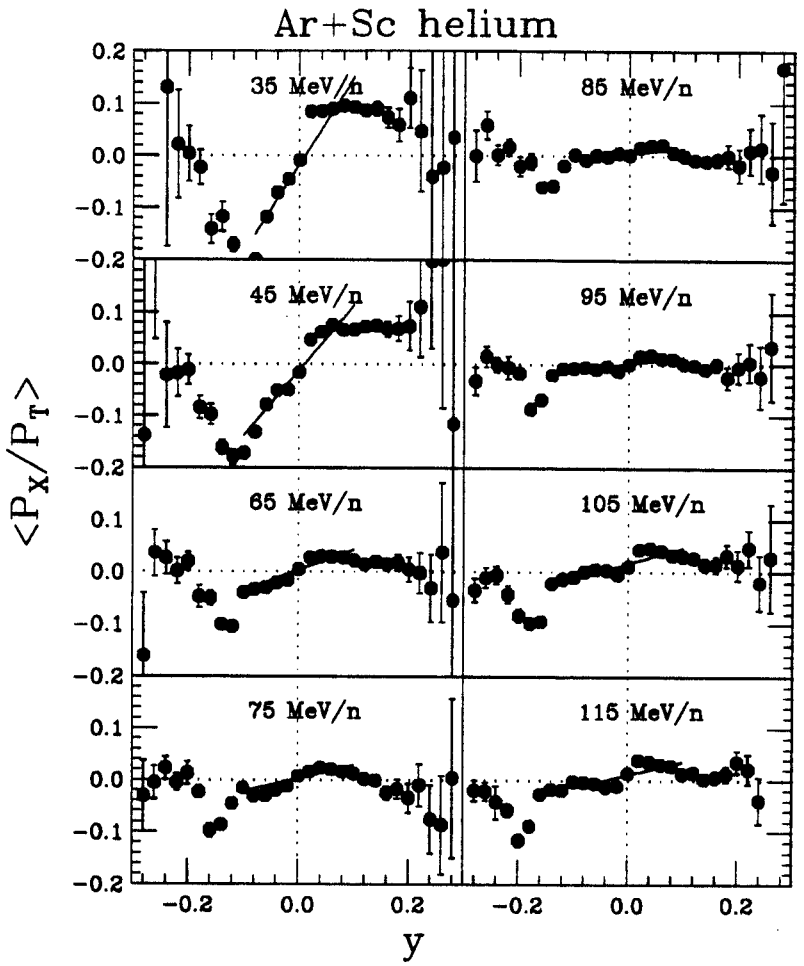

Figure 5.7: Helium transverse flow of Ar + Sc at beam energy of 35 to 115 MeV/nucleon. The straight line is a linear fit to the data from y from -0.1 to 0.1

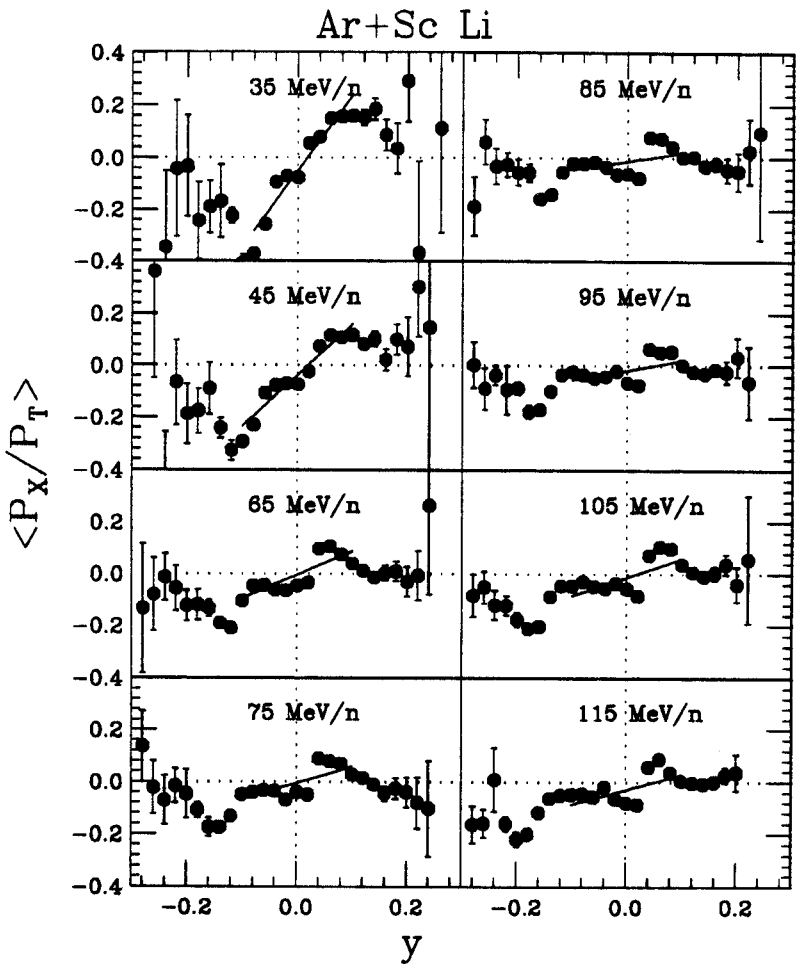

Figure 5.8: Lithium transverse flow of Ar + Sc at beam energy of 35 to 115 MeV/nucleon. The straight line is a linear fit to the data from y from -0.1 to 0.1

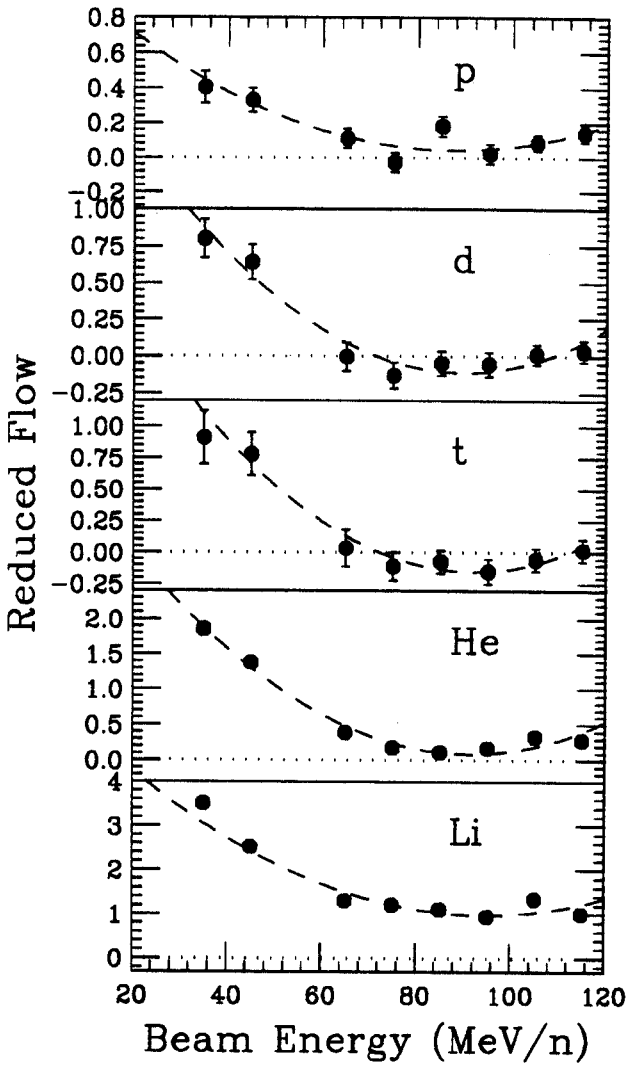

Figure 5.9: Reduced flow for p, d, t, He, Li. The dashed curves are third order polynomial fits to the data points to obtain the minimum, i.e. balance energies.

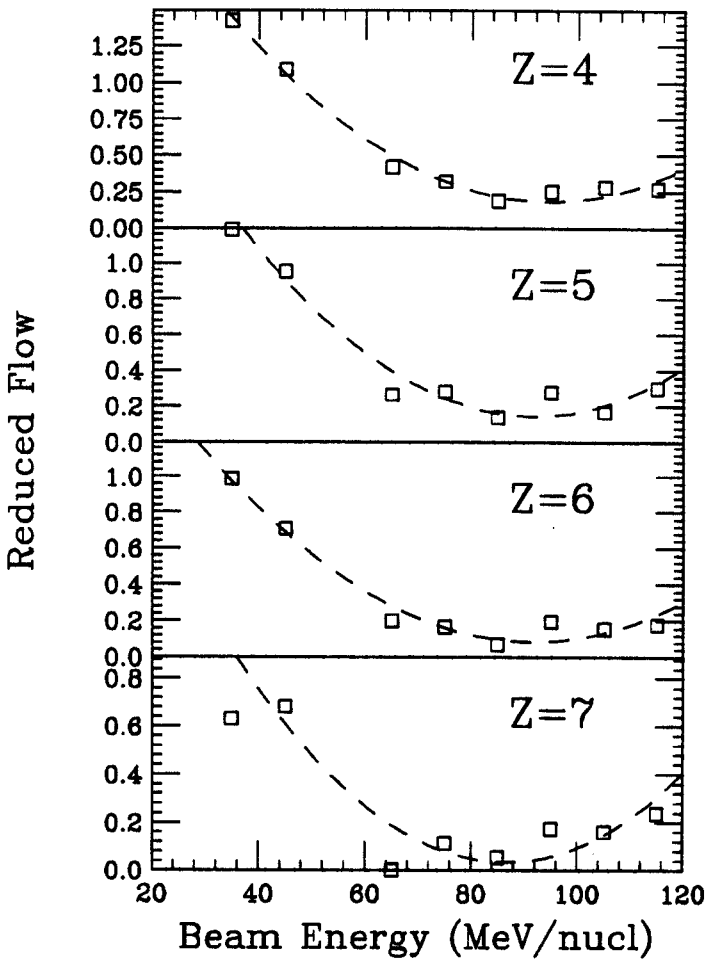

Figure 5.10: Reduced flow for Z=4,5,6,7. The dashed curves are third order polynomial fits to the data points to obtain the minimum, i.e. balance energies.

5.4 BUU Calculation and Nuclear Compressibility

The BUU (Boltzmann-Uehling-Uhlenbeck) transport equations contain mean field, n-n collision and Pauli blocking [Bert84, Bert88, Ma93]. The transport is governed by the equation:

$$\frac{\partial f}{\partial t} + \mathbf{v}\cdot\nabla_{\mathbf{r}} f - \nabla_{\mathbf{r}} U\cdot\nabla_{\mathbf{p}} f = -\frac{1}{(2\pi)^6}\int d^3p_2 d^3p_{2'} d\Omega \frac{d\sigma}{d\Omega} v_{12} \times\{[ff_2(1-f_{1'})(1-f_{2'}) - f_{1'}f_{2'}(1-f)(1-f_2)] \times(2\pi)^3\delta^3(\mathbf{p_1}+\mathbf{p_2}-\mathbf{p_{1'}}-\mathbf{p_{2'}})\}, \quad (5.3)$$

where $f = f(p,r)$ is the single particle distribution function and U is the mean field (see equation 5.1) and $\mathbf{v}$ is the velocity of the particle. Right hand side of the equation is the collision integral which includes Pauli-blocking factor $(1-f)(1-f)$. Before the collision nucleons have momenta $\mathbf{p_1}$ and $\mathbf{p_2}$ and after collision the momenta of the two nucleons change to $\mathbf{p_{1'}}$ and $\mathbf{p_{2'}}$. v_{12} is the relative velocity of the two nucleons and $\frac{d\sigma}{d\Omega}$ is the n-n cross section. The numerical solution of Equation 5.3 is described in reference [Bert88]. The mean field potential used in BUU calculation is in the form of equation 5.1.

The major ingredients for BUU calculation are the repulsive n-n collisions and the mean field interaction. The n-n repulsive interaction is represented by hard cord collisions with a in-medium n-n cross section, $\sigma_{nn} = (d\sigma/d\Omega)$, as an input parameter. The mean field is parameterized with three constants, A, B, σ which are linked with nuclear compressibility by:

$$K = 9(\frac{p_F^2}{3m} + A + \sigma B), \quad (5.4)$$

where p_F is fermi momentum and m is nucleon mass [Bert88]. The dynamics in BUU is a competition between mean field attraction and n-n repulsion. Therefore BUU

gives a balance beam energy for a projectile, P, colliding with a target, T, with an impact parameter, b, if the nuclear compressibility and in-medium n-n cross section, σ_{nn}, are given, i.e.

$$E_{balance}^{BUU} = E_{balance}^{BUU}(P, T, b, K, \sigma_{nn}), \tag{5.5}$$

where $E_{balance}^{BUU}$ is the balance energy calculated by BUU. The experimental result of $E_{balance}^{exp}(b, P, T)$ may provide a constraint on the two parameters, K and σ_{nn}.

The BUU calculations are strongly dependent on the in-medium n-n cross section and weakly dependent on the nuclear compressibility K. Figure 5.11 shows a calculation of balance energy for ^{45}Ar + ^{51}V for different values of K and σ_{nn} [Ogil90]. Figure 5.11 a) shows K vs. $E_{balance}^{BUU}$ with $\sigma_{nn} = \sigma_{free}$ where σ_{free} is the free n-n cross section. A dramatic change of K from 200 MeV to 380 MeV only changes the $E_{balance}^{BUU}$ by about 8 MeV/nucleon which is smaller than the experimental error. Figure 5.11 b) shows in-medium n-n cross section vs. $E_{balance}^{BUU}$ with a fixed K = 200 MeV. A dramatic change of $E_{balance}^{BUU}$, 40 MeV/nucleon, when changing σ_{nn} from 100% of σ_{free} to 70% of σ_{free}.

The insensitivity of $E_{balance}$ to the nuclear compressibility makes the determination of nuclear compressibility impossible with a single experimental point. In order to achieve the goal of finding both K and σ_{nn}, a systematic study of different reaction systems and different impact parameters are needed.

5.5 Conclusion

The competition of mean field attraction and n-n repulsion in heavy ion reactions provides an observable, i.e. balance energy, where the transverse flow disappears. The balance energy as a function of projectile, target and impact parameter can be observed experimentally without significant influence by either detector acceptance

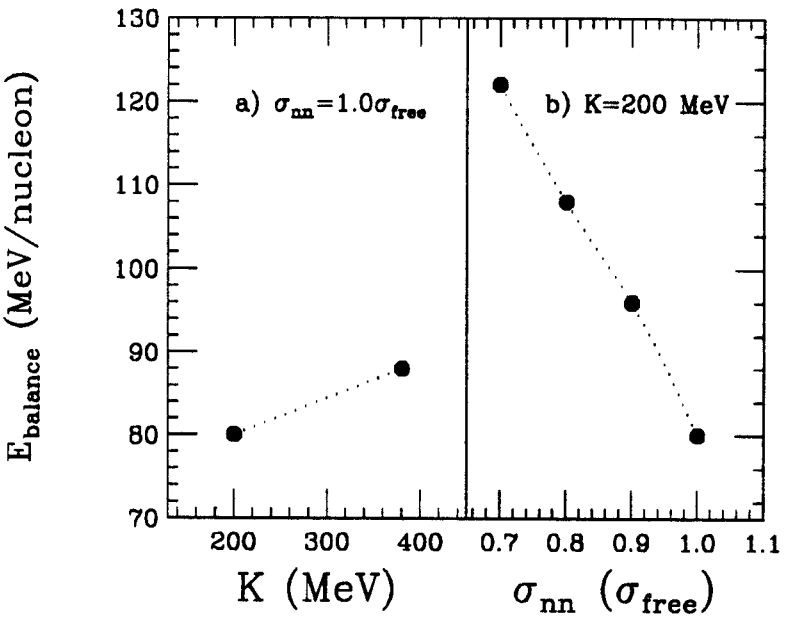

Figure 5.11: The sensitivity of balance energy with the nuclear compressibility, K, and in-medium n-n cross section, σ_{nn}. a) K vs. balance energy for $\sigma_{nn} = 1.0\sigma free$. b) σ_{nn} vs. balance energy for $K = 200$ MeV.

or the error of determination of reaction plane. The experimentally measured balance energy can be used to compare directly with theoretical calculation, which involves the dynamics of mean field attraction and n-n hard core collisions.

For $^{40}Ar + ^{45}Sc$, the transverse flow was observed and a balance energy of 87 ± 12 MeV/nucleon was obtained by fitting the reduced flow defined as $d(\langle P_X/P_T \rangle)/dy$ at y/y_proj from -0.1 to 0.1 to a third order polynomial.

The BUU calculation of the balance energy is sensitive to the in-medium n-n collision cross section, but is less sensitive to the nuclear matter compressibility. The single measurement of the balance energy for one reaction system with one impact parameter can not provide limits on both K and σ_{nn}. To fix both free parameters in BUU calculations, the mass dependence of balance energy or the impact parameter dependence of balance energy must be measured.

Chapter 6

Conclusion

To study the dynamical and statistical properties of intermediate energy heavy ion reactions in order to gain knowledge of thermodynamical properties of bulk nuclear matter, central collisions of a nearly symmetric reaction system, $^{40}Ar + ^{45}Sc$, from 15 to 115 MeV/nucleon, were studied using the MSU 4π Array. The MSU 4π Array phase II configuration consists of 30 low-energy-threshold high-charge-resolution Bragg Curve Counters backed up by 170 high dynamic range fast/slow plastic phoswich detectors. 45 plastic phoswich detectors cover the forward direction. The newly finished BCCs allow the measurement of high Z particles with low kinetic energy.

Initial Condition Determination

The MSU 4π Array allows us to estimate the initial conditions such as reaction plane and impact parameter. Using the azimuthal correlation method, the reaction plane determination is more accurate than the transverse momentum method previously used in high energy heavy ion reactions. The impact parameter determination has been done though an analytic method. It gives a relation of impact parameter and a global observable, which is assumed to vary monotonically with the impact parameter. The observed distribution function of the global observable, folded into the geometrical entrance channel cross section, gives the impact parameter as a function

of the global observable. The central collisions are then selected by a combined global observable which gives a common centrality cut for both dynamical and statistical studies with minimal gating distortion. Central collisions with impact parameter b from 0 to 0.25 b_{max} are studied.

Statistical Result – Critical Behavior of IMF Production:

According to both Fisher's droplet model and bond percolation model, cluster distributions behave as a power law at the critical point. Around the critical point, the cluster distribution can be fitted by a power law with an apparent exponent, λ. At the critical point the λ reaches a minimum. Away from the critical point, the cluster size distribution is better described by an exponential function.

The observed Z-distributions has been corrected for detector acceptance. The corrected Z-distributions are fitted by both a power law and an exponential function. Fitting the power law parameter, λ, vs. beam energies with a four term polynomial we get a minimum of the apparent exponent, $\tau = 1.21 \pm 0.01$, at a beam energy of 23.9 ± 0.7 MeV/nucleon for Ar + Sc, and $\tau = 2.0 \pm 0.01$ at (equivalent) beam energy of 29 ± 0.2 MeV/nucleon for Au + C, Al, Cu [Ogil91]. Also, at the critical point, the power law fit has a smaller χ^2 per degree of freedom than exponential fit. At higher energy the χ^2 of the power law fit are much larger than the exponential fit. The excitation energy of the central collisions has been estimated through proton kinetic energy slope parameters.

A bond percolation calculation has been carried out assuming the bond breaking probability is associated with the binding energy and the temperature of the system by an integration of a Boltzmann distribution. Performing percolation calculation with a system of 68 nucleons (calculated by fireball model with $b = 0.25 b_{max}$) and a binding energy of 7.8 MeV/nucleon, we get a minimum apparent exponent, $\tau = 1.5 \pm 0.1$, at

a beam energy of 28 ± 0.4 MeV/nucleon. For Au + C, Al, Cu, we used a system of 150 nucleon with a binding energy of 7.0 MeV/nucleon. We get $\tau = 1.98 \pm 0.03$ at a beam energy of 32.7 ± 0.1 MeV/nucleon.

The percolation calculation shows the system mass dependence of the critical behavior. To obtain the asymptotic limit of the critical behavior and to understand the finite size effects, we performed the percolation calculation for system size of 50, 100, 200, 300, 400, 500 and 800 with a binding energy of 8 MeV/nucleon. The asymptotic limit of the critical temperature reaches 13.1 ± 0.6 MeV at size 800 and τ reaches 2.3 ± 0.2.

Dynamical Observation: Flow and Disappearance of Flow:

The transverse flow collective motion, and the disappearance of flow due to the balanced interaction of nucleon-nucleon repulsive interaction and mean field attractive interaction, have been studied for Ar + Sc system. A balance energy of 87 ± 12 MeV/nucleon has been observed.

The BUU calculations show sensitivity of the balance energy to the in-medium n-n cross section and weak sensitivity to the mean field parameters. In order to provide more complete constraint on the input parameters of BUU calculations, more systems with different mass have to be studied. The impact parameter dependence of the balance energy also must be investigated to determine the nuclear compressibility.

Bibliography

[Abra79] F. F. Abraham, Phys. Rep. **53**, 95 (1979).

[Asse82] J. M. Asselineau, J. Duchon, M. L'Haridon, P. Mosrin, R. Regimbart, and B. Tamain, Nucl. Instr. Meth. **204**, 109 (1982).

[Awes81] T. C. Awes, G. Poggi, S. Saini, C. K. Gelbke, R. Legrain, and G. D. Westfall, Phys. Lett. **103B**, 417 (1981).

[Awes82] T. C. Awes, S. Saini, G. Poggi, C. K. Gelbke, D. Cha, R. Legrain and G. D. Westfall, Phys. Rev. C **25**, 2361 (1982).

[Baro85] E. Baron, J. Cooperstein, and S. Kahana, Phys. Rew. Lett. **55**, 126 (1985).

[Baro87] E. Baron, H. A. Bethe, G.E. Brown, J. Cooperstein, and S. Kahana, Phys. Rew. Lett. **59**, 736 (1987)

[Barz86] H. W. Barz, J. P. Bondorf, R. Donangelo, and H. Schulz, Phys. Lett. **B169**, 318 (1986).

[Baue85] W. Bauer, D. R. Dean, U. Mosel, and U. Post, Phys. Lett. **150B** 53 (1985).

[Baue86] W. Bauer, U. Post, D. R. Dean, and U. Mosel, Nucl. Phys. **A 452**, 699 (1986).

[Baue87] W. Bauer, G. F. Bertsch, and S. Das Gupta, Phys. Rev. Lett. **58**, 863 (1987).

[Baue88] W. Bauer, Phys. Rev. C **38**, 1297 (1988).

[Baue92] W. Bauer, Nucl. Phys. **A545**, 369 (1992).

[Baue93] W. Bauer, Prog. Part. Nucl. Phys. **30**, 45 (1993).

[Bert84] G. F. Bertsch, H. Kruse, and S. Das Gupta, Phys. Rev. C **29**, 673 (1984).

[Bert87] G. F. Bertsch, W. G. Lynch, and M. B. Tsang, Phys. Lett. **189B**, 384 (1987).

[Beav92] D. Beavis, R. Bock, R. Brockmann, P. Danielewicz, S. Y. Fung, J. W. Harris, D. Keane, Y. M. Liu, G. Odyniec, H. G. Pugh, R. E. Renfordt, A. Sandoval, D. Schall, L. S. Schroeder, R. Stock, H. Ströbele, M. A. Vient, Phys. Rev. C **45**, 299 (1992).

[Bert88] G.F. Bertsch, and S. Das Gupta, Phys. Rep. **160**, 190 (1988)

[Bind84] K. Binder and D. Stauffer, in Application of Monte-Carlo Methods in Statistical Physics, ed. K. Binder (Springer, Heidelberg, 1984), p. 241.

[Biro86] T. S. Biro, J. Knoll, and J. Richert, Nucl. Phys. **A 459**, 692 (1986).

[Biza93] G. Bizard, R. Bougault, R. Brou, J. Colin, D. Durand, A. Genoux-Lubain, J. L. Laville, C. LeBrun, J. F. Lecolley, M. Louvel, J. Péter, J. C. Steckmeyer, B. Tamain, A. Badala, T. Motobayashi, G. Rudolf, and L. Stuttgé, Phys. Lett. **B302**, 162 (1993).

[Blai80] J. P. Balizot, Phys. Rep. **64**, 171 (1980).

[Blum91] Y. Blumenfeld, N. Colonna, P. Roussel-Chomaz, D. N. Delis, K. Hanold, J. C. Meng, G. F. Peaslee, Q. C. Sui, G. J. Wozniak, L. G. Moretto, B. Libby, A. C. Mignerey, G. Guarino, N. Santoruvo and I. Iori, Phys. Rev. Lett. **66**, 576 (1991).

[Boal86] David H. Boal, Alan L. Goodman, Phys. Rev. C **33**, 1690 (1986).

[Bond85] J. P. Bondorf, R. Donangelo, I. N. Mishustin, C. J. Pethick, H. Schulz, and K. Sneppen, Nucl. Phys. **A443**, 321 (1985).

[Boug88] R. Bougault, F. Delaunay, A. Genoux-Lubain, C. Lebrun, J. F. Lecolley, R. Lefebvres, M. Louvel, J. C. Steckmeyer, J. C. Adloff, B. Bilwes, R. Bilwes, M. Glaser, G. Rudolf, F. Scheibling, L. Stuttge, and J. L. Ferrero, Nucl. Phys. **A488**, 255c (1988).

[Bowm91] D. R. Bowman, G. F. Peaslee, R. T. de Souza, N. Carlin, C. K. Gelke, W. G. Gong, Y. D. Kim, M. A. Lisa, W. G. Lynch, L. Phair, M. B. Tsang, C. Williams, N. Colonna, K. Hanold, M. A. McMahan, G. J. Wozniak, L. G. Moretto, and W. A. Friedman, Phys. Rev. Lett. **67**, 1527 (1991).

[Bowm92] D. R. Bowman, C. M. Mader, G. F. Peaslee, W. Bauer, N. Carlin, R. T. de Souza, C. K. Gelbke, W. G. Gong, Y. D. Kim, M. A. Lisa, W. G. Lynch, L. Phair, M. B. Tsang, C. Willams, N. B. Colonna, K. Hanold, M. A. McMahan, G. J. Wozniak, and L. G. Moretto, and W. A. Friedman, Phys. Rev. C **46**, 1834 (1992).

[Bran79] S. Brandt and H. D. Dahmen, Z. Phys. C1, 61 (1979).

[Brow85] G. E. Brown and E. Osnes, Phys. Rev. Lett. **159B**, 223 (1985).

[Camp86] X. Campi, J. Phys. A **19**, L917 (1986).

[Camp88] X. Campi, Phys. Lett. **B208**, 351 (1988).

[Camp92] X. Campi, and H. Krivine, Nucl. Phys. **A545**, 161c (1992).

[Cava90] C. Cavata, M. Demoulins, J. Gosset, M.-C. Lemaire, D. L'Hôte, J. Poitou, and O. Valette, Phys. Rev. C **42**, 1760 (1990).

[Cebr90a] D. Cebra, PhD. Thesis, Michigan State University, 1990.

[Cebr90b] D. A. Cebra, S. Howden, J. Karn, A. Nadasen, C. A. Ogilvie, A. Vander Molen, G. D. Westfall, W. K. Wilson, and J. S. Winfield, Phys. Rev. Lett. **64**, 2246 (1990).

[Cebr91] D. A. Cebra, S. Howden, J. Karn, D. Kataria, M. Maier, A. Nadasen, C. A. Ogilvie, N. Stone, D. Swan, A. Vander Molen, W. K. Wilson, J. S. Winfield, J. Yurkon, G. D. Westfall, and E. Norbeck, Nucl. Instr. Meth. **A300**, 518 (1991).

[Chit83] C. B. Chitwood, D. J. Fields, C. K. Gelbke, W. G. Lynch, A. D. Panagiotou, M. B. Tsang, H. Utsunomiya, and W. A. Friedman, Phys. Lett. **131B**, 289 (1983).

[Colo92] M. Colonna, P. Roussel-Chomaz, N. Colonna, M. Di Toro, L. G. Moretto, and G. J. Wozniak, Phys. Lett. **B 283**, 180 (1992).

[Coni79] A. Coniglio, H. E. Stanley, and W. Klein, Phys. Rev. Lett. **42** 518 (1979).

[Cser86] L. P. Csernai and J. I. Kapusta, Phys. Rep. **131**, 223 (1986).

[Cugn82] J. Cugnon, J. Knoll, C. Riedel, and Y. Yariv, Phys. Lett. **109B**, 167 (1982).

[Cugn85] J. Cugnon, and Denis L'Hôte, Nucl. Phys. **A447**, 27c (1985).

[Curt83] W. Curtin, H. Toki and D. K. Scott, Phys. Lett. **123B**, 289 (1983).

[Dani85] P. Danielewicz, and G. Odyniec, Phys. Lett. **157B**, 146 (1985).

[Dani88] P. Danielewicz, H. Ströbele, G. Odyniec, D. Bangert, R. Bock, R. Brockmann, J. W. Harris, H. G. Pugh, W. Rauch, R. E. Renfordt, A. Sandoval, D. Schall, L. S. Schroeder, and R. Stock, Phys. Rev. C **38**, 120 (1988).

[Desb87] J. Desbois, Nucl. Phys. **A466**, 724 (1987).

[Doss86] K. G. R. Doss, H. Å. Gustafsson, H. H. Gutbrod, K. H. Kampert, B. Kolb, H. Löhner, B. Ludewigt, A. M. Poskanzer, H. G. Ritter, H. R. Schmidt, and H. Wieman, Phys. Rev. Lett. **57**, 302 (1987).

[Doss87] K. G. R. Doss, H. A. Gustafsson, H. Gutbrod, J. W. Harris, B. V. Jacak, K. H. Kampert, B. Kolb, A. M. Poskanzer, H. G. Ritter, H. R. Schmidt, L. Teitelbaum, M. Tincknell, S. Weiss, and H. Wieman, Phys. Rev. Lett. **59**, 2720 (1987).

[Fai83] G. Fái, and J. Randrup, Nucl. Phys. **A404**, 551 (1983).

[Fan92] Zhi-Guo Fan, private communication.

[Fish67] M. E. Fisher, Physics 3, 255 (1967).

[Finn82] J. E. Finn, S. Agarwal, A. Bujak, J. Chuang, L. J. Gutay, A. S. Hirsch, R. W. Minich, N. T. Porile, R. P. Scharenberg, and B. C. Stringfellow, Phys. Rev. Lett. **49**, 1321 (1982).

[Frie89] William A. Friedman, Phys. Rev. C **40**, 2055 (1989).

[Fish67] M. E. Fisher, Physics 3, 255 (1967)

[Gale90] C. Gale, G. M. Welke, M. Prakash, S. J. Lee, and S. Das Gupta, Phys. Rev. C **41**, 1545 (1990).

[Glen86] N. K. Glendenning, L. P. Csernai, and J. I. Kapusta, Phys. Rev. C **33**, 1299 (1986).

[Glen88] N.K. Glendenning, Phys. Rev. C **37**, 2733 (1988)

[Gong92] Wen Guang Gong, PhD. Thesis, Michigan State University, 1992.

[Gong90] W. G. Gong, W. Bauer, C. K. Gelbke, Phys. Rev. Lett. C **65**, 2114 (1990).

[Gong91] W. G. Gong, C. K. Gelbke, W. Bauer, N. Carlin, R. T. de Souza, Y. D. Kim, W. G. Lynch, T. Murakami, G. Poggi, D. P. Sanderson. M. B. Tsang, H. M. Xu, D. E. Fields, K. Kwiatkowski, R. Planeta, V. E. Viola, Jr. S. J. Yennello, and S. Pratt, Phys. Rev. C **43**, 1804 (1991).

[Good84] Alan L. Goodman, Joseph I. Kapusta, Aram Z. Mekjian, Phys. Rev. C **30**, 851 (1984).

[Goss77] J. Gosset, H. H. Gutbrod, W. G. Meyer, A. M. Poskanzer, A. Sandoval, R. Stock, and G. D. Westfall, Phys. Rev. C **16**, 629 (1977).

[Goss78] J. Gosset, J. I. Kapusta, and G. D. Westfall, Phys. Rev. C **18**, 844 (1978).

[Grab92] B. Grabež, Phys. Rev. C **45**, R5 (1992).

[Gruh82] C. R. Gruhnm, M. Binimi, R. Loveman, W. Pang, M. Roach, D. K. Scott, A. Shotter, T. J. Symons, J. Wouters, M. Zisman, R. Devries, Y. C. Peng, and W. Sondheim, Nucl. Instr. Meth. **196**, 33 (1982).

[Gupt93] Subal Das Gupta and Gary D. Westfall, Physics Today, p.34, May 1993.

[Gust84] H. A. Gustafsson, H. H. Gutbrod, B. Kolb, H. Lohner, B. Ludewigt, A. M. Poskanzer, T. Renner, H. Riedesel, H. G. Ritter, A Warwick, F. Werk, and H. Wieman, Phys. Rev, Lett.**52**, 1590 (1984)

[Gutb89a] H. H. Gutbrod, A. M. Poskanzer, and H. G. Ritter, Rep. Prog. Phys. **52**, 1267 (1989).

[Gutb89b] H. H. Gutbrod, K. H. Kampert, B. W. Kolb, A. M. Poskanzer, H. G. Ritter, and H. R. Schmidt, Phys. Lett. **216B**, 267 (1989).

[Hage92] K. Hagel, M. Gonin, R. Wada, J. B. Natowitz, B. H. Sa, Y. Lou, M. Gui, D. Utley, G. Nebbia, D. Fabris, G. Prete, J. Ruiz, D. Drain, B. Chambon, B. Cheynis, D. Guinet, X. C. Hu, A. Demeyer, C. Pastor, A. Giorni, A. Lleres, P. Stassi, J. B. Viano, and P. Gonthier, Phys. Rev. Lett. **68**, 2141 (1992).

[Herr81] D. W. Herrmann and D. Stauffer, Z. Phys. **B44**, 339 (1981).

[Herr93] N. Herrmann, Nucl. Phys. **A553**, 739c (1993).

[Hirs84] A. S. Hirsch, A. Bujak, J. E. Finn, L. J. Gutay, R. W. Minich, N. T. Porile, R. P. Scharenberg, and B. C. Stringfellow, Phys. Rev. C **29**, 508 (1984).

[Hube91] J. Hubele, P. Kreutz, J. C. Adloff, M. Begemann-Blaich, P. Bouissou, G. Imme, I. Iori, G. J. Kunde, S. Leray, V. Lindenstruth, Z. Liu, U. Lynen, R. J. Meijer, U. Milkau, A. Moroni, W. F. J. Müller, C. Ngô, C. A. Ogilvie, J. Pochodzalla, G. Raciti, G. Rudolf, H. Sann, A. Schüttauf, W. Seidel, L. Stuttge, W. Trautmann, and A. Tucholski, Z. Phys. A. **340**, 263 (1991).

[Hüfn85] J. Hüfner, Phys. Rep. **125**, 129 (1985).

[Jaca87] B. V. Jacak, G. D. Westfall, G. M. Crawley, D. Fox, C. K. Gelbke, L. H. Harwood, B. E. Hasselquist, W. G. Lynch, D. K. Scott, H. Stöcker, M B. Tsang, G. Buchwald, and T. J. M. Symons, Phys. Rev. C **35**, 1751 (1987).

[Jaca84] B. V. Jacak, PhD. dissertation, Michigan State University, 1984.

[Jako82] B. Jakobsson, G. Jönsson, B. Lindkvist and A. Oskarsson, Z. Phys. **A307**, 293 (1982).

[Jaqa84] H. R. Jaqaman, A. Z. Mekjian, and L. Zamick, Phys. Rev. C **29**, 2067 (1984).

[Kim89] Y. D. Kim, M. B. Tsang, C. K. Gelbke, W. G. Lynch, N. Carlin, Z. Chen, R. Fox, W. G. Gong, T. Murakami, T. K. Nayak, R. M. Ronnigen, H. M. Xu, F. Zhu, W. Bauer, L. G. Sobotka, D. Stracener, D. G. Sarantites, Z. Majka, V. Abenante, and H. Griffin, Phys. Rev. Lett. **63**, 494 (1989).

[Küpp74] W. A. Küpper, G. Wegmann, and E. R. Hilf, Ann. Phys. **88**, 454 (1974).

[Kapu84] Joseph Kapusta, Phys. Rev. C **29**, 1735 (1984).

[Kim92] Y. D. Kim, R. T. deSouza, D. R. Bowman, N. Carlin, C. K. Gelbke, W. G. Gong, W. G. Lynch, L. Phair, M. B. Tsang, and F. Zhu, Phys. Rev. C **45**, 338 (1992).

[Kott87] R. Kotte, H.-J. Keller, H.-G. Ortlepp and F. Stary, Nucl. Instr. Meth. **A257**, 244 (1987).

[Krof89] D. Krofcheck, W. Bauer, G. M. Crawley, C. Djalali, S. Howden, C. A. Ogilvie, A. Vander Molen, G. D. Westfall, and W. K. Wilson, Phys. Rev. Lett. **63**, 2028 (1989).

[Krof91] D. Krofcheck, D. A. Cebra, M. Cronqvist, R. Lacey, T. Li, C. A. Ogilvie, A. Vander Molen, K. Tyson, G. D. Westfall, W. K. Wilson, J. S. Winfield, A. Nadasen, and E. Norbeck, Phys. Rev. C **43**, 350 (1991).

[Krof92] D. Krofcheck, W. Bauer, G. M. Crawley, S. Howden, C. A. Ogilvie, A. Vander Molen, G. D. Westfall, and W. K. Wilson, Phys. Rev. C **46** 1416 (1992).

[Krus85] H. Kruse, B. V. Jacak, H. Stöcker, Phys. Rev. Lett. **54**, 289 (1985).

[Lace93] Roy Lacey, A. Elmaani, J. Lauret, T. Li, W. Bauer, D. Craig, M. Cronqvist, E. Gualtieri, S. Hannuschke, T. Reposeur, A. Vander Molen, G. D. Westfall, W. K. Wilson, J. S. Winfield, J. Yee, S. Yennello, A. Nadasen, R. S. Tickle, and E. Norbeck, Phys. Rev. Lett. **70**, 1224 (1993).

[Lamb78] D. Q. Lamb, J. M, Lattimer, C. J. Pethick, and D. G. Ravenhall, Phys. Rev. Lett. **41**, 1623 (1978).

[Phai92] L. Phair, W. Bauer, D. R. Bowman, N. Carlin, R. T. de Souza, C. K. Gelbke, W. G. Gong, Y. D. Kim, M. A. Lisa, W. G. Lynch, G. F. Peaslee, M. B. Tsang, C. Williams, F. Zhu, N. Colonna, K. Hanold, M. A. McMahan, G. J. Wozniak, and L. G. Moretto, Phys. Lett. **B285**, 10 (1992).

[Li93] T. Li, W. Bauer, D. Craig, M. Cronqvist, E. Gualtieri, S. Hannuschke, R. Lacey, W. J. Llope, T. Reposeur, A. M. Vander Molen, G. D. Westfall, W. K. Wilson, J. S. Winfield, J. Yee, S. J. Yennello, A. Nadasen, R. S. Tickle, and E. Norbeck, Phys. Rev. Lett. **70** 1924 (1993).

[Llop93] W. Llope, private communication.

[Lópe89] J. A. López, and J. Randrup, Nucl. Phys. **A491**, 477 (1989).

[Ma93] Ma Yugang, Shen Wenqing, Feng Jun, Ma Yuqiang, Z. Phys. **A344**, 469 (1993).

[Mcdo84] R. J. McDonald, L. G. Sobotka, Z. Q. Yao, G. J. Wozniak and G. Guarino, Nucl. Instr. Meth. **219**, 508 (1984).

[Meye81] W. G. Meyer, N. Matsushita, private communication.

[Mini82] R. W. Minich, S. Agarwal, A. Bujak, J. Chuang, J. E. Finn, L. J. Gutay, A. S. Hirsch, N. T. Porile, R. P. Scharenberg, and B. C. Stringfellow, Phys. Lett. **118B**, 458 (1982).

[Mahi88] M. Mahi, A. T. Bujak, D. D. Carmony, Y. H. Chung, L. J. Gutay, A. S. Hirsch, G. L. Paderewski, N. T. Porile, T. C. Sangster, R. P. Scharenberg, and B. C. Stringfellow, Phys. Rev. Lett. **60**, 1936 (1988).

[Moli85] J. J. Molitoris, D. Hahn, and H. Stöcker, Nucl. Phys.**A447**, 13c (9185).

[Moro84] A. Moroni, I. Iori, and L. Z. Yu, Nucl. Instr. Meth. **225**, 57 (1984).

[Oed83a] A. Oed, P. Geltenbort and F. Gönnenwein, Nucl. Instr. Meth. **205**, 451 (1983).

[Oed83b] A. Oed, P. Geltenbort, F. Gönnenwein, T. Manning and D. Souque, Nucl. Instr. Meth. **205**, 455 (1983).

[Ogil89a] C. A. Ogilvie, D. A. Cebra, J. Clayton, P, Danielewicz, S. Howden, J. Karn, A. Nadasen, A. Vander Molen, G. D. Westfall, W. K. Wilson, and J. S. Winfield Phys. Rev. C **40**, 2592 (1989).

[Ogil89b] C. A. Ogilvie, D. A. Cebra, J. Clayton, S. Howden, J. Karn, A. Vander Molen, G. D. Westfall, W. K. Wilson, and J. S. Winfield Phys. Rev. C **40**, 654 (1989).

[Ogil89c] C. A. Ogilvie, D. A. Cebra, J. Clayton, S. Howden, J. Karn, A. Vander Molen, G. D. Westfall, W. K. Wilson, and J. S. Winfield, Phys. Lett. **B231**, 35 (1989).

[Ogil90] C. A. Ogilvie, W. Bauer, D. A. Cebra, J. Clayton, S. Howden, J. Karn, A. Nadasen, A. Vander Molen, G. D. Westfall, W. K. Wilson, and J. S. Winfield, Phys. Rev. C **42**, R10 (1990)

[Ogil91] C. A. Ogilvie, J. C. Adloff, M. Begemann-Blaich, P. Bouissou, J. Hubele, G. Imme, I. Iori, P. Kreutz, G. J. Kunde, S. Leray, V. Lindenstruth, Z. Liu, U. Lynen, R. J. Meijer, U. Milkau, W. F. J. Müller, C. Ngô, J. Pochodzalla, G. Raciti, G. Rudolf, H. Sann, A. Schüttauf, W. Seidel, L. Stuttge, W. Trautmann, and A. Tucholski, Phys. Rev. Lett. **67**, 1214 (1991).

[Ogil93] C. A. Ogilvie, J. C. Adloff, M. Begemann-Blaich, P. Bouissou, J. Hubele, G. Imme, I. Iori, P. Kreutz, G. J. Kunde, S. Leray, V. Lindenstruth, Z. Liu, U. Lynen, R. J. Meijer, U. Milkau, W. F. J. Müller, C. Ngô, J. Pochodzalla, G. Raciti, G. Rudolf, H. Sann, A. Schüttauf, W. Seidel, L. Stuttge, W. Trautmann, and A. Tucholski, Nucl. Phys. **A553**, 271c (1993).

[Pan93] Qiubao Pan, and Pawel Danielewicz, Phys. Rev. Lett. **70**, 2062 (1993)

[Pana84] A. D. Panagiotou, M. W. Curtin, H. Toki, D. K. Scott, and P. J. Siemens, Phys. Rev. Lett. **52**, 496 (1984).

[Peas92] G. F. Peaslee, Proceedings of the 8th Winter Workshop on Nuclear Dynamics, p.75 (1992).

[Péte90a] J. Péter, J. P. Sullivan, D. Cussol, G. Bizard, R. Brou, M. Louvel, J. P. Patry, R. Regimbart, J. C. Stechmeyer, B. Tamin, E. Crema, H. Doubre, K. Hagel, G. M. Jin, A. Peghaire, F. Saint-Laurent, Y. Cassagnou, R. Legrain, C. Lebrun, E. Rosato, R. MacGrath, S. C. Jeong, S. M. Lee, Y. Nagashima, T. Nakagawa, M. Ogihara, J. Kasagi, T. Motobayashi, Phys. Lett. **237B**, 187 (1990).

[Péte90b] J. Péter, J. P. Sullivan, D. Cussol, G. Bizard, R. Brou, M. Louvel, J. P. Patry, R. Regimbart, J. C. Stechmeyer, B. Tamin, E. Crema, H. Doubre, K. Hagel, G. M. Jin, A. Peghaire, F. Saint-Laurent, Y. Cassagnou, R. Legrain, C. Lebrun, E. Rosato, R. MacGrath, S.C. Jeong, S. M. Lee, Y. Nagashima, T. Nakagawa, M. Ogihara, J. Kasagi, T. Motobayashi, Nucl. Phys. **A519**, 127c (1990).

[Peth87] C. J. Pethick and D. G. Ravenhall, Nucl. Phys. **A471**, 19c (1987).

[Pori89] N. T. Porile, A. J. Bujak, D. D. Carmony, Y. H. Chung, L. J. Gutay, A. S. Hirsch, M. Mahi, G. L. Paderewski, T. C. Sangster, R. P. Scharenberg, and B. C. Stringfellow, Phys. Rev. C **39**, 1914 (1989).

[Rich90] J. Richert and P. Wagner, Nucl. Phys. **A517**, 399 (1990).

[Ritt85] H. G. Ritter, K. G. R. Doss, H. A. Gustafsson, H. H. Gutbrod, K. H. Kampert, B. Kolb. H. Lohner, B. Ludewigt, A. M. Poskanzer, A. Warwick, and H. Wieman, Nucl. Phys. **A447**, 3c (1985).

[Sang92] T. C. Sangster, H. C. Britt, D. J. Fields, L. F. Hansen, R. G. Lanier, M. N. Namboodiri, B. A. Remington, M. L. Webb, M. Begemann-Blaich, T. Blaich, M. M. Fowler, J. B. Wilhelmy, Y. D. Chan, A. Dacal, A. Harmon, J. Pouliot, R. G. Stokstad, S. Kaufman, F. Videbaek, Z. Fraenkel, G. Peilert, H. Stöcker, W. Greiner, A. Botvina, and I. N. Mishustin, Phys. Rev. C **46**, 1404 (1992).

[Saue76] G. Sauer, H. Chandra, and U. Mosel, Nucl. Phys. **A264**, 221 (1976).

[Schi82] Ch. Schiessl, W. Wagner, K. Hartel, P. Kienle, H. J. Körner, W. Mayer, and K. E. Rehm, Nucl. Instr. Meth. **192**, 291 (1982).

[Schu82] H. Schulz, L. Münchow, G. Röpke and M. Schmidt, Phys. Lett. **119B**, 12 (1982).

[Shen85] N. J. Shenav, and H. Stelzer, Nucl. Instr. Meth. **228** (1985).

[Stau79] D. Stauffer, Phys. Rep. 54, 1 (1979).

[Strö83] H. Ströbele, R. Brockmann, J. W. Harris, F. Riess, A. Sandoval, R. Stock, K. L. Wolf, H. G. Pugh, L. S. Schroeder, R. E. Renfordt, K. Tittel, and M. Maier, Phys. Rev. C **27**, 1349 (1983).

[Sull90] J. P. Sullivan, J. Péter, D. Cussol, G. Bizard, R. Brou, M. Louvel, J. P. Patry, R. Regimbart, J. C. Steckmeyer, B. Tamain, E. Crema, H. Doubre, K. Hagel, G. M. Jin, A. Péhaire, F. Saint-Laurent, Y. Cassagnou, R. Legrain, C, Lebrun, E. Rosato, R. MacGrath, S. C. Jeong, S. M. Lee, Y. Nagashima, T. Nakagawa, M. Ogihara, J. Kasagi, and T. Motobayashi, Phys. Lett. **B249**, 8 (1990).

[Sull92] J. P. Sullivan, J. Péter, Nucl. Phys. **A540**, 275 (1992).

[Sumi92] K. Sumiyoshi, H. Toki, and R. Brockmann, Phys. Lett. **B276**, 393 (1992).

[Tsan89] M. B. Tsang, G. F. Bertsch, W. G. Lynch, M. Tohyama, Phys. Rev. C **40**, 1685 (1989).

[Wada89] R. Wada, D. Fabris, K. Hagel, G. Nebbia, Y. Lou, M. Gonin, J. B. Natowitz, R. Billerey, B. Cheynis, A. Demeyer, D. Drain, D. Guinet, C. Pastor, J. A. Arja, A. Giorni, D. Heuer, C. Morand, B. Viano, C. Mazur, C. Ngô, S. Leray, R. Lucas, M. Ribrag, and E. Tomasi, Phys. Rev. C **39**, 397 (1989).

[West76] G. D. Westfall, J. Gosset, P. J. Johansen, A. M. Poskanzer, W. G. Meyer, H. H. Gutbrod, A. Sandoval, and R. Stock, Phys. Rev. Lett. **37**, 1202 (1976).

[West82] G. D. Westfall, B. V. Jacak, N. Anataraman, M. W. Curtin, G. M. Crawley, C. K. Gelbke, B. Hasselquist, W. G. Lynch, D. K. Scott, B. M. Tsang, M. J. Murphy, T. J. M. Symons, R. Legrain, T.J. Majors, Phys. Lett. **116B**, 118 (1982)